EXPERIMENTAL MODELING OF SALT FLOW SUBPARALLEL TO BASEMENT-INVOLVED FAULTS: INFLUENCE OF SALT DISTRIBUTION AND FAULT GEOMETRIES IN RIFT BASINS

By

MATTATHIAS DAVID NEEDLE

A thesis submitted to the

Graduate School-New Brunswick

Rutgers, The State University of New Jersey

In partial fulfillment of the requirements

For the degree of

Masters of Science

Graduate Program in Geological Sciences

Written under the direction of

Roy W. Schlische

Martha O. Withjack

And approved by

_____

_____

_____

New Brunswick, New Jersey

October 2016

ABSTRACT OF THE THESIS

Experimental Modeling of Salt Flow Subparallel to Basement-Involved Faults: Influence of Salt Distribution and Fault Geometries

By MATTATHIAS DAVID NEEDLE

Thesis Directors:

Dr. Roy W. Schlische and Dr. Martha O. Withjack

Rock salt exhibits highly ductile behavior at shallow crustal levels, and its presence profoundly affects the structural development of rift basins. Basement-involved normal faults strongly influence the initial thickness and distribution of the synrift salt. Subsequent deformation and deposition during and after rifting cause the salt to flow. This work uses experimental (analog) modeling to examine the secondary structures that develop in the sedimentary cover above synrift salt that flows subparallel to the strike of basement-involved faults. In the models, silicone polymer simulates salt, wet clay simulates the sedimentary cover, and rigid blocks represents basement-involved faults. Extension imposed at the base of the models causes the silicone polymer to flow subparallel to the rigid blocks.

The models indicate that two zones of deformation form within the sedimentary cover: 1) a shear zone with oblique-slip faults that trends (sub)parallel to the strike of the underlying faults; and 2) an extensional domain with predominantly normal faults that strike (sub)perpendicular to the flow direction of

the ductile unit. At the clay surface, some faults in the shear zone and extensional domain link, forming curved fault surfaces.

The initial thickness and distribution of the highly ductile unit affect the development of secondary structures in the overlying cover. The thickness of the ductile unit controls the degree of decoupling between shallow and deep structures. Where the ductile unit is thick, the extensional domain and shear zone in the cover are broad, whereas where the ductile unit is thin, the extensional domain and shear zone in the cover are narrow and form directly above the deep structures. Varying the initial distribution of the ductile unit produces subsequent asymmetrical deformation in the overlying cover.

The orientation of pre-existing faults, relative to the flow direction of the highly ductile unit, also has an influence on the development of secondary structures. When the flow of the ductile unit (relative to a pre-existing fault) produces highly oblique extension at depth, deformation is distributed broadly in the extensional domain, and the shear zone forms above and trends parallel to the pre-existing fault. However, when the flow of the ductile unit (relative to the pre-existing fault) produces highly oblique shortening at depth, 1) the trend of the shear zone in the cover is not parallel to the strike of the underlying pre-existing fault, and 2) secondary features in the extensional domain are muted in the cover. The latter suggests that the ductile unit distributes the deformation and, thus, subdues the expression of both shortening and extensional features at the surface.

Comparisons of the modeling results in this thesis to the deformation in the Jeanne d'Arc basin of offshore Newfoundland, Canada, suggest that the synrift Argo

Salt flowed parallel to the basin's long-axis. The salt flow produced secondary structures in the sedimentary cover above the salt including trans-basin normal faults and shear zones above basement-involved faults.

ACKNOWLEDGMENTS

It has been an honor to work with Martha Withjack and Roy Schlische for my Masters degree. They have shared with me their expertise of analog modeling, scientific writing and communication, and extensional tectonics. This thesis is a culmination of many of the skills they have bestowed upon me, but not a representation of *all* they have given me. Thank you to Don Monteverde and Chris Potter for their guidance and support of me as a geologist. Their love and curiosity for geology is infectious. Thank you to Iain Sinclair and Husky Energy for inspiration, direction, and funding for the experimental models of this thesis.

Thank you to Sean Kinney, Cesar Sequeira, Kathleen Warrell, and Natalie Stier for reviewing and discussing my research, and embarking on adventures to fuel the spirit. The following individuals assisted me with constructing and collecting data from the models in this study: Mike Flite, Michael Klaser, Michelle Kuhn, Michelle Miller, Christina Sheng, Ben Dunham, Bill Reilly, Phil Darias, and J.N. Stanley. Thank you to the maintenance staff of Riemann-Wright Labs for tolerating and taking care of the mess (dry-clay tracks) that I made outside of the lab. Thank you to Jason Pappas for tech support and encouragement regarding graphic design.

Lauren Adamo and Patricia Irizarry fostered my abilities as an outreach scientist and artist. They gave me free-reign to be creative while communicating with the public. Thank you to Jim Wright for often providing the intellectual discourse I desired as I matured as a 21st century scientist. Thank you to my comrades in the Rutgers Geology Swim Team: Juliane Gross, Brent Turrin, and Xiaoran Chen. You enabled me to have a sound mind in a sound body.

Table of Contents

List of Figures and Tables

1. INTRODUCTION

Rift basins, which are wide crustal depressions bounded by one or more basement-involved normal faults (commonly referred to as "border faults"), result from crustal extension (e.g., Withjack et al., 2002). According to Withjack et al. (2002), the presence of a highly ductile unit (salt or overpressured shale) in the pre-rift or synrift section of a basin is an important factor in controlling the style of subsequent deformation. Examples of rift basin containing a highly ductile unit in the synrift section include the Jeanne d'Arc and Suez basins (Fig. 1.1). In these basins, the initial thickness of the salt is fault-controlled, and can vary across the basin and from fault block to fault block. Secondary normal faults may detach within these highly ductile units, and forced folds above deep-seated normal faults are common (e.g., Withjack & Callaway, 2000; Withjack et al., 2002). These secondary structures may trap hydrocarbons; thus, understanding their development is important. The presence of salt complicates the interpretation of seismic-reflection profiles because salt, with its relatively low density and high velocity compared to other sedimentary rocks, commonly obscures subsalt structural geometries.

Scaled experimental (analog) modeling is a tool for enhancing our understanding of the spatial and temporal development of structures. Numerous studies have involved experimental modeling of salt structures (e.g., Hudec and Jackson, 2011, and references therein), but relatively few studies (e.g., Withjack and Callaway, 2000; Gartrell et al., 2005; Del Ventisette et al., 2006; Durcanin, 2009) have examined the effects of a synrift ductile unit on subsequent deformation within a rift basin. This thesis examines the structures that develop in the sedimentary

cover above a synrift ductile unit that flows parallel or subparallel to the border faults and/or other basement-involved faults (Fig. 1.2). Specifically, the following questions serve as the primary motivation for this study:

1. What secondary structures develop in the overlying sedimentary cover?
2. How does the initial thickness and distribution of the highly ductile unit affect the development of secondary structures in the overlying sedimentary cover?
3. How does the orientation of a pre-existing basement-involved fault, relative to the flow direction of the highly ductile unit, influence the development of secondary structures?
4. How do the structures formed in these experimental models compare to those in similar experimental models and to natural structures in the Jeanne d'Arc rift basin of offshore Newfoundland, Canada (Fig. 1.1a)?

2. METHODS

2.1. Modeling materials

Scaled experimental models permit direct observation of deformation at spatial and temporal scales that would not otherwise be possible. In modeling, the initial boundary conditions are known, whereas in the natural world, one can only observe complex structures that have developed over geologic time. By varying certain boundary conditions within a model (e.g., presence/orientation of pre-existing structures, thickness/distribution of ductile units, displacement distances/rates), it is possible to decipher the variables that influence the style of deformation and better describe the structural evolution of an analogous natural prototype.

Geometric, kinematic, and dynamic scaling are necessary to relate the model to a natural prototype (Hubbert, 1937). In the models in this thesis, wet clay simulates the sedimentary overburden. The clay, a mixture of mostly kaolinite and 40% water by weight, had a density of ~1600 kg/m^3 and cohesion of ~50 Pa (Eisenstadt and Sims, 2005; Withjack et al., 2007). Wet clay is an effective modeling material because the scaling of its cohesive strength relative to that of natural rocks is comparable to the desired scaling of its length; specifically, cm-scale structures in the model are comparable to km-scale structures in nature (e.g., Withjack and Callaway, 2000). Silicone putty simulates a ductile unit (e.g., salt), deforming plastically and with a Newtonian viscosity of ~10^4 Pa s (Withjack and Callaway, 2000, and references therein). See **7.1. Appendix** for details about scaling.

2.2. Model setup

The experimental apparatus (Fig. 2.1) has a southern fixed wall and a northern mobile wall with an attached rectangular basal mylar sheet. A rigid metal block on the eastern side of the apparatus simulates a basement-involved fault block (Figs. 2.2a and 2.2b). The edge of the rigid block dips 90°, simulating a steeply dipping fault surface. A layer of silicone putty overlies the mylar sheet to the west of the rigid block and south of a wet-clay dam (Fig. 2.2b). The clay dam prevents the putty from flowing out of the model during the experiment. This dam has no analog in the natural system, and, thus, deformation in its vicinity is an edge effect. A 3-cm-thick wet-clay layer, simulating sedimentary cover above the salt, overlies the rigid block, putty, and clay dam (Fig. 2.2c).

During the experiments, an electric motor displaces the mobile wall and the attached basal mylar sheet northward at a constant rate of 9 cm/h. The E-striking southern edge of the mylar sheet is a discontinuity (subsequently referred to as the "edge of the mylar sheet") that imposes a basal N-S extension. The northward movement of the mylar sheet also produces right-lateral shear at the base of the western edge of the rigid block. In response to the imposed basal extension and shear, the putty layer flows and the overlying layer of wet clay deforms. This thesis focuses on how the thickness of the putty layer and the orientation of the rigid block influence the deformation in the wet-clay layer.

2.2.1. Standard Model

All experimental models in this thesis are variations on the Standard Model (Table 2.1; Figs. 2.1 and 2.2). In the Standard Model, a 1-cm-thick layer of putty overlies the mylar sheet (Fig. 2.2). The top of the putty is level with the top of the rigid block (1 cm in height). The discontinuity on the eastern edge of the rigid block is N-trending.

2.2.2. Models with variable thickness of putty layer

The Thin-Putty Model and No-Putty Model have the same setup as the Standard Model except for the initial thickness of the putty (Fig. 2.3). In the Thin-Putty Model, the putty layer is 0.5 cm thick, and the rigid block on the eastern side of the model is 0.5 cm high. The No-Putty Model has no putty or a rigid block on the eastern side of the model. Rather, the N-trending discontinuity is between the eastern edge of the mylar sheet and the immobile base of the apparatus.

Like the Standard Model, the Putty-on-Discontinuity Model has a 1-cm thick layer of putty overlying the mylar sheet. However, in the Putty-on-Discontinuity Model, the rigid block on the eastern side of the model is 0.5 cm high and the putty covers the block. This simulates a ductile unit overlying a N-striking basement-involved fault (Fig. 2.4).

The Variable-Putty Model has a N-trending discontinuity on the eastern side of the model like the Standard Model. It also has a N-trending discontinuity on the western side of the model (Fig. 2.5). The putty thickness is 1 cm in the west and

about zero cm in the east. This model simulates a ductile unit with a thickness that varies perpendicular to the basin axis.

The Layered Model has a similar setup to the Variable-Putty Model except that its thick wet-clay cover has multiple layers with different colors (Fig. 2.6) but otherwise very similar mechanical properties. After the wet clay dried, vertical sections (oriented both perpendicular and parallel to the edge of the mylar sheet) permitted detailed cross-sectional analysis of the model. Additionally, high-resolution, plan-view photographs allowed comparisons of the deformation at the base and top of the clay layer. Post-desiccation photographs of the Layered Model were restored to their original thickness after accounting for vertical shrinkage (~40%) during desiccation. Fig. 2.6 shows cross-sectional evidence that putty flowed during the model setup: thus, the exact initial thickness and distribution of putty are unknown. Subsequent sections regarding the Layered Model focus on deformation features that are independent of knowing the precise initial thickness and distribution of the putty. See **Appendix 7.2** for photos of pre-restoration cross sections.

2.2.3. Models with variations in pre-existing fault geometry

In this suite of models, the edges of the rigid block (i.e., the shear-dominated discontinuity) have variable orientations relative to the northerly displacement direction of the mylar sheet (Fig. 2.7). The N5°E and N10°E models produce highly oblique extension along the discontinuity at the edge of the rigid block, whereas the

N5°W and N10°W models produce highly oblique shortening. The strike-slip component of deformation is right lateral in all models.

2.3. Data collection and presentation

Displacement of the mobile wall (and mylar sheet) (i.e., the boundary displacement) was at least 10.0 cm to the north for all models except for the No-Putty Model in which extreme thinning of the clay exposed the mylar sheet at ~ 5 cm of boundary displacement, forcing an end to the model run. Photographs of the surface of the models, taken every 0.1 cm of displacement, had three lighting configurations: light from the north, light from the south, and light from both north and south. Multiple lighting directions permit more accurate tracing of fault surfaces (Fig. 2.8). Oblique-view photos captured linear grooves on fault surfaces, which indicate slip directions (Fig. 2.9). Normal faults have grooves parallel to the dip direction of the fault and offset the top of the clay. Oblique-slip faults have grooves that are oblique to both the strike and dip direction of the fault; they also offset the top of the clay. Strike-slip faults, which do not offset the top of the clay, lack exposed grooves. Animations (developed in Adobe Premiere Pro CC), in which each frame consisted of a photograph from a single 0.1-cm increment of displacement, provided information about the temporal development of the surface deformation.

Cropped photographs exclude deformation associated with undesirable edge effects near the southern fixed wall, the spacers used to build the layers of the model, and the clay dam (Fig. 2.10). The cropped photographs focus on the deformation above the intersection of the basal discontinuities: the E-striking edge

of mylar sheet and the ~N-trending edge of the rigid block. See **7.2. Appendix** for photos with the full horizontal extent of the models.

3. OBSERVATIONS

3.1. Models that investigate the influence of putty thickness and distribution

3.1.1. Standard Model (at 10 cm of displacement)

The Standard Model has two domains of deformation: (1) a broad extensional domain in the clay above the putty containing E-, ESE-, and ENE-striking normal faults; and (2) a broad right-lateral shear zone with NNE-striking faults in the clay above the N-trending discontinuity (Fig. 3.1). Many faults have the greatest displacement near the intersection of the shear zone and extensional domain where ENE-striking faults link with NNE-striking faults with oblique slip (Fig. 3.2). In the N-trending shear zone, faults at the top of the clay strike NNE compared to the underlying N-trending discontinuity (Fig. 3.3). Based on their strike, these faults likely originated as en-echelon R-type Riedel structures produced by shear at the N-trending discontinuity. The NNE-striking faults consistently drop the top of the clay surface down to the WNW, and, therefore, are oblique-slip faults.

3.1.2. Standard Model: Temporal Development (Fig. 3.4)

A N-trending shear zone develops in the region above the buried N-trending discontinuity on the eastern side of the model at the start of displacement of the apparatus's moving wall (and mylar sheet). Between 2.0 and 4.0 cm of displacement, NNE-striking faults develop within the shear zone. As displacement increases, new NNE-striking faults form in the shear zone further south. An extensional zone composed of small E- and ENE-striking normal faults forms in the clay above the E-trending edge of the mylar sheet.

Between 4.0 and 6.0 cm of displacement, ENE-striking normal faults nucleate at the NNE-striking faults in the shear zone and propagate westward. At this linkage site, displacement on the fault surfaces has oblique-slip. Faults in the extensional domain increase in length and number as their displacement increases. Between 6.0 and 10.0 cm of displacement, new E-striking normal faults develop in the southern part of the extensional domain. Based on the heave magnitude, linked faults connecting the ENE-striking faults in the extensional domain and NNE-striking faults in the shear zone appear to accommodate much of the deformation.

3.1.3. No-Putty Model

Like the Standard Model, the No-Putty Model has an extensional domain and right-lateral shear zone. However, in the No-Putty Model, the extensional domain and shear zone are narrower (Fig. 3.5). The extensional domain consists of a single large E-trending fault-bounded depression above the E-striking edge of the mylar sheet (Fig. 3.5b). On its northern side, a large S-dipping normal fault accommodates most of the extension, whereas on its southern side, numerous small N-dipping normal faults accommodate the extension. The N-trending shear zone, with a right-lateral sense of shear (Fig. 3.5c), contains a long strike-slip fault that is subparallel to the underlying N-trending discontinuity. Unlike the Standard Model, the deformation at the top of the wet-clay cover in the No-Putty Model directly overlies the underlying discontinuities in both the extensional domain (E-striking edge of mylar sheet) and shear zone (N-trending discontinuity).

Within the shear zone, small NE-striking faults, which splay from the dominant strike-slip fault, form the boundaries of structures associated with strike-slip deformation. Uplifted blocks of clay are likely pop-up structures that formed at restraining bends. Subsided blocks of clay and gaps are likely pull-apart basins that formed at releasing bends (Fig. 3.6).

3.1.4. Thin-Putty Model

The Thin-Putty Model, with an intermediate putty thickness between that of the Standard Model and the No-Putty Model, demonstrates the effect of putty thickness on the fault distribution (Fig. 3.7). As putty thickness decreases, the deformation in the shear zone and extensional domain in the cover becomes more coupled with the deep deformation (i.e., the orientation and location of the shallow deformation matches that of the edge of the mylar sheet and the N-trending discontinuity).

For the Thin-Putty Model, N- and E-striking faults form orthogonal fault sets that bound rectangular blocks near the intersection of the shear zone and extensional domain (Fig. 3.8).

3.1.5. Putty-on-Discontinuity Model

As in the Standard Model, a broad shear zone and broad extensional domain develop over the N-trending discontinuity and edge of the mylar sheet, respectively (Fig. 3.9). At the surface, however, the shear zone is more diffuse than in the Standard Model with fewer NNE-striking faults, and it does not extend as far to the

south (Fig. 3.9). Generally, the faults in the extensional domain of the Putty-on-Discontinuity Model are evenly distributed and have similar heaves, whereas a few faults in the extensional domain of the Standard Model have large heaves and accommodate much of the deformation (Fig. 3.9).

3.1.6. Variable-Putty Model

The deformation in the Variable-Putty Model resembles that of the Standard Model where putty is thickest (west) and that of the No-Putty Model where putty is thinnest (east) (Fig. 3.10). Where putty is thicker (i.e., the western side of the model), displacement on faults is greatest at the linkage between a long NNW-striking fault in the shear zone and W- to WNW-striking faults in the extensional domain. A few NNW-striking en-echelon faults formed above the underlying western N-trending discontinuity. Additionally, normal faults in the extensional domain have a greater N-S distribution, and the faults with the greatest heave are offset considerably (to the north) from the edge of the mylar sheet (Fig. 3.10).

Where putty is thinnest (i.e., the eastern side of the model), deformation is more focused in the shear zone with pull-apart basins and pop-up structures developing. The extensional domain is narrower where putty is thinnest, and deformation is more coupled with the edge of the mylar sheet and eastern N-trending discontinuity (Fig. 3.10).

From west to east, the distribution of extensional structures (measured in the direction of movement of the mylar sheet) gradually varies from broader to

narrower as the putty thickness decreases. This varied distribution produces an asymmetrical extensional domain (Fig. 3.10).

3.1.7. Layered Model

As discussed in the Methods section, the putty flowed during the model setup; thus, the exact initial distribution and thickness of the ductile unit is unknown. However, the Layered Model still has utility, and I will focus on observations that are independent of the approximate distribution and thickness of the ductile unit.

The top of the clay (Fig. 3.11) has fewer faults than the base of the clay (Fig. 3.12). At the top of clay, faults in the shear zone extend beyond the N-trending discontinuities; however, at the base of clay, no faults form above the top of the rigid blocks (Fig. 3.13). Thus, the deformation zone widens upward. At the base of clay, the strike of the faults in the shear zone becomes more northerly with increasing proximity to the N-trending discontinuity (Fig. 3.13b). In cross section, most faults in the shear zones dip steeply (Fig. 3.14). The extensional domain has a set of N-dipping domino-style faults with normal separation (Fig. 3.15).

3.2. Models that investigate the influence of the orientation of the shear-dominated discontinuity

3.2.1. N5°E Model and N10°E Model

As in the Standard Model, two domains of deformation develop in the N5°E Model and the N10°E Model: (1) a broad extensional domain containing, E-, ESE-,

and ENE- striking normal faults; and (2) a broad shear zone with NNE- and NE-striking oblique-slip faults (Fig. 3.16); this shear zone directly overlies the basal shear-dominated discontinuity. As in the Standard Model, many faults have the greatest displacement near the intersection of the shear zone and extensional domain where ENE-striking faults link with NNE-striking faults with oblique slip. Tips of ENE- and E-striking normal faults do not extend far beyond the buried shear-dominated (N5°E- and N10°E-trending) discontinuities (Figs. 3.16 and 3.17).

The orientation of the shear-dominated discontinuities influences the trend of the shear zone and the strike of the constituent faults. For example, the shear-zone faults in the N10°E Model have a more easterly strike than the faults in the shear zone of the N5°E Model. The shear-zone faults in the N5°E Model have a more easterly strike than the faults in the Standard Model (Fig. 3.18a). For the shear zones of the Standard, N5°E, and N10°E Models, faults in the north strike 10-20° clockwise of the shear-dominated discontinuity, and fault segments are long (Figs. 3.18b and 3.18c). In the south, faults strike 30-40° clockwise of the shear-dominated discontinuity, and fault segments are shorter (Figs. 3.18b and 3.18c).

3.2.2. N5°W Model and N10°W Model

As in the Standard Model, an extensional domain and a shear zone develop in the N5°W Model and the N10°W Model (Fig. 3.19). The extensional domains have normal faults that strike E, ESE, and ENE, as in the Standard Model (Fig. 3.19). However, compared to the Standard Model, the extensional domains of the N5°W and N10°W Models: 1) have fewer normal faults, and 2) these normal faults have

less displacement, characterized by smaller heaves (Fig. 3.19). The extensional domains of the N5°W and N10°W Models also have zones with limited normal faulting (Fig. 3.20).

At the surface, the trends of the shear zones of the N5°W Model and N10°W Model do not overlie their respective shear-dominated discontinuities at depth (Fig. 3.21). The shear zones at the surface trend N and are dominated by N-striking strike-slip faults, despite the N5°W and N10°W trends of the shear-dominated discontinuities at depth (Fig. 3.21). The shear zones of the N5°W Model and the N10°W Model also greatly differ from the shear zone of the Standard Model (Figs. 3.21 and 3.22). These shear zones 1) have fewer faults, and 2) do not extend as far south as the surface faulting observed in the shear zone of the Standard Model (Figs. 3.21 and 3.22).

South of the faults in the shear zones of the N5°W Model and the N10°W Model, NW-trending shadows (cast inside of broad undulations on the models' surface) reveal the presence of NW-trending depressions that have limited faulting; however, the Standard Model lacks such a NW-trending depression (Fig. 3.23).

4. DISCUSSION

4.1. Summary of modeling results and comparisons to other models

4.1.1. Influence of putty thickness and distribution

The thickness of the ductile layer varied in the Standard Model, Thin Putty Model, and No-Putty Model. The models show that as thickness of the highly ductile unit (putty in the models, salt or overpressured shale in nature) increases, the degree of decoupling between shallow and deep structures increases, and deformation becomes more distributed (Fig. 4.1). Withjack and Callaway (2000) came to the same conclusion for models investigating the cover deformation above an upward-propagating normal fault (Fig. 4.2).

Figure 4.3 explores how the presence or absence of a ductile unit above the rigid block influences the style of deformation. In the Putty-on-Discontinuity Model where putty is present on both sides of the discontinuity, more decoupling occurs between deep and shallow structures than in the Standard Model, where putty is present on only one side of the discontinuity. In addition, the deformation in the extensional domain is more distributed in the Putty-on-Discontinuity Model than in the Standard Model.

The Variable-Putty Model (Fig. 4.4) further demonstrates the effect of putty thickness on the degree of decoupling between deep and shallow structures. It shows that an asymmetrical distribution of putty (salt or overpressured shale in nature) yields an asymmetrical deformation pattern. Specifically, the extensional deformation occurs in a broader zone (offset from the edge of the mylar sheet)

where the putty is thicker, and is more focused above the edge of the mylar sheet where the putty is thinner.

The Layered Model (Fig. 4.5) shows that: 1) faults do not nucleate directly above the rigid block at depth; 2) faults are more numerous at the base of the clay than at the top; and 3) like the top of the Thin-Putty Model, the base of the Layered Model has both NNE-striking faults produced by right-lateral shear along the N-striking discontinuities and ENE-striking extensional faults produced by the northerly displacement of the mylar sheet. Fault orientations in the shear zone are slightly different at the base of the model compared to the top. At the base, faults in the shear zone have orientations that are more N-striking with increasing proximity to the discontinuity, whereas faults that are present at the surface are more oblique to the discontinuity.

Deformation at or near the shear-dominated discontinuity is similar to that in other experimental models with strike-slip deformation (Fig. 4.6). In Ginting's (2013) model, brittle deformation occurs on both sides of the basal discontinuity. In contrast, deformation in the Standard Model and Putty-on-Discontinuity Model occurs above and to the west of the basal discontinuity, where putty is present and/or thicker. Viscous flow and thinning of the putty promotes subsidence on the west side of the discontinuity and produces a component of dip slip for faults in the shear zone. In contrast, faults in Ginting's (2013) model have predominantly strike slip. Ginting's (2013) model contains both R-type and R'-type Riedel shears, whereas the Standard Model and Putty-on-Discontinuity Model only have faults with the orientation of R shears at the surface.

Deformation above the shear-dominated discontinuity in the No-Putty Model is similar to deformation produced in the clay models (without putty) of strike-slip faulting by Schlische et al. (2002) (Fig. 4.7). However, faults in the shear zone of the No-Putty Model rotate easterly with increasing proximity to the southern edge of the mylar sheet; these faults are transitional between the NNE- to N-striking faults above the N-trending discontinuity and the E-striking faults above the southern edge of the mylar sheet.

4.1.2. Orientation of the shear-dominated discontinuity

The orientation of the discontinuity relative to the movement direction of the mylar sheet strongly influences deformation patterns in the cover (Fig. 4.8). In models with highly oblique extension at depth, a shear zone develops parallel to the discontinuity, just like in the Standard Model. However, in models with highly oblique shortening at depth, the trend of the shear zone at the top of the clay does not parallel the discontinuity at depth, and deformation in the extensional domain is less pronounced at the surface.

The model with highly oblique extension at depth (N10°E Model) exhibits primarily NNE-striking right-lateral strike-slip to oblique-slip faults at the northern end of the shear zone. Farther south, the faults strike more easterly (more nearly perpendicular to the displacement direction), reflecting the greater influence of extension produced by northward movement of the southern edge of the mylar sheet.

In the model with highly oblique shortening at depth (N10°W Model), the degree of extensional deformation is suppressed throughout the extensional domain (Fig. 4.8); for example, the maximum heave on extensional faults is considerably less in the N10°W model than for the N0°E (Standard) and N10°E models. A NNE-trending strike-slip fault zone forms subparallel to the movement direction of the mylar sheet (oblique to the discontinuity) in the cover layer. These deformation patterns are markedly different from those produced in a sand model with highly oblique shortening (Fig. 4.9) (McClay et al., 2004). In the sand model, a zone of uplift forms parallel to the basal discontinuity. The sand model does not have a ductile layer, and the surface deformation patterns are strongly coupled to the basal boundary conditions. In the N10°W Model, the putty suppressed both the shortening along the discontinuity and the degree of extension in the extensional domain.

4.2. Application to Jeanne d'Arc basin

The hydrocarbon-bearing Jeanne d'Arc basin (Figs. 1.1a, 4.10a) on the Grand Banks of offshore Newfoundland is a fault-bounded Mesozoic rift basin. As discussed below, the presence of pre-existing zones of weakness, created before and during an initial episode of rifting, and the synrift Argo Salt significantly influenced the development of the basin. Late Triassic to Early Jurassic NW-SE to W-E extension produced activity on the Murre, Mercury and Voyager fault systems (Sinclair, 1995; Serrano Suarez, 2013; Stier, 2016) (Fig. 4.10a-b). The gentle dips of the Murre and Mercury faults at depth (Fig. 1.1a) suggest that they are reactivated

Paleozoic structures (deVoogd et al., 1990). Deposition of the Argo Salt occurred during this initial episode of rifting. Rifting, perhaps episodically, continued throughout the Jurassic (Withjack et al., 2012). During the Early Cretaceous, the Jeanne d'Arc basin underwent NE-SW extension, and NW-striking faults with normal separation (trans-basin faults) formed. Many of these faults detach within the Argo Salt, although others may involve the basement (Sinclair, 1995) (Fig. 4.10c). Some of the pre-existing, NE-striking faults were reactivated as strike-slip (or oblique-slip) faults during this episode of extension (Sinclair, 1995; Serrano Suarez, 2013; Stier, 2016). As in other rift basins with salt, the presence of the Argo Salt decoupled the shallow and deep deformation in the Jeanne d'Arc basin (e.g., Sinclair, 1995; Withjack and Callaway, 2000).

In the experimental models of this study, the edge of the rigid block simulates a pre-existing, deep-seated fault (e.g., the Murre, Mercury, or Voyager fault systems), the putty represents a highly ductile unit (e.g., the Argo Salt), and the clay layer simulates the sedimentary cover above the Argo Salt. In the models, the northward displacement of the mylar sheet produces extension in the putty and clay cover and strike-slip deformation between the putty and clay layer and the rigid block as hypothesized for the Jeanne d'Arc basin. Thus, these models provide templates for the interpretation of the complex fault structures of the Jeanne d'Arc basin.

The Putty-on-Discontinuity Model demonstrates that putty on both sides of a discontinuity (e.g., fault) will cause greater decoupling between shallow and deep structures and a wider distribution of deformation in the extensional domain. Based on these observations, where salt overlies NE-striking fault splays of the Murre

fault, NE-directed movement of the salt would produce a wide distribution of NW-striking trans-basin faults that curve to link with NE-striking faults (Fig. 4.11).

The Variable-Putty Model demonstrates that if salt thickness varies across a basin, the deformation associated with salt mobilization would also vary across the basin. Thus, an initial asymmetrical distribution of Argo Salt in the Jeanne d'Arc basin (i.e., thicker on the northwest side bounded by the Murre fault) would produce an asymmetrical distribution of trans-basin normal faults (Fig. 4.12). Deformation in the central western part of the Jeanne d'Arc basin resembles the deformation in the Variable-Putty Model, suggesting a variable distribution of salt from East to West in this region of Jeanne d'Arc basin.

Two main fault orientations are present in the Terra Nova region of the Jeanne d'Arc basin: N-striking and E-striking (Enachescu, 1987; Sinclair, 1995) (Fig. 4.13). Displacement on many of the younger E-striking faults is greatest where these faults link with N-striking faults (McIntyre et al., 2004). Henza et al. (2009) demonstrated similarities between this fault pattern in the Jeanne d'Arc basin and those in clay models with two phases of non-coaxial extension. However, my models show a similar pattern of N- and E-striking faults in the shear zone of the Thin-Putty Model. Thus, multiple fault trends do not automatically imply that faults formed in multiple phases of deformation; rather, a pre-existing structure at depth can influence the geometry of deformation when salt is involved. Thus, not all of the E-striking faults in the Jeanne d'Arc basin are necessarily younger than the N-striking faults.

Comparisons of the experimental models to the Jeanne d'Arc basin suggest that the Argo Salt flowed (sub)parallel to the NNE-striking Murre and Mercury border faults , producing overlying secondary structures like the trans-basin normal faults and oblique-slip faults. However, the modeling study does not address the cause of the salt mobilization; differential loading, tilting to the NNE, and basement-involved extensional faulting are possible causes.

4.3. Suggestions for future work

This study identified several issues that require further study.

1. The N- and E-striking orthogonal faults form in the shear zone of the Thin-Putty Model. Why does this fault pattern not form on the surface of the Standard Model and the No-Putty Model?
2. Faults that bound basins are commonly the product of the linkage of multiple normal faults. This linkage can result in the formation of a relay ramp between fault segments. How would a segmented rigid block (in the basal boundary conditions) affect the deformation observed at the surface when a ductile unit is mobilized?
3. Discontinuities in the models have vertical dips. Does the dip angle also have an influence?
4. The N5°W Model and the N10°W Model featured highly oblique shortening between the N-directed movement of the mylar sheet and the oblique orientation of the rigid block at depth; however, the surface deformation for these models does not contain evidence of oblique shortening (e.g. pop-up

structures, anticlines, thrust faults). At what angle of oblique shortening will a model (with similar boundary conditions to this series) produce shortening features at the top of the clay?

5. CONCLUSIONS

The experimental (analog) models in this thesis investigate the style of cover deformation (simulated with wet clay) related to the mobilization of synrift salt (simulated with silicone polymer). When a synrift ductile unit flows parallel to the strike of a pre-existing basin-bounding or other basement-involved fault (which control the thickness of the ductile unit), two zones of deformation form within the sedimentary cover: 1) a shear zone with oblique-slip faults that trends (sub)parallel to the strike of the underlying faults (reactivated with a large component of strike slip); and 2) an extensional domain with predominantly normal faults that strike (sub)perpendicular to the flow direction of the ductile unit. At the surface of the clay, some faults in the shear zone and extensional domain link, forming curved faults with displacement maxima at or near the site of linkage. In some models, an orthogonal set of faults develops in this region.

The following remarks summarize the other substantial findings of this work:

1. When the subsalt pre-existing fault is reactivated in strike-slip and even mild transpression, the faults at the clay surface initiate with the orientation of R-type Riedel shears in the shear zone, but R'-type Riedel shears are not present. The shear-zone faults initiate or evolve into oblique-slip faults that always have a normal component of slip, most likely related to the subsidence of the clay that occurs in the extensional domain. This contrasts with the shear zone in the No-Putty Model, which is a strike-slip fault zone with alternating push-ups and pull-aparts related to bends and step-overs.

2. The initial thickness and distribution of the highly ductile unit affect the development of secondary structures in the overlying cover. The thickness of the ductile unit controls the degree of decoupling between shallow and deep structures (in agreement with the modeling results of Withjack and Callaway, 2000). An initially thicker ductile unit produces more decoupling between shallow and deep structures, producing both a broad extensional domain (in the direction of flow of the highly ductile unit) and a broad shear zone (in the direction normal to flow of the highly ductile unit). Varying the initial distribution of the ductile unit produces subsequent asymmetrical deformation in the overlying cover, with the extensional domain broadening as the thickness of the ductile layer increases. Faults at the surface are less numerous than faults at the base of the sedimentary cover that overlies the ductile unit. In cross section, the shear zone has steeply dipping faults, and the extensional domain has domino-style normal faults.
3. The orientation of a pre-existing fault, relative to the flow direction of the highly ductile unit, influences the development of secondary structures. When the flow of the ductile unit (relative to the pre-existing fault) produces highly oblique extension at depth, deformation is distributed broadly in the extensional domain, and the shear zone trends above and parallel to the underlying pre-existing fault. However, when the flow of the ductile unit (relative to the pre-existing fault) produces highly oblique shortening at depth, (a) the trend of the shear zone in the cover is not parallel to the orientation of the underlying pre-existing fault, and (b) secondary features in

the extensional domain are muted in the clay. I infer that the ductile unit distributes the deformation and, thus, inhibits the expression of shortening in the shear zone and normal faults in the extensional domain. However, I only investigated up to 10° of obliquity, and it is unclear if and when evidence of surface shortening would have an expression and/or completely mute the extensional structures.

4. Although the cause of salt flow in the Jeanne d'Arc basin is unknown (it may be triggered by regional tilting, differential loading, and/or by deep-seated extension), comparisons of the experimental models to the Jeanne d'Arc basin suggest that the Argo Salt flowed (sub)parallel to the NE-striking Murre and Mercury border faults, producing NW-striking faults with normal separation (trans-basin faults) that locally curve into parallelism with NE-striking basement-involved faults. In addition, an initial asymmetrical distribution of salt across a basin can produce an asymmetrical distribution of trans-basin faults upon salt mobilization; this resembles the trans-basin fault pattern in the Jeanne d'Arc basin, and supports current interpretations of the basin's kinematic history as well as the initial salt distribution and subsequent salt flow. The presence of coeval orthogonal faults produced during the flow of the highly ductile unit in some experimental models raises the possibility that not all of the E(NE)-striking faults in the Jeanne d'Arc basin are younger than the N(NE)-striking faults.

6. REFERENCES

Byerlee, J. "Friction of rocks." Pure and Applied Geophysics 116.4-5 (1978): 615-626.

Del Ventisette, C., Montanari, D., Sani, F., and Bonini, M. “Basin inversion and fault reactivation in laboratory experiments.” Journal of Structural Geology 28 (2006): 2067-2083.

de Voogd, B., Keen, C. E., and Kay, W. A. "Fault reactivation during Mesozoic extension in eastern offshore Canada." Tectonophysics 173.1 (1990): 567-580.

Durcanin, M. A. “Influence of synrift salt on rift-basin development: Application to the Orpheus basin, offshore Eastern Canada.” M.S. Thesis. Rutgers University-Graduate School-New Brunswick, 2009.

Eisenstadt, G., and Sims, D. "Evaluating sand and clay models: do rheological differences matter?" Journal of Structural Geology 27.8 (2005): 1399-1412.

Enachescu, M. E. "Tectonic and structural framework of the northeast Newfoundland continental margin." Canadian Society of Petroleum Geologists 12, *eds* Beaumont, C., Tankard, A. (1987): 117-146.

Gartrell, A., Hudson, C., and Evans, B. “The influence of basement faults during extension and oblique inversion of the Makassar Straits rift system: Insights from analog models.” AAPG Bulletin 89 (2005): 495-506.

Ginting, P. C. S. “Influence of pre-existing strike-slip faults on fault development during a subsequent phase of extension.” M.S. Thesis. Rutgers University-Graduate School-New Brunswick, 2013.

Handin, J. "Section 10: strength and ductility." Geological Society of America Memoirs 97 (1966): 223-290.

Henza, A. A., Withjack, M. O., and Schlische, R. W. "Normal-fault development during two phases of non-coaxial extension: An experimental study." Journal of Structural Geology 32.11 (2010): 1656-1667.

Hubbert, M. K. "Theory of scale models as applied to the study of geologic structures." Geological Society of America Bulletin 48.10 (1937): 1459-1520.

Hudec, M. R. and Jackson, M. P. A. “The salt mine: a digital atlas of salt tectonics.” The University of Texas at Austin, Bureau of Economic Geology, Udden Book Series No. 5; AAPG Memoir 99 (2011): 1-305.

Koyi, H. A., and Sans, M. "Deformation transfer in viscous detachments: comparison of sandbox models to the South Pyrenean Triangle Zone." Geological Society, London, Special Publications 253.1 (2006): 117-134.

McClay, K., Muñoz, J. and García-Senz, J. "Extensional salt tectonics in a contractional orogen: A newly identified tectonic event in the Spanish Pyrenees." Geology 32.9 (2004): 737-740.

McIntyre, J., DeSilva, N., and Thompson, T. "Updated regional mapping of Jeanne d'Arc Basin based on released 3-D seismic data: Canada-Newfoundland Offshore Petroleum Board." Open file GP-CNOPB-04-01 (2004).

Schlische, R. W., Withjack, M. O. and Eisenstadt, G. "An experimental study of the secondary deformation produced by oblique-slip normal faulting." AAPG Bulletin 86.5 (2002): 885-906.

Serrano Suarez, B.E. “Evolution of the Jeanne d'Arc basin, offshore Newfoundland, Canada: 3D seismic evidence for> 100 million years of rifting.” M.S. thesis. Rutgers University-Graduate School-New Brunswick, 2013.

Sinclair, I. K. "Transpressional inversion due to episodic rotation of extensional stresses in Jeanne d’Arc Basin, offshore Newfoundland." Geological Society, London, Special Publications 88.1 (1995): 249-271.

Stier, N. E. “3D seismic evidence for multiple movement directions and detached extension during Mesozoic rifting in the Jeanne d'Arc basin, offshore Newfoundland, Canada.” M.S. thesis. Rutgers University-Graduate School-New Brunswick, 2016.

Vendeville, B. C., Hongxing Ge, and M. P. A. Jackson. "Scale models of salt tectonics during basement-involved extension." Petroleum Geoscience 1.2 (1995): 179-183.

Weijermars, R., Jackson, M.P.A. , and Vendeville, B. "Rheological and tectonic modeling of salt provinces." Tectonophysics 217.1-2 (1993): 143-174.

Withjack, M. O., and Callaway, S. "Active normal faulting beneath a salt layer: an experimental study of deformation patterns in the cover sequence." AAPG Bulletin 84.5 (2000): 627-651.

Withjack, M.O., and Schlische, R.W. “A review of tectonic events on the passive margin of eastern North America.” In: Post, P., ed. Petroleum Systems of Divergent Continental Margin Basins: 25th Bob S. Perkins Research Conference, Gulf Coast Section of SEPM (2005): 203-235.

Withjack, M. O., and Schlische, R. W. "Geometric and experimental models of extensional fault-bend folds." Geological Society, London, Special Publications 253.1 (2006): 285-305.

Withjack, M. O., Schlische, R.W., and Henza, A.A. "Scaled experimental models of extension: dry sand vs. wet clay." Houston Geological Survey Bulletin 49:8 (2007): 31-49.

Withjack, M. O., Schlische, R.W., and Olsen, P.E. “Rift-basin structure and its influence on sedimentary systems. In: edited by R. Renaut, R. and Ashley, G.M. eds. Sedimentation in Continental Rifts: Spec. Publ. SEPM Soc. Sediment. Geol. 73 (2002): 57–81.

Withjack, M. O., Schlische, R. W., and Olsen, P.E. "Development of the passive margin of eastern North America: Mesozoic rifting, igneous activity, and breakup." In: Roberts, D.G. and Bally, A.W. eds. Regional Geology and Tectonics: Phanerozoic Rift Systems and Sedimentary Basins 1 (2012): 301.

7. APPENDIX

7.1. Scaling (adapted mostly from Withjack & Callaway, 2000)

This thesis uses wet clay to simulate the sedimentary cover and silicone polymer to simulate a highly ductile unit like salt. As in previous studies, (e.g., Withjack and Callaway, 2000; Eisentadt and Sims, 2005; Withjack and Schlische, 2006; Withjack et al., 2007), wet clay simulates the behavior of upper crustal rocks. It consists primarily of kaolinite (having a grain size <0.005 mm diameter) and 40% water by weight, having the following properties: 1) a density of ~1.55 – 1.60 g cm^{-3}; 2) a coefficient of internal friction of ~0.6; 3) a cohesive strength of ~50 Pa. In order for comparisons with a natural prototype to be legitimate, experimental models must maintain geometric, kinematic, and dynamic similarity with natural systems (Hubbert 1937). Because the strength of upper crustal rocks increases with depth (e.g., Byerlee, 1978), modeling materials must have similar properties. Therefore,

$$\tau = C_0 + \mu\sigma_n \qquad (1)$$

where the variables τ and σ_n represent the shear and normal stresses on potential fault surfaces; C_0 represents the cohesion, and μ represents the coefficient of internal friction. A caveat, however, is that this relationship only holds for the initiation of new faults, not the reactivation of existing faults. In nature, the coefficient of internal friction for sedimentary rocks ranges from ~ 0.55 to 0.85 (e.g., Handin 1966; Byerlee, 1978).

To achieve dynamical similarity, properly scaled experimental models must adhere to two conditions (Weijermars et al., 1993; Vendeville et al., 1995; Withjack and Callaway, 2000). First, the coefficients of internal fiction of the modeling

materials and the rocks in the upper crust must be similar. Second, the following equation must hold:

$$C_0^* = \rho^* \cdot g^* \cdot l^* \quad (2)$$

the model-prototype cohesive strength ratio (C_0^*) must equal the product of the model-prototype ratios of density (ρ^*), gravity (g^*), and length (l^*). The models in this thesis have values of 0.62 and 1.0 for (ρ^*) and (g^*), respectively. Consequently the values of (C_0^*) and (l^*) must be similar to maintain dynamic similarity. Values of C are highly variable in nature. They are typically less than 1 MPa in loosely compacted sedimentary rocks and can be greater than 10 MPa for crystalline rocks (Handin, 1966). Because the wet clay in the models has a cohesive strength of ~ 50 Pa, values of C^* are between 10^{-4} and 10^{-6}. Consequently, l^* varies between 10^{-4} and 10^{-6} in models, with the exact value being a function of the cohesion of the natural prototype. For example, when clay simulates loosely compacted sedimentary rock, 1 cm in the model corresponds to 100 m in nature. However, if the clay simulates crystalline rock, 1 cm corresponds to ~10 km in nature.

Dynamic similarity between natural prototypes and modeling materials that simulate the ductile behavior of salt (viscosity ~10^{16} – 10^{20} Pa s) requires using a viscous silicone polymer that has an effective viscosity μ_m of ~10^4 Pa s (Vendeville et al., 1995; Withjack and Callaway, 2000; Koyi and Sans, 2006).

Withjack and Callaway (2000) note that the following equation satisfies dynamic similarity between the models and natural prototypes (when deformation due to viscous flow occurs):

$$d_r^* = [\rho^* \cdot g^* \cdot (l^*)^2]/\mu^* \quad (3)$$

where d_r^* and μ^*represent model-prototype ratios for displacement rate and viscosity, respectively.

Reformatting equation 3 permits the determination of values for displacement rates in models,

$$d_{rm} = [\rho^* \cdot g^* / \mu_m \ ] \cdot (l^*)^2 \cdot P \qquad (4)$$

where d_{rm} is the displacement rate of the mobile wall of the modeling apparatus, μ_m is the viscosity of the putty unit, and $P = d_{rn} \cdot \mu_n$, the product of the displacement rate of a master normal fault in nature (analogous to the master normal fault that forms in the wet clay above the southern edge of the mylar sheet in the No-Putty Model) and the viscosity of a natural salt layer. Natural displacement rates range from about 1 to 10 mm yr^{-1} (or 10^{-7} to 10^{-8} cm s^{-1}) and salt viscosities range from 10^{16} to 10^{20} Pa s; thus, $P = d_{rn} \cdot \mu_n$ ranges from 10^5 to 10^{12} Pa cm (Withjack and Callaway, 2000). Using the displacement rate for the mobile wall in this study (9 cm h^{-1} or 2.5 x 10^{-3} cm s^{-1}), a midrange scaling factor of 10^{-5} for l^*, and the accepted lower limit for salt viscosity (10^{16} Pa s) yields a value of 2.5 x 10^{-5} cm s^{-1} for the displacement rate of a master normal fault in nature; this value is higher than the accepted range for fault-displacement rates in nature. Using the accepted upper limit for salt viscosity (10^{20} Pa s) yields a natural displacement rate of 2.5 x 10^{-9} cm s^{-1}, which is lower than the accepted natural displacement rates (10^{-7} to 10^{-8} cm s^{-1}). Thus, given the wide range of salt viscosities (10^{16} to 10^{20} Pa s), using a midrange value for salt viscosity would yield an acceptable value for the scaling of the displacement rate of mobile wall to natural fault-displacement rates.

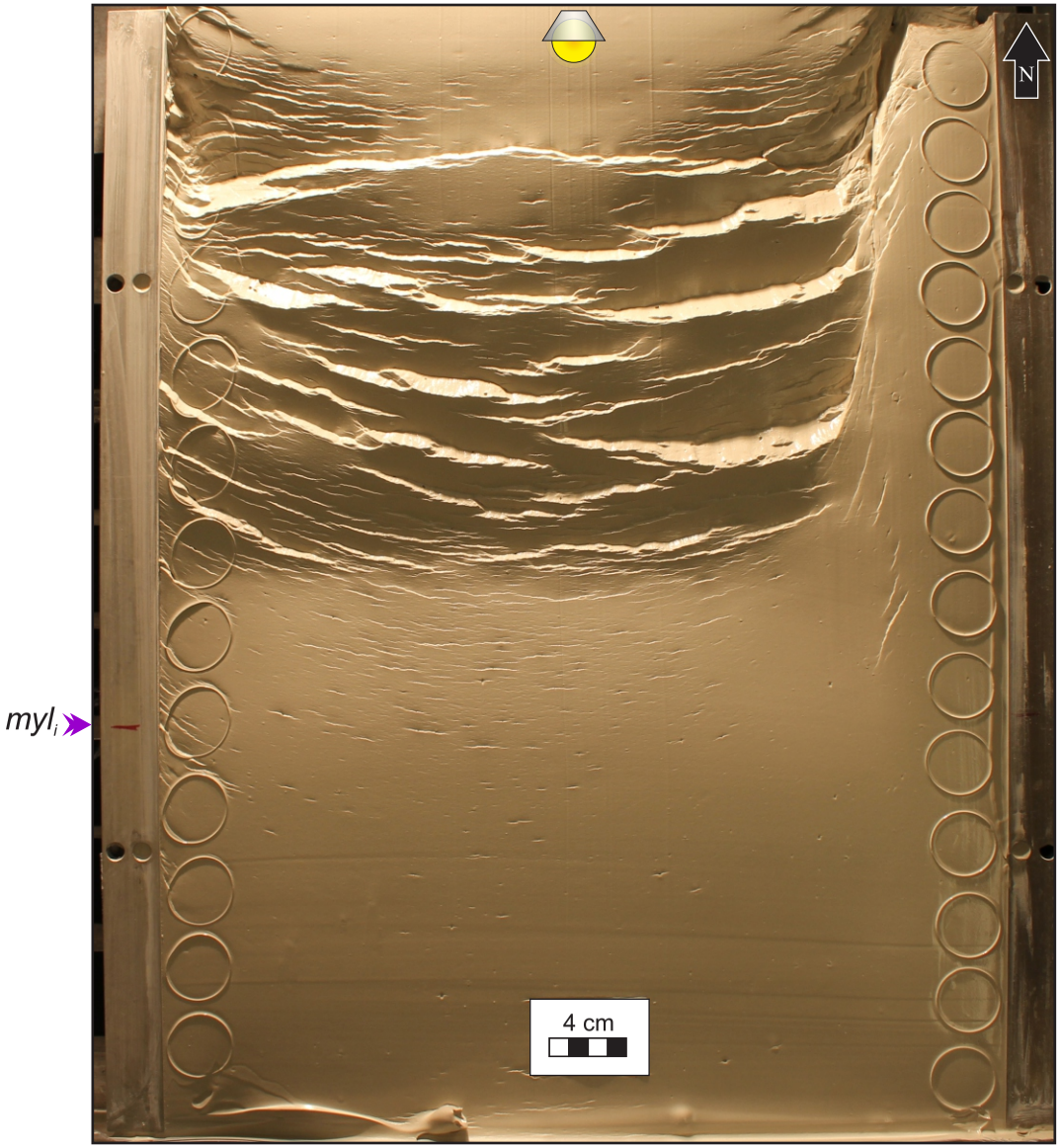

Appendix 7.2.1:
Photograph of Standard Model in plan view at 10.0 cm of displacement. Small purple arrow indicates initial position of edge of mylar sheet (myl_i).

Model Dimensions

Rigid block
Width: 6 cm
Length: 61 cm
Height: 1 cm

Putty unit
Width: 40 cm
Thickness: 1 cm

Clay unit
Width: 46 cm
Length: 61 cm
Thickness: 3 cm

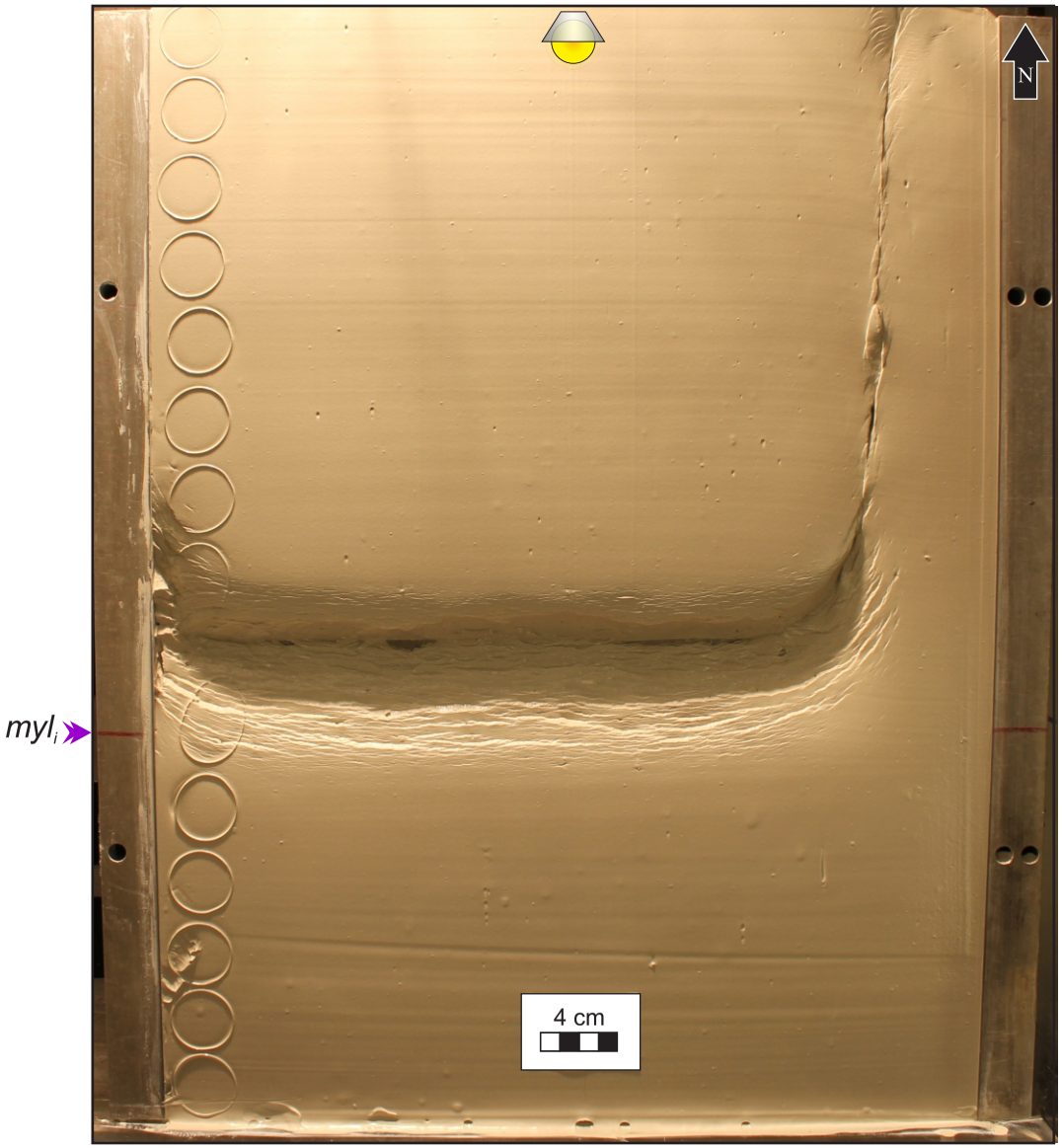

Appendix 7.2.2:
Photograph of No-Putty Model in plan view at 5.0 cm of displacement. Small purple arrow indicates initial position of edge of mylar sheet (myl_i).

Model Dimensions

Mylar sheet
Width: Extends 40 cm eastward from western fixed wall.
Length: 40 cm from north edge of model
Height: negligible

Putty unit
No putty

Clay unit
Width: 46 cm
Length: 61 cm
Thickness: 3 cm

Appendix 7.2.3:
Photograph of Thin-Putty Model in plan view at 10.0 cm of displacement. Small purple arrow indicates initial position of edge of mylar sheet (myl_i).

Model Dimensions

Rigid block
Width: 6 cm
Length: 61 cm
Height: 0.5 cm

Putty unit
Width: 40 cm
Thickness: 0.5 cm

Clay unit
Width: 46 cm
Length: 61 cm
Thickness: 3 cm

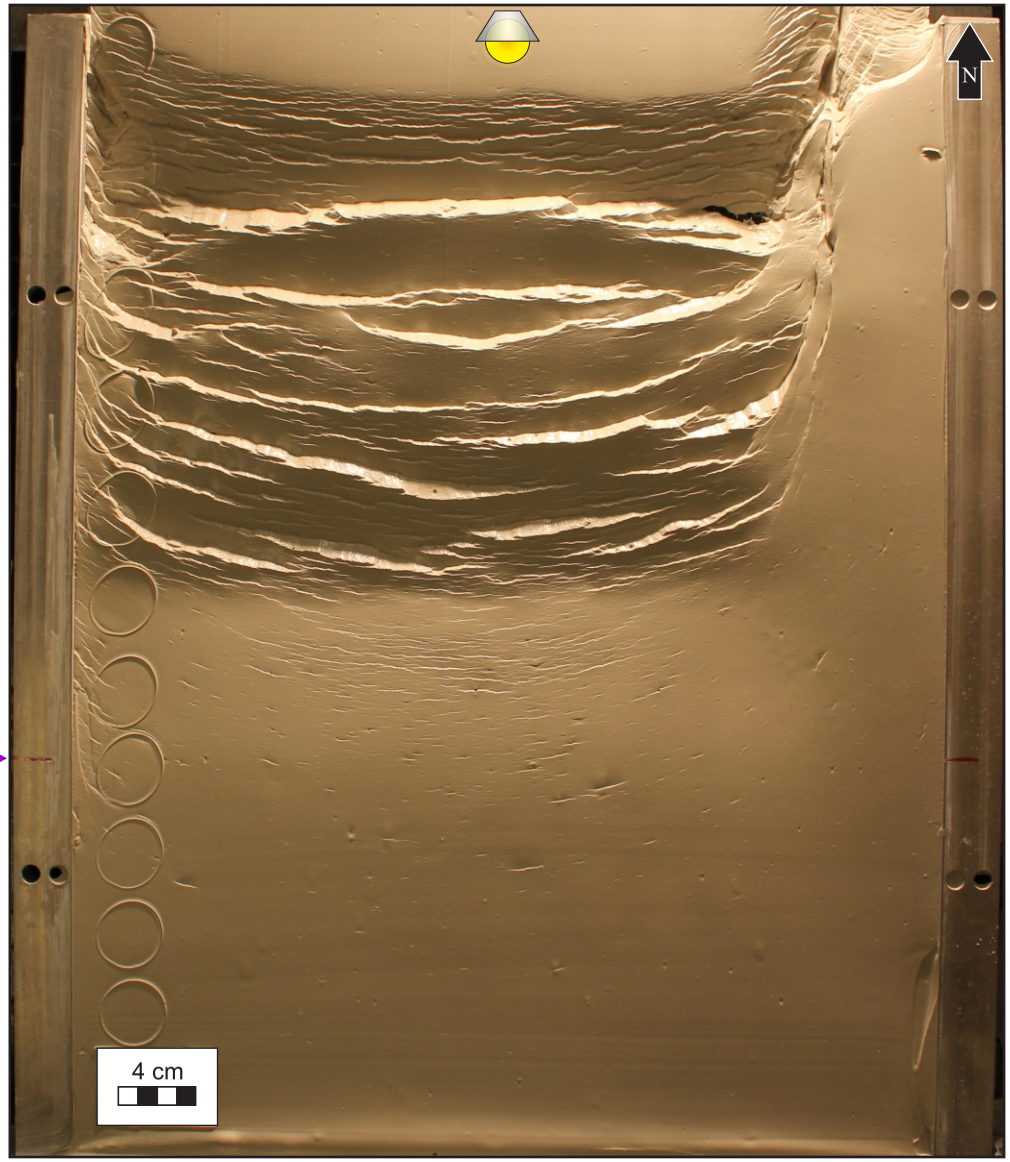

Appendix 7.2.4:
Photograph of Putty-on-Discontinuity Model in plan view at 10.0 cm of displacement. Small purple arrow indicates initial position of edge of mylar sheet (myl_i).

Model Dimensions

Rigid block
Width: 6 cm
Length: 61 cm
Height: 0.5 cm

Putty unit
Width: 40 cm above mylar sheet, 6 cm above rigid block
Thickness: 1 cm above mylar sheet, 0.5 cm above rigid block

Clay unit
Width: 46 cm
Length: 61 cm
Thickness: 3 cm

Appendix 7.2.5:
Photograph of Variable-Putty Model in plan view at 10.0 cm of displacement. Small purple arrow indicates initial position of edge of mylar sheet (myl_i).

Model Dimensions

Rigid blocks (on east and west sides of model)
Width: 6 cm
Length: 61 cm
Height: 1 cm

Putty unit
Width: 40 cm
Thickness: Variable; 1 cm to ~0 cm (west to east)

Clay unit
Width: 52 cm
Length: 61 cm
Thickness: 3 cm

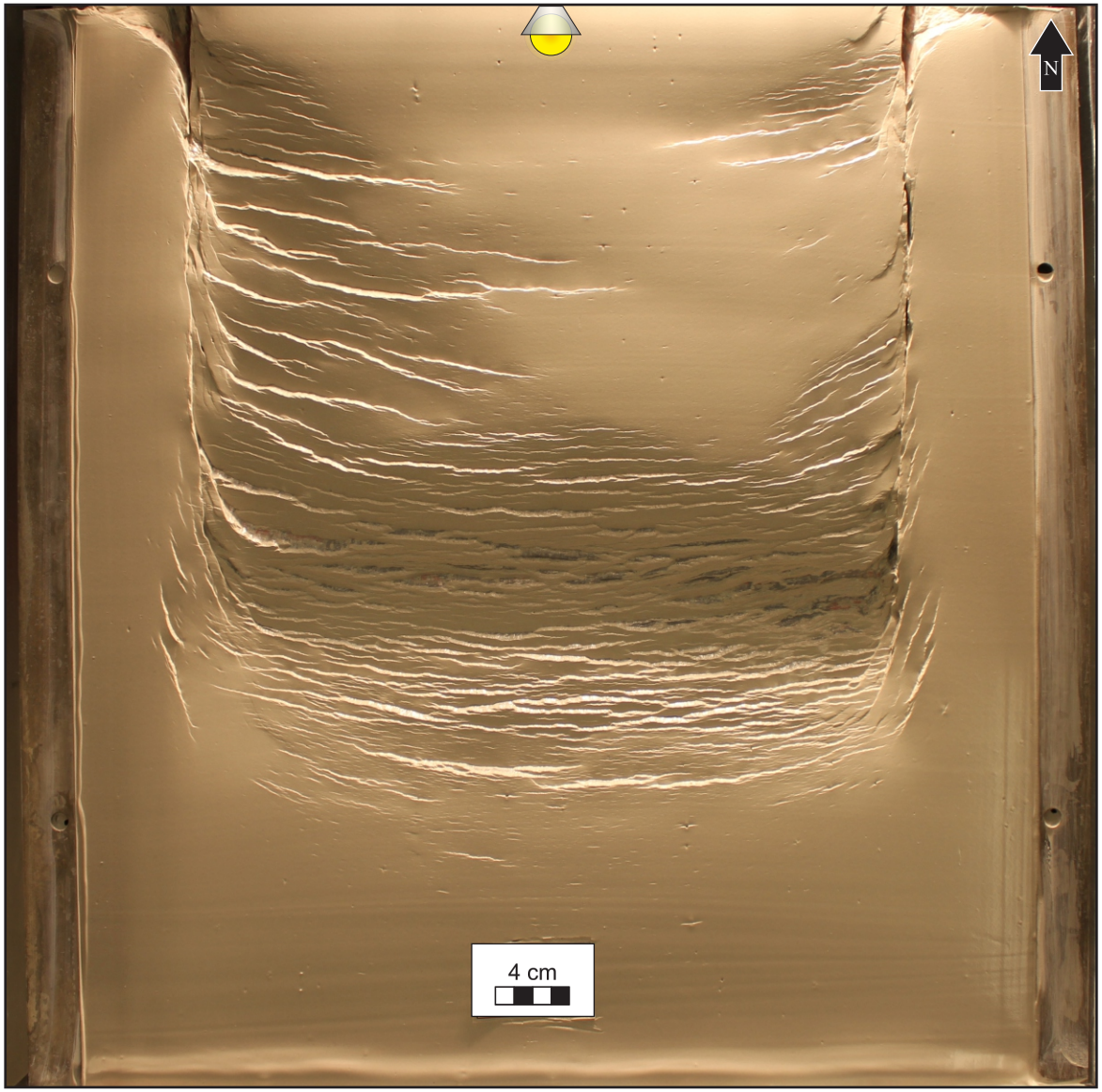

Appendix 7.2.6.1: Photograph of top of Layered Model in plan view at 10.0 cm of displacement. Small purple arrow indicates initial position of edge of mylar sheet (myl_i).

Model Dimensions

Rigid blocks (on east and west sides of model)
Width: 6 cm
Length: 61 cm
Height: 1 cm

Putty unit
Width: 40 cm
Thickness: Variable; 1 cm to ~0 cm (west to east) – intended initial conditions

Clay unit
Width: 52 cm
Length: 61 cm
Thickness: 3 cm

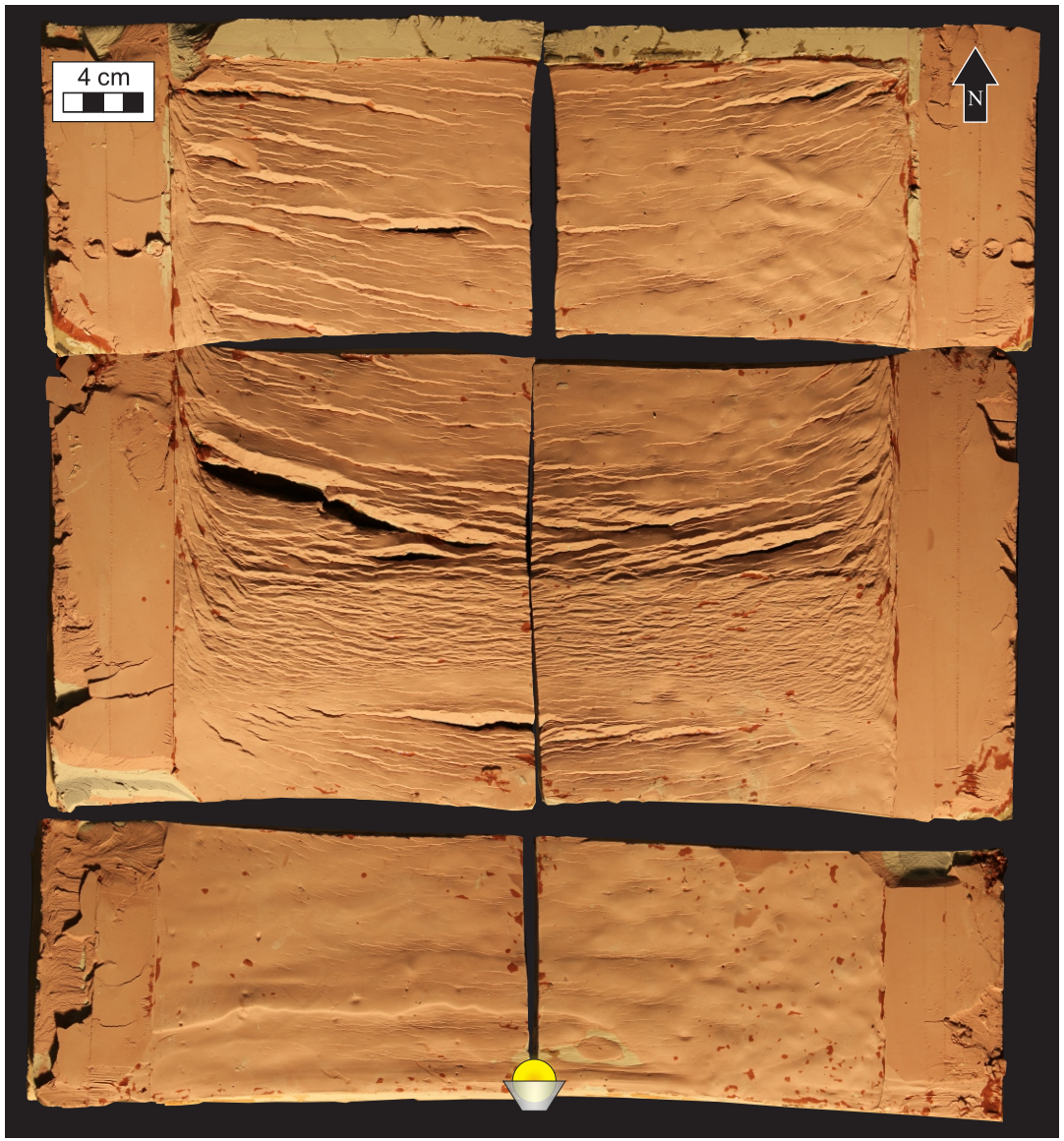

Appendix 7.2.6.2:
Photograph of post-desiccation base of Layered Model in plan view at 10.0 cm of displacement. Dimensions of model are not restored to pre-desiccation values.

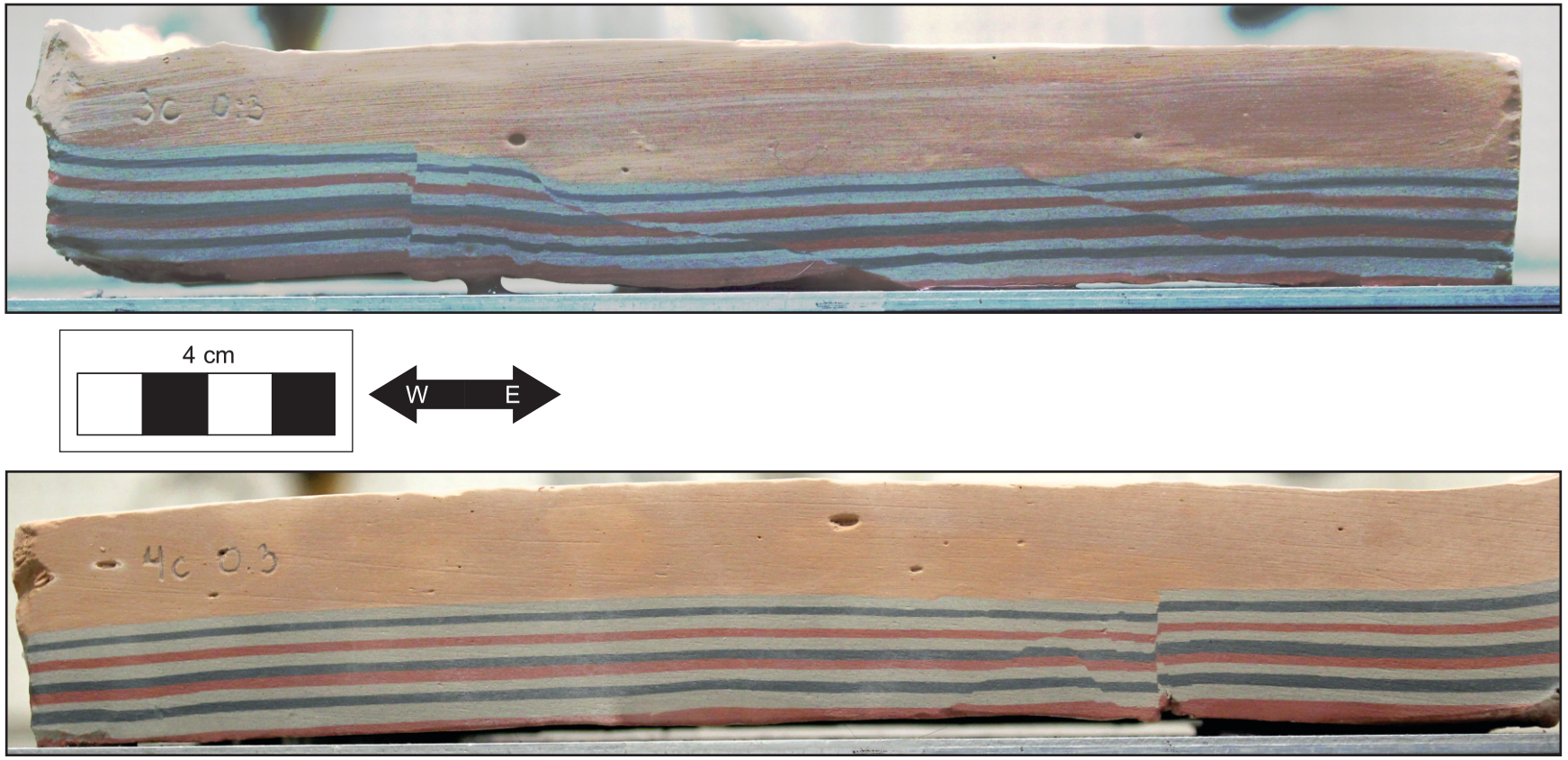

Appendix 7.2.6.3:
Photographs of post-desiccation E-W cross sections of Layered Model at 10.0 cm of displacement. (Top) Western half of section. (Bottom) Eastern half of section. Dimensions of model are not restored to pre-desiccation values. Digital color saturation of photographs enhances contrast between layers of clay. The thick top layer (beige) is the post-kinematic layer of clay.

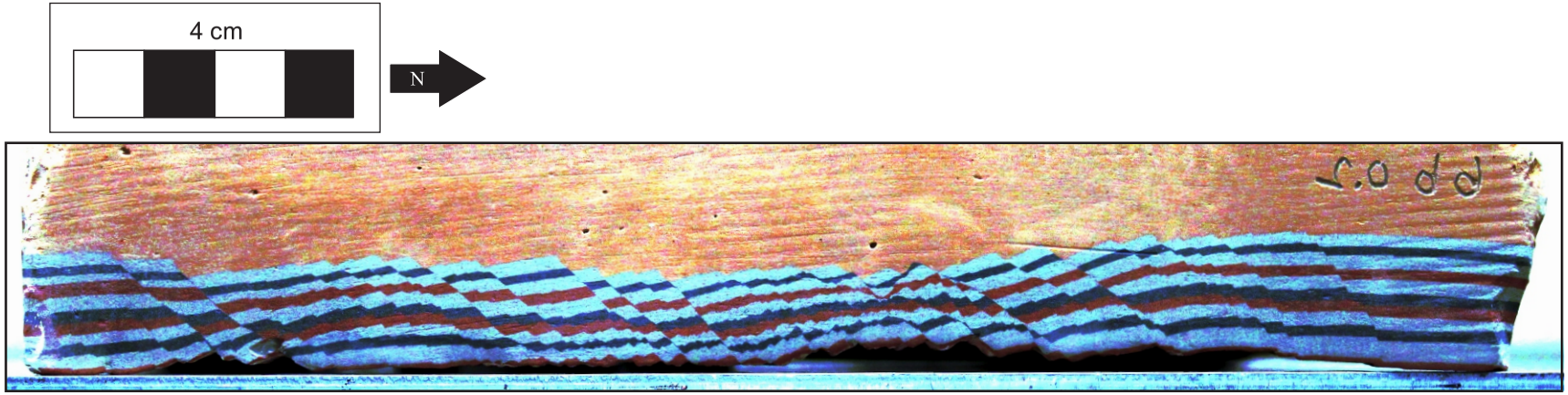

Appendix 7.2.6.4:
Photograph of post-desiccation N-S cross section of Layered Model at 10.0 cm of displacement. Dimensions of model are not restored to pre-desiccation values. Digital color saturation of photograph enhances contrast between layers of clay. The top layer (beige) is the post-kinematic layer of clay.

Appendix 7.2.7:
Photograph of N5°E Model in plan view at 10.0 cm of displacement. Small purple arrow indicates initial position of edge of mylar sheet (myl_i).

Model Dimensions

Rigid block (east side of model)
Width: ~6 cm (north edge), ~11 cm (south edge)
Length: ~61.2 cm (west edge), 61 cm (east edge)
Height: 1 cm

Putty unit
Width: ~38 cm (north), ~34 cm (south)
Thickness: 1 cm

Clay unit
Width: 46.5 cm
Length: 61 cm
Thickness: 3 cm

Appendix 7.2.8:
Photograph of N10°E Model in plan view at 10.0 cm of displacement. Small purple arrow indicates initial position of edge of mylar sheet (myl_i).

Model Dimensions

Rigid block (east side of model)
Width: ~6 cm (north edge), ~17 cm (south edge)
Length: ~62 cm (west edge), 61 cm (east edge)
Height: 1 cm

Putty unit
Width: ~39 cm (north), ~31 (south)
Thickness: 1 cm

Clay unit
Width: 44.5 cm
Length: 61 cm
Thickness: 3 cm

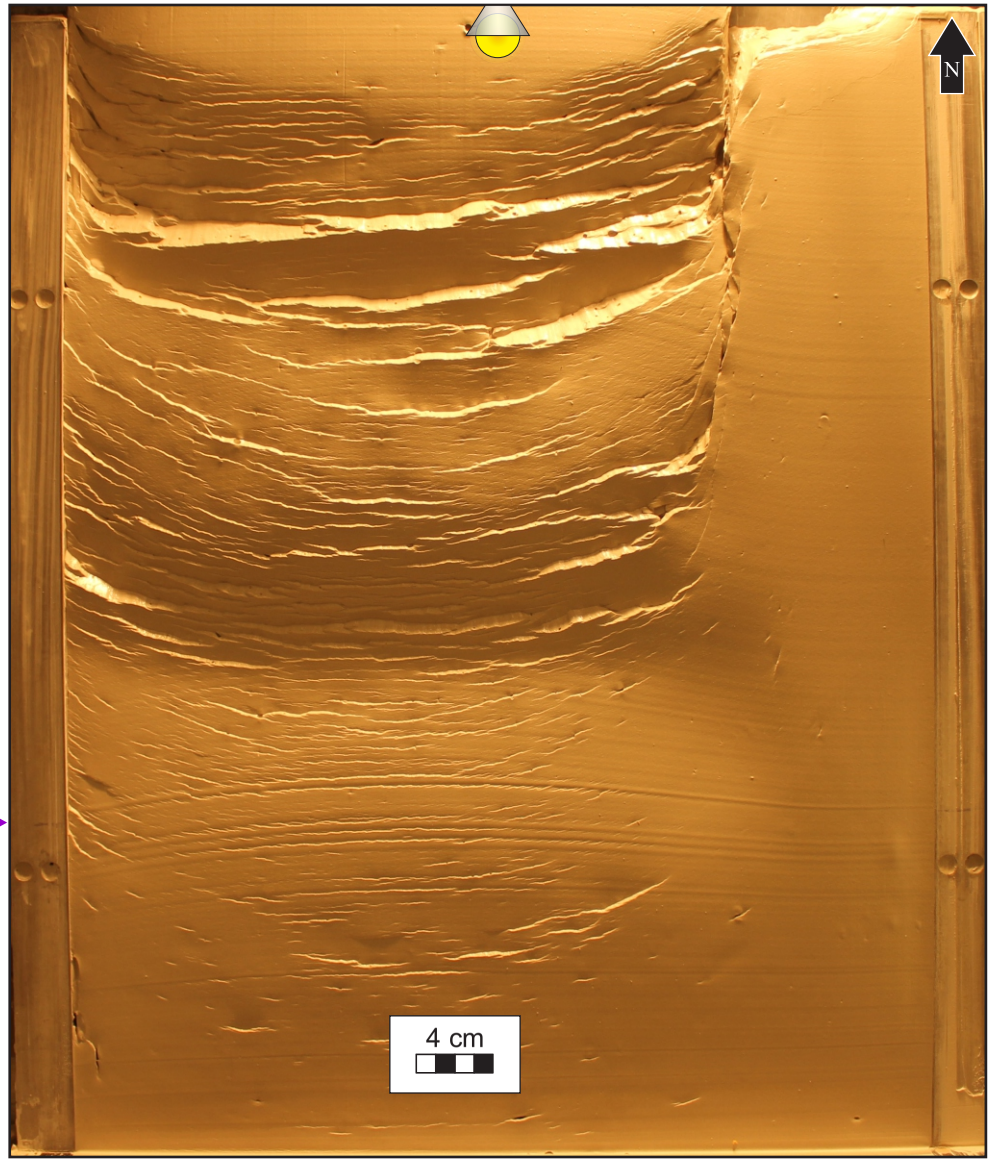

myl_i

Appendix 7.2.9:
Photograph of N5°W Model in plan view at 10.0 cm of displacement. Small purple arrow indicates initial position of edge of mylar sheet (myl_i).

Model Dimensions

Rigid block (east side of model)
Width: ~11 cm (north edge), ~6 cm (south edge)
Length: ~61.2 cm (west edge), 61 cm (east edge)
Height: 1 cm

Putty unit
Width: ~35 cm (north), ~39 cm (south)
Thickness: 1 cm

Clay unit
Width: 44.5 cm
Length: 61 cm
Thickness: 3 cm

Appendix 7.2.10:
Photograph of N10°W Model in plan view at 10.0 cm of displacement. Small purple arrow indicates initial position of edge of mylar sheet (myl_i).

Model Dimensions

Rigid block (east side of model)
Width: ~17 cm (north edge), 6 cm (south edge)
Length: ~62 cm (west edge), 61 cm (east edge)
Height: 1 cm

Putty unit
Width: ~34 cm (north), ~42 cm (south)
Thickness: 1 cm

Clay unit
Width: 48 cm
Length: 61 cm
Thickness: 3 cm

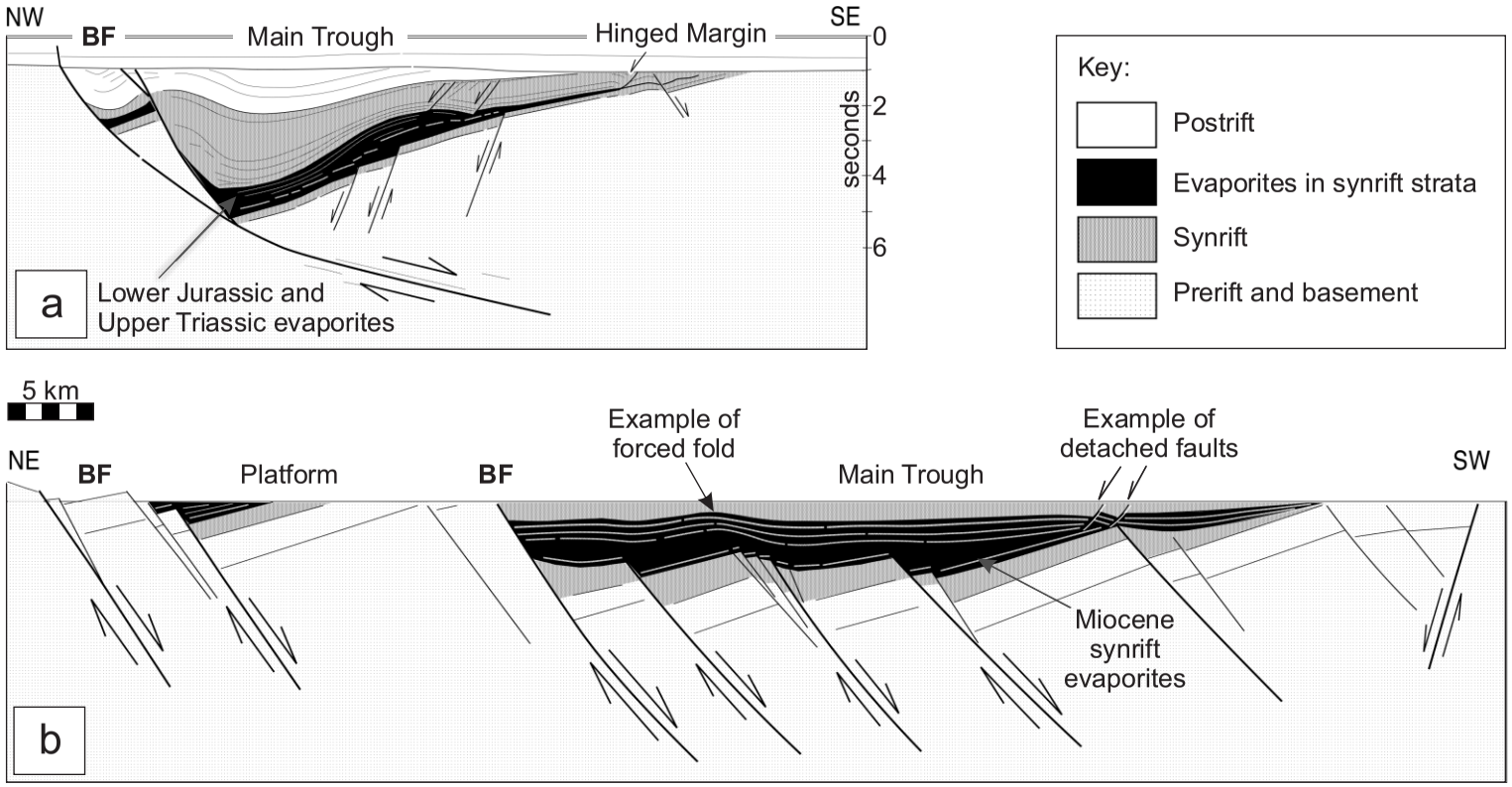

Fig. 1.1: Examples of rift basins in cross-sectional view (modified from Withjack et al., 2002). Displacement on faults controls the thickness and distribution of synrift strata, including evaporites (shown in black) within rift basins. Cross sections have the same horizontal scale and are shown with the border faults (BF) on the left. (a) Line drawing of seismic line 85-4A through the Jeanne d'Arc rift basin, offshore Newfoundland. Line drawing is from seismic line and is displayed without vertical exaggeration assuming a velocity of 4 km/s; vertical axis is in seconds of two-way travel time. (b) Cross section of the Suez rift basin, Egypt (without vertical exaggeration).

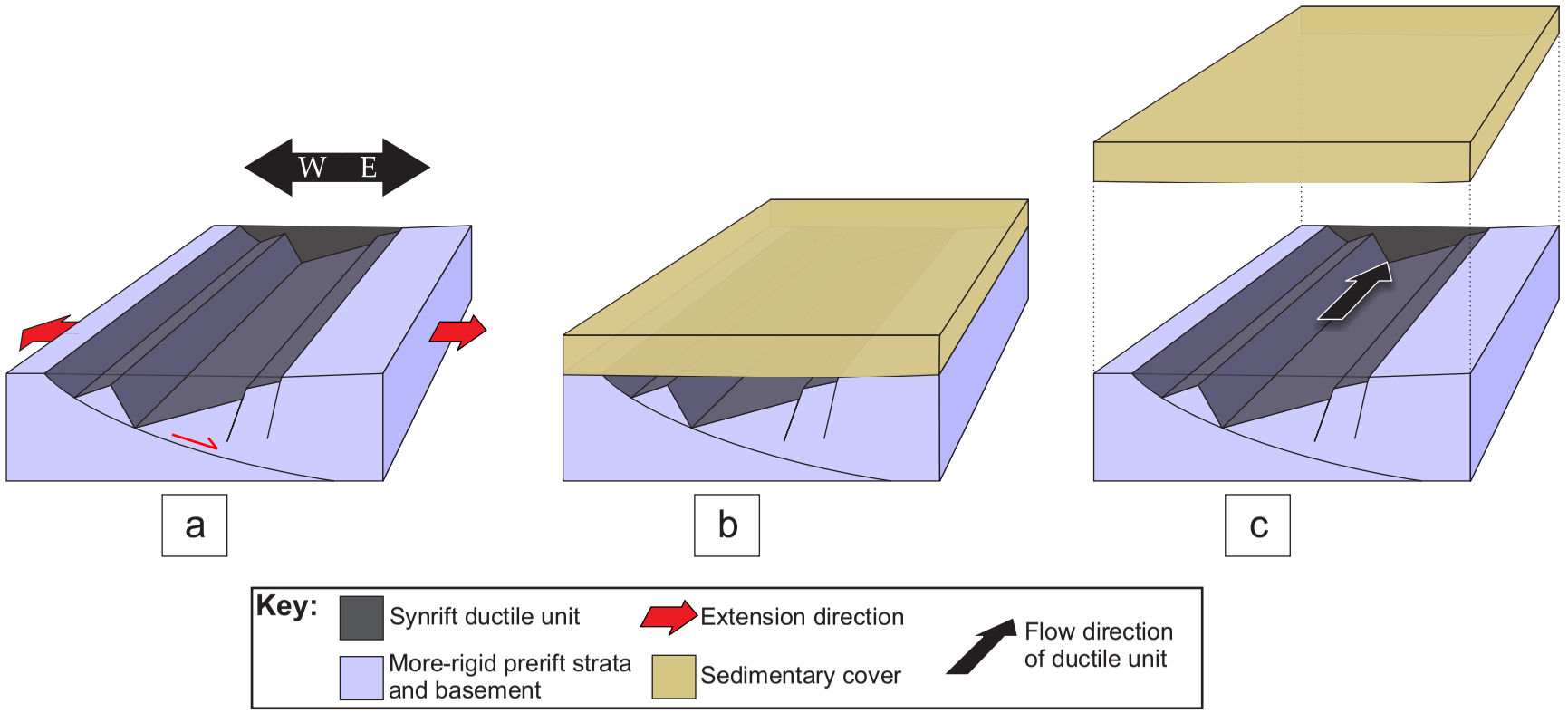

Fig. 1.2: Cartoon of ductile unit flowing parallel to long axis of a rift basin with sedimentary cover. (a) E-W extension produces rift basin with synrift ductile unit. Long axis of basin trends N. Displacement on faults controls thickness and distribution of synrift ductile unit. (b) Deposition of sedimentary cover. (c) Ductile unit flows parallel to N-trending long axis of rift basin.

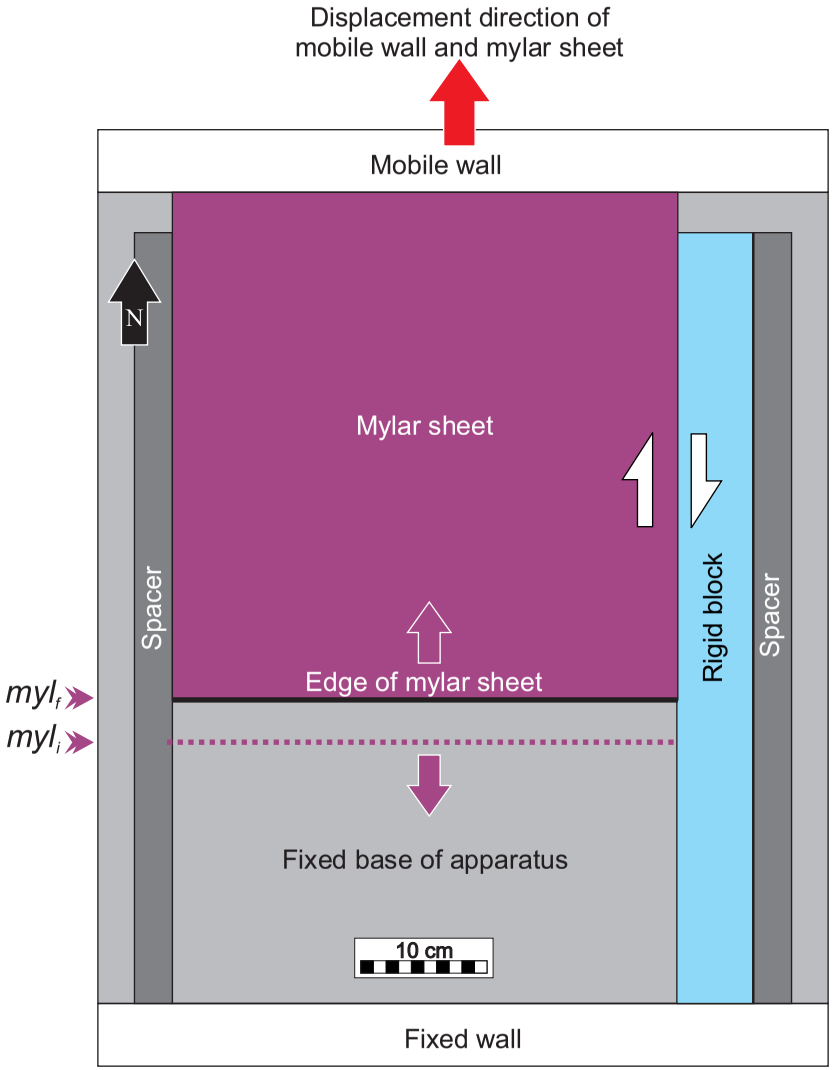

Fig. 2.1: Plan-view diagram of basal boundary conditions and kinematics. Movement of the southern edge of mylar sheet produces N-S extension (large purple arrows). Movement of eastern edge of the mylar sheet produces right-lateral strike-slip (white half arrows) along N-trending edge of rigid block. Small purple arrows indicate initial and final positions of edge of mylar sheet (myl_i and myl_f respectively).

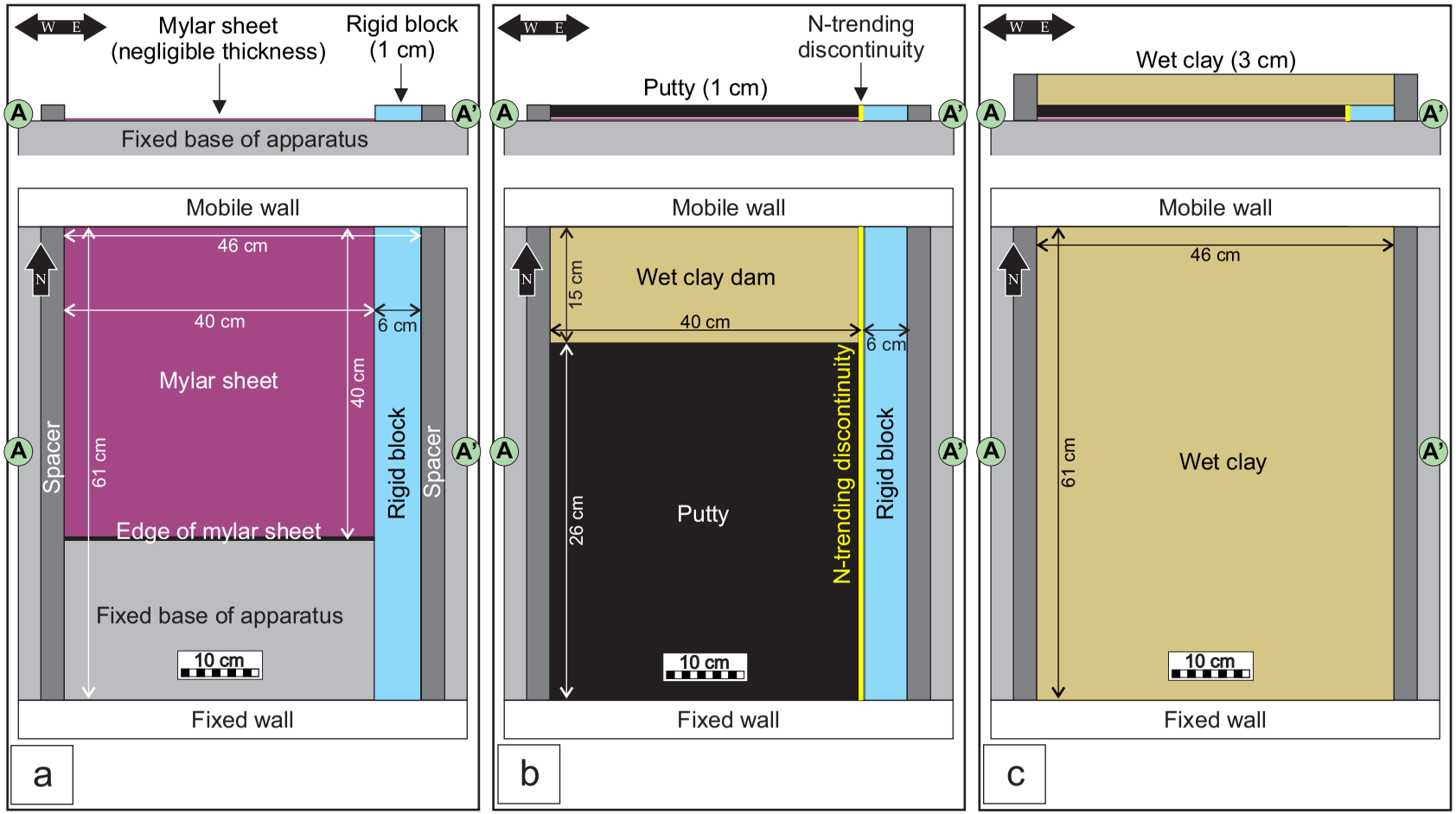

Fig. 2.2: Setup of Standard Model in cross-section and plan views. Cross sections have vertical exaggeration of 1.5. Numbers in parentheses are thicknesses. A-A' in plan view gives location of cross section. (a) Setup at base of model. (b) Setup at top of putty. (c) Setup at top of clay.

Model Name	Putty Thickness (cm)	Thickness of rigid block (cm)	Thickness of wet clay cover (cm)	Trend of Discontinuity	Number of discontinuities related to rigid block(s)
Standard Model	1.0	1.0	3	N	1
Thin-Putty Model	**0.5**	**0.5**	3	N	1
No-Putty Model	**0.0**	**0.0**	3	N	1
Putty-on-Discontinuity Model	**1.0, 0.5 over rigid block**	**0.5**	3	N	1
Variable-Putty Model	**1.0 to ~0.0 (west to east)**	**1.0 (west), 0.0 (east)**	3	N	**2**
Layered Model	**1.0 to ~0.0 (west to east)**	**1.0 (west), 0.0 (east)**	**3 cm of colored layers**	N	**2**
N5°E Model	1.0	1.0	3	**N5°E**	1
N10°E Model	1.0	1.0	3	**N10°E**	1
N5°W Model	1.0	1.0	3	**N5°W**	1
N10°W Model	1.0	1.0	3	**N10°W**	1

Table 2.1: List of models with boundary conditions. Bold type indicates deviations in boundary conditions from those of the Standard Model.

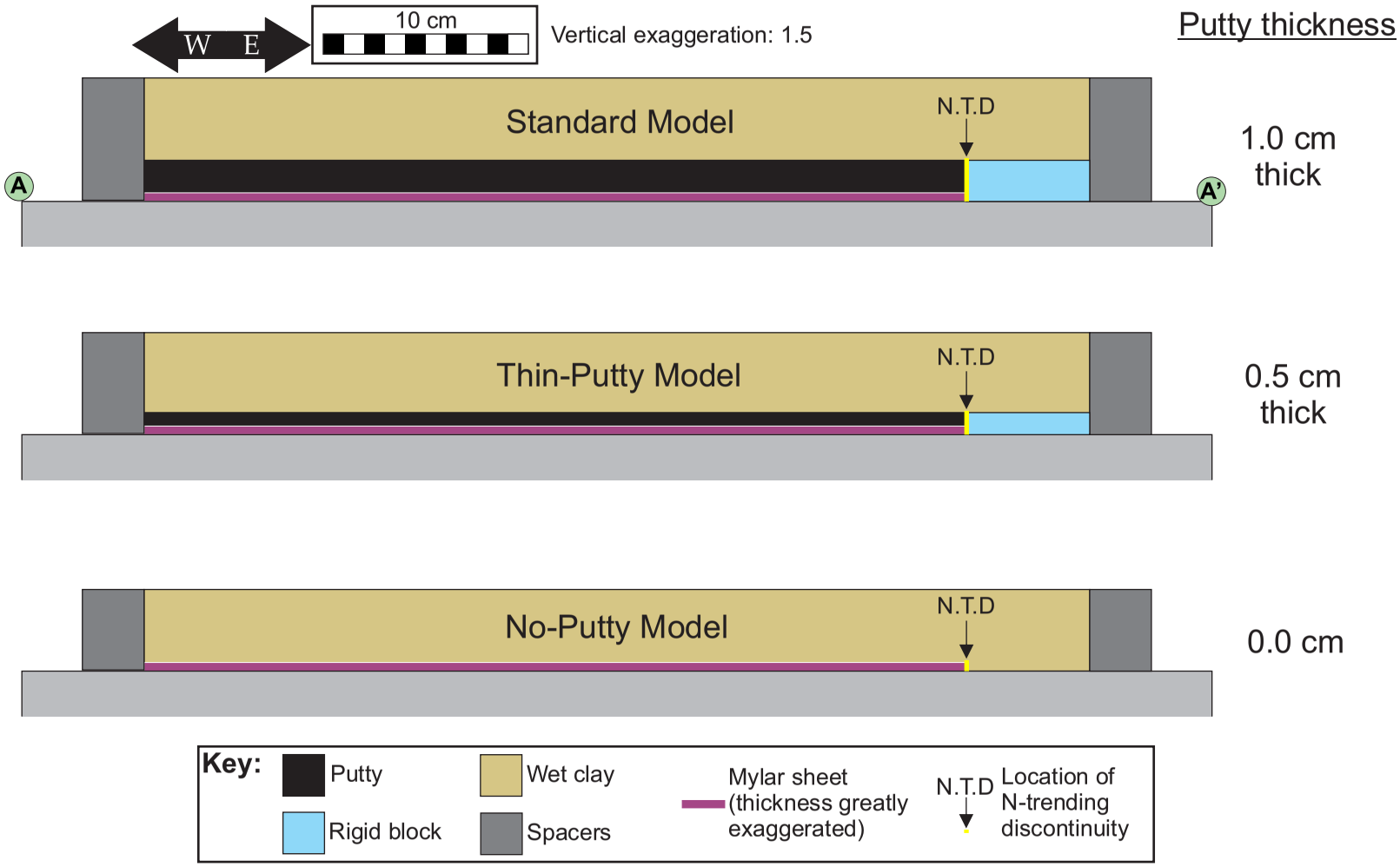

Fig. 2.3: Comparison of setup in cross section for Standard Model, Thin-Putty Model, and No-Putty Model. For location of cross section A-A', see Fig. 2.2c.

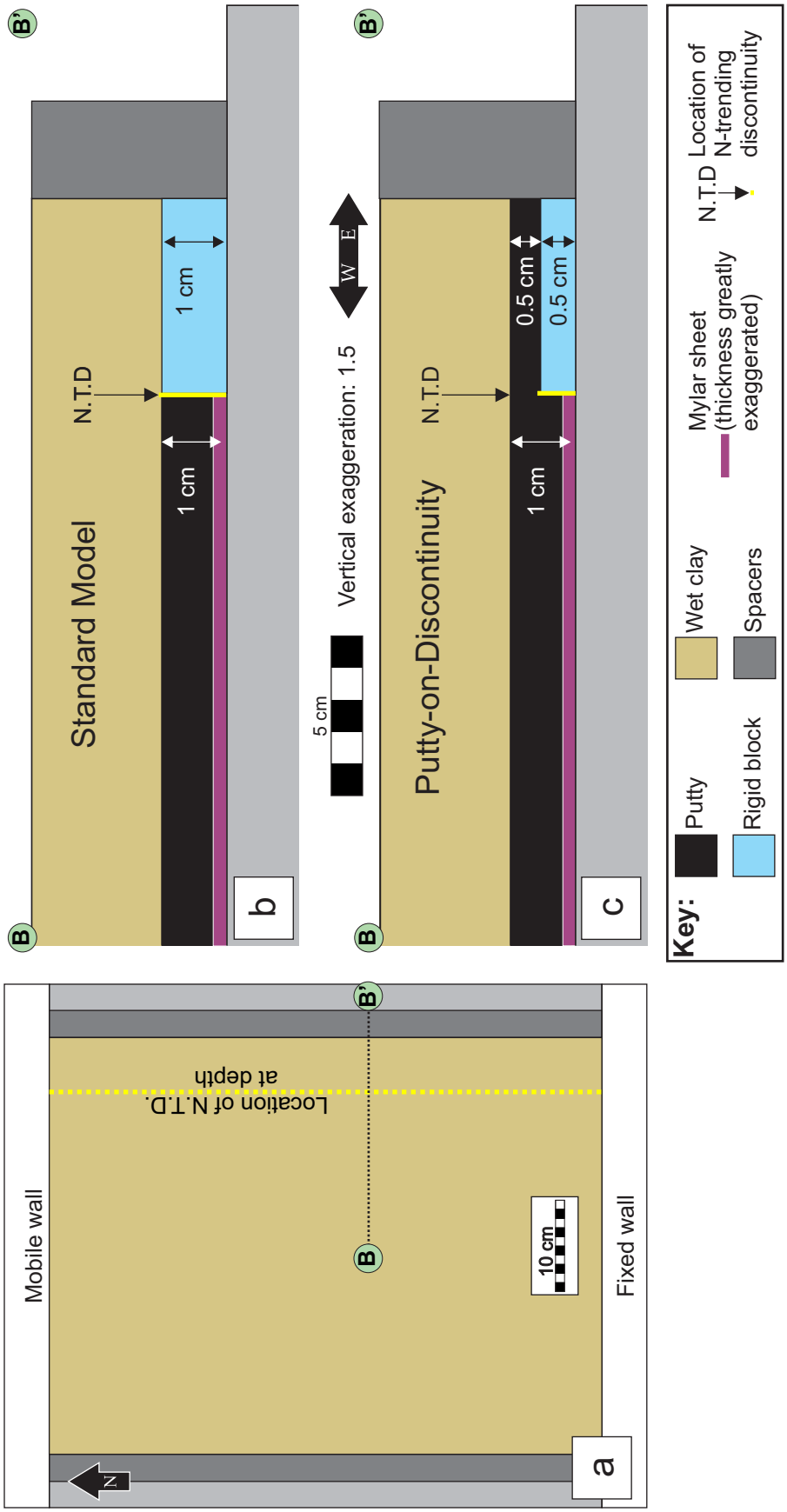

Fig. 2.4: Comparison of setups for Standard Model and Putty-on-Discontinuity Model. (a) Plan view is same for Standard Model and Putty-on-Discontinuity Model. B-B' gives location of sections in (b) and (c), which highlight extent of putty in vicinity of N-trending discontinuity at edge of rigid block. (b) Cross section of Standard Model. (c) Cross section of Putty-on-Discontinuity Model.

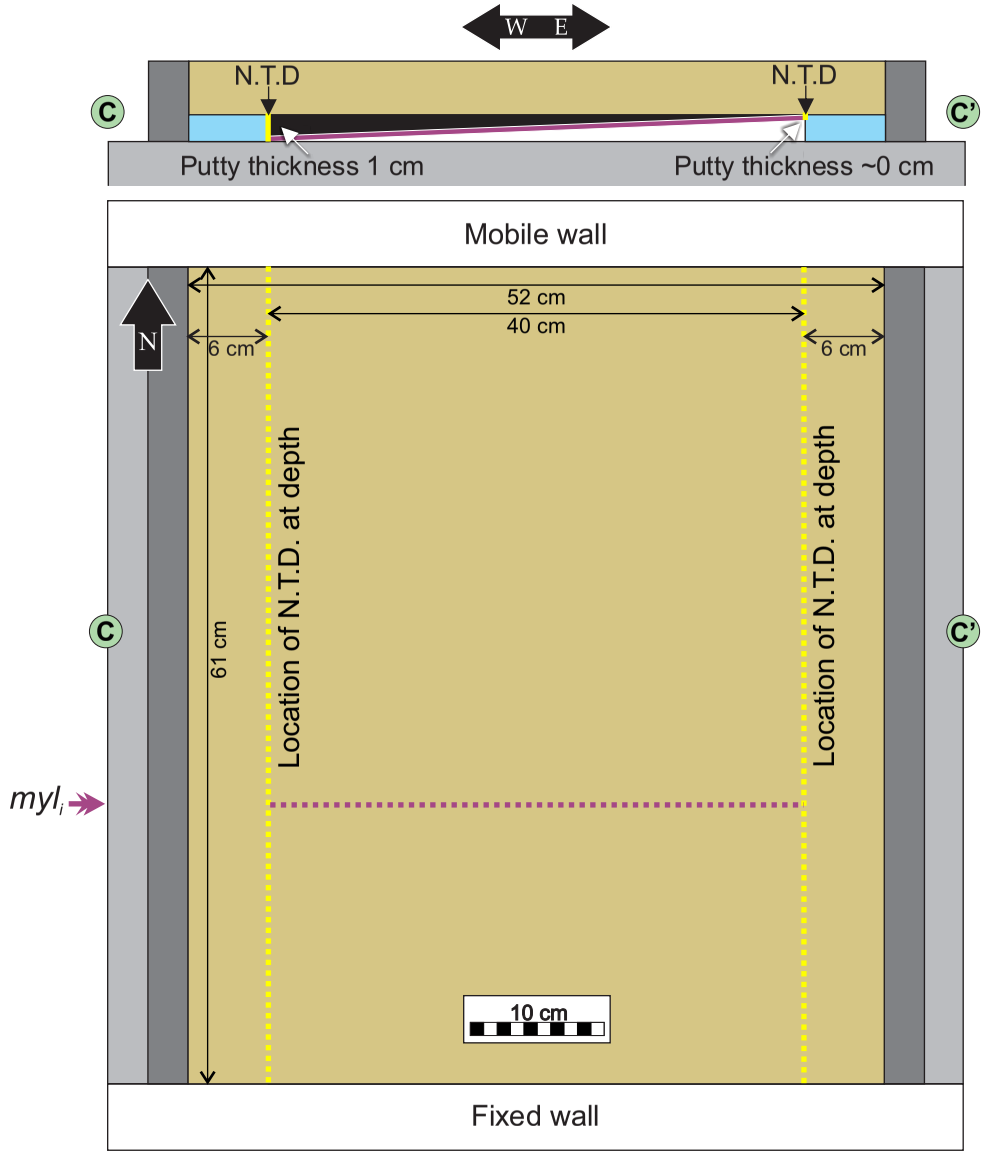

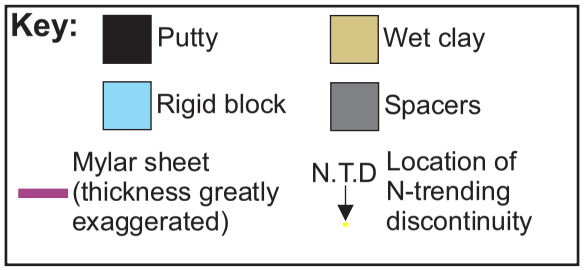

Fig. 2.5: Setup for Variable-Putty Model. (a) Cross section shows two discontinuities and thickness of putty increasing from east to west. Location of cross section C-C' given in (b). (b) Plan-view geometry at top of clay shows position of two N-trending discontinuities. Dashed purple line and purple arrow indicate initial position of edge of mylar sheet (myl_i).

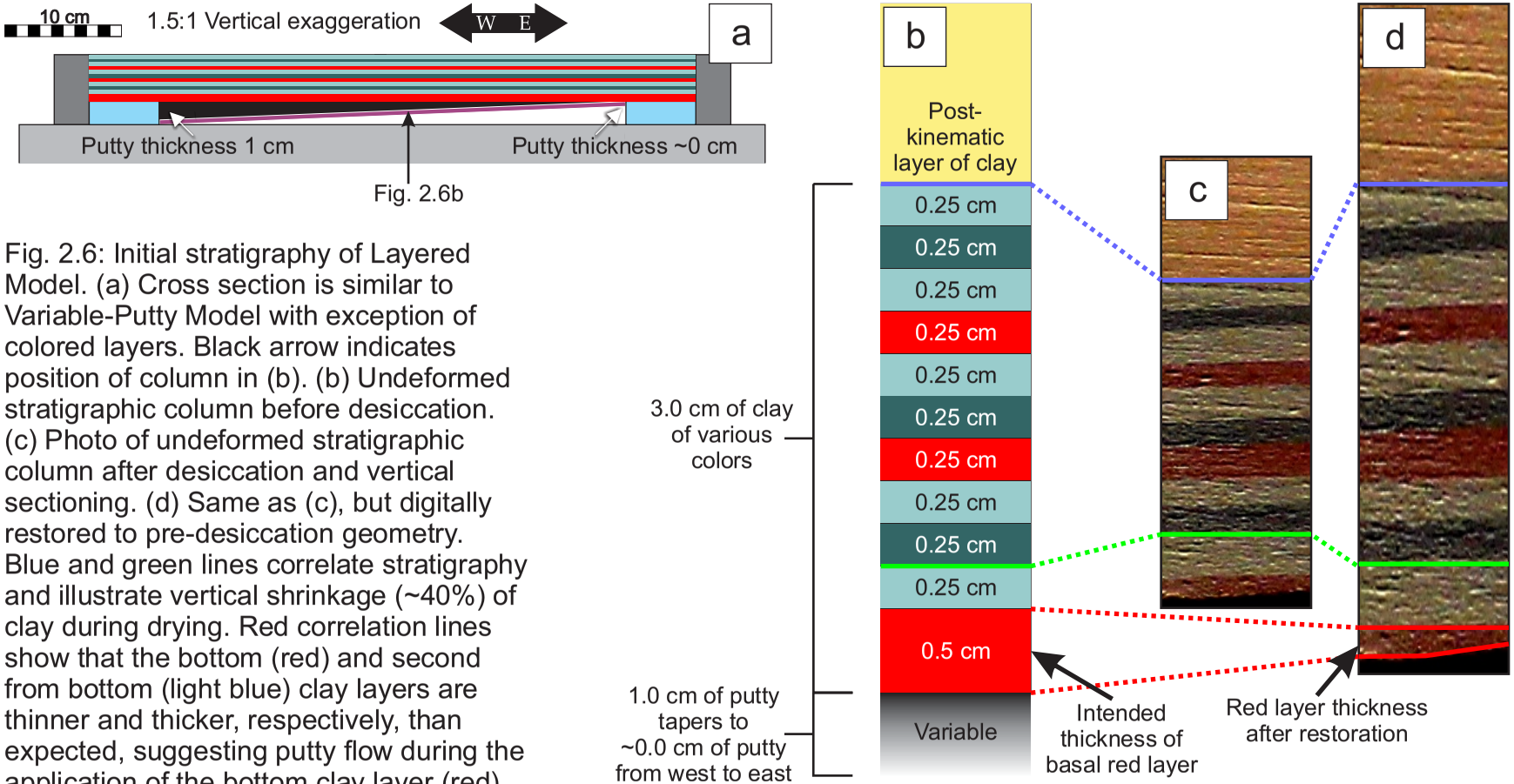

Fig. 2.6: Initial stratigraphy of Layered Model. (a) Cross section is similar to Variable-Putty Model with exception of colored layers. Black arrow indicates position of column in (b). (b) Undeformed stratigraphic column before desiccation. (c) Photo of undeformed stratigraphic column after desiccation and vertical sectioning. (d) Same as (c), but digitally restored to pre-desiccation geometry. Blue and green lines correlate stratigraphy and illustrate vertical shrinkage (~40%) of clay during drying. Red correlation lines show that the bottom (red) and second from bottom (light blue) clay layers are thinner and thicker, respectively, than expected, suggesting putty flow during the application of the bottom clay layer (red).

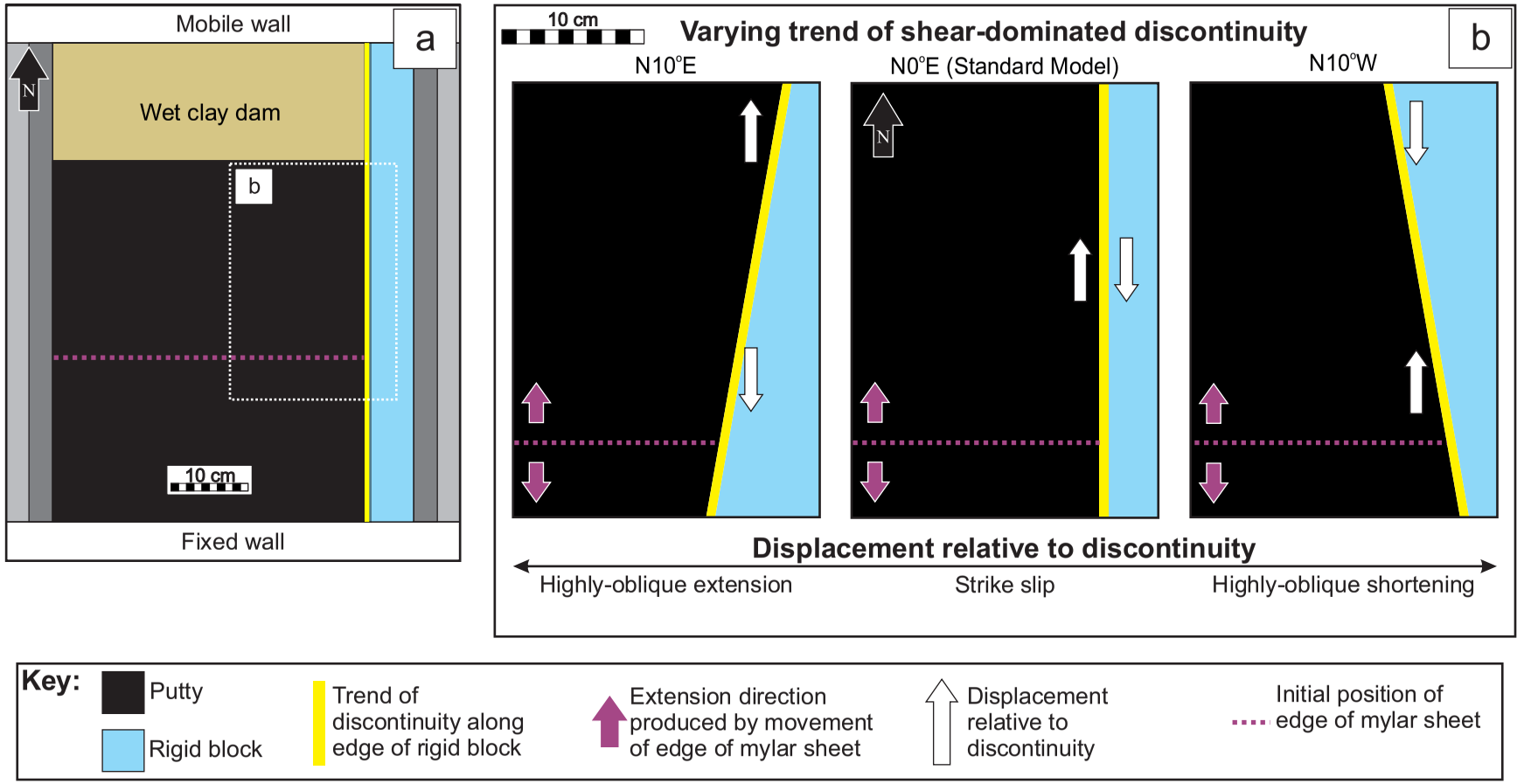

Fig. 2.7: Setup in plan view for models that vary the trend of the shear-dominated discontinuity. (a) Plan view of Standard Model shown at top-of-putty level. Dashed white rectangle shows area enlarged in (b). (b) From left-right: N10°E Model (discontinuity undergoes highly oblique extension), Standard Model (discontinuity undergoes right-lateral strike slip), and N10°W Model (discontinuity undergoes highly oblique shortening). Note that edge of rigid block is straight and continues to fixed wall and mobile wall for each model.

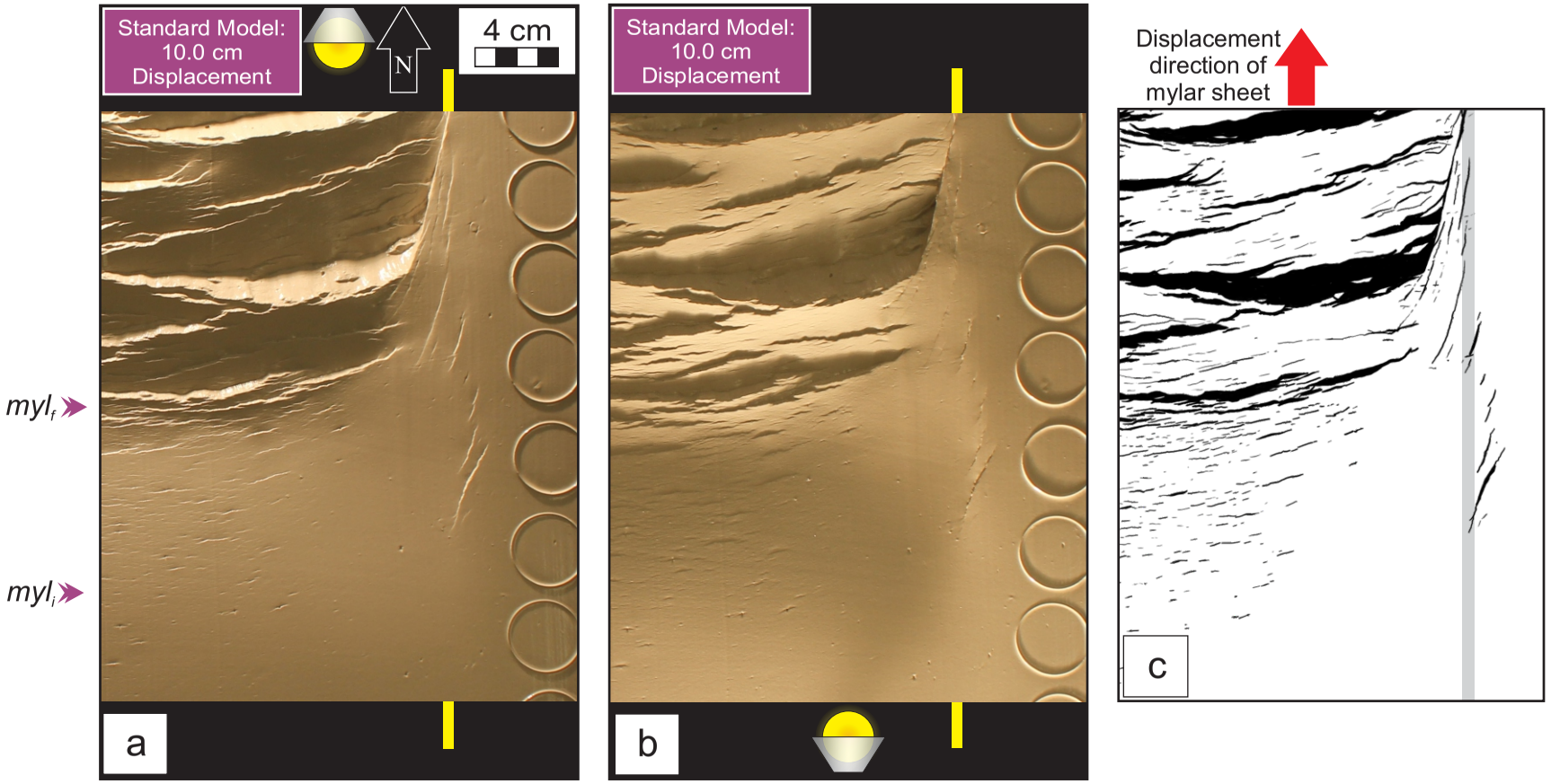

Fig. 2.8: Construction of fault-trace map utilizing multiple lighting directions (yellow bulbs) for Standard Model at 10 cm of boundary displacement. (a) Photo of part of Standard Model with light from north; north-dipping faults are bright; south-dipping faults are in shadow, with shadow width exceeding extent of fault surface. (b) Photo of part of Standard Model with light from south; south-dipping faults are bright. (c) Map of fault traces (black polygons) made by overlaying two photographs (a and b). For normal faults only, the width of the black polygon in the displacement direction (north) is equal to the heave on the fault. Yellow and gray bar(s) give location of the N-trending discontinuity. Purple arrows indicate initial and final positions of edge of mylar sheet (myl_i and myl_f respectively).

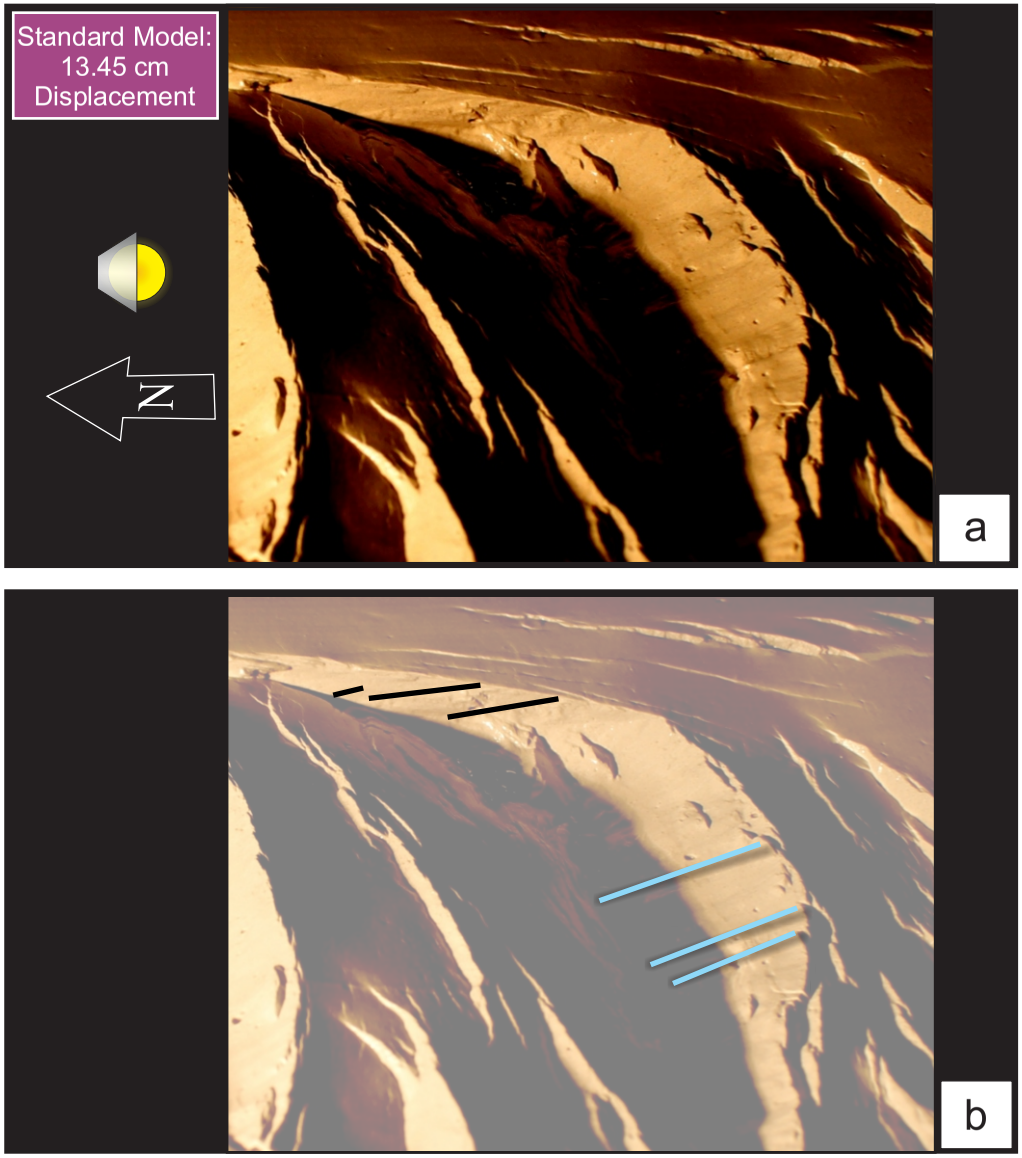

Fig. 2.9: Grooves on fault surfaces record slip direction. (a) Uninterpreted oblique view photo of Standard Model at 13.45 cm of boundary displacement. (b) Interpretation of fault-slip lineations. Shallow-raking grooves (black lines) record oblique slip on steeply-dipping NNE-striking faults. Grooves (blue lines) indicate mostly dip slip on E- and ENE-striking fault surfaces. These grooves have a vertical component, but the horizontal component of the groove vectors is (sub)parallel to the displacement direction (N).

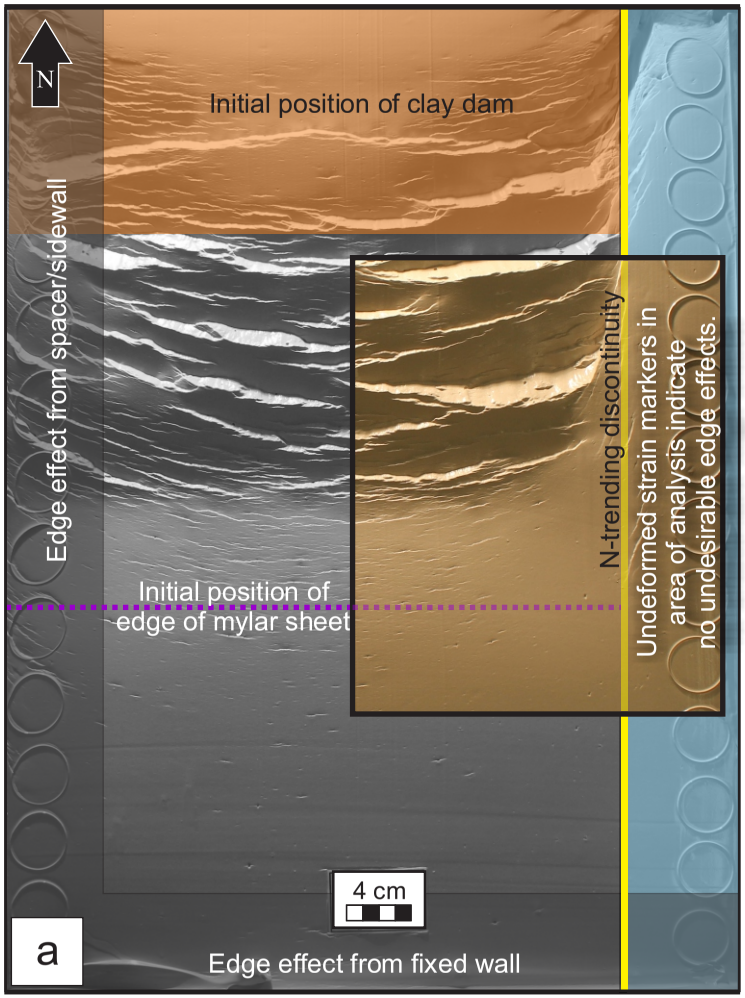

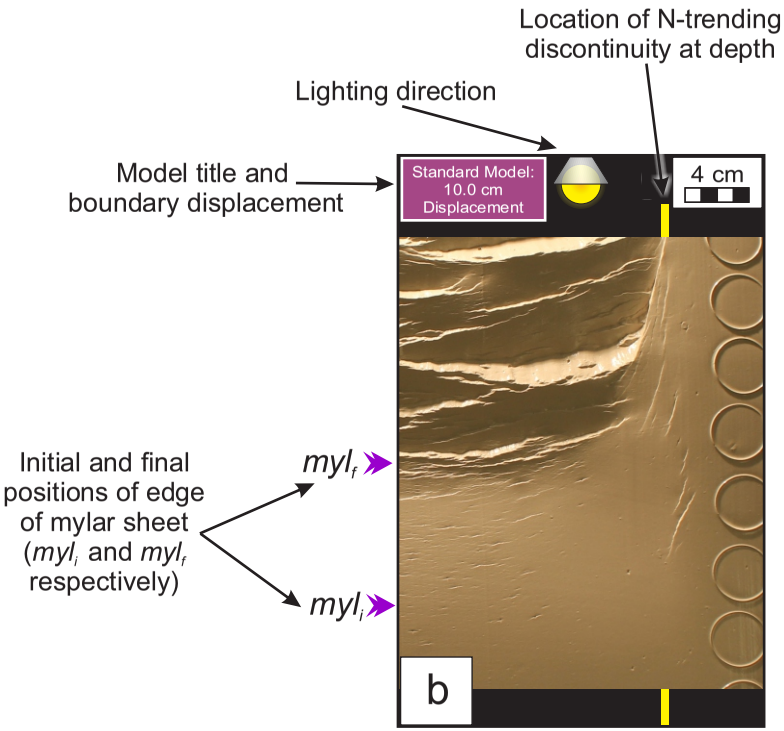

Fig. 2.10: Area of analysis for most models (except Variable-Putty Model and Layered Model). (a) Full view of Standard Model at 10.0 cm of boundary displacement with labeled positions of discontinuities. Thick black rectangle indicates area shown in (b). (b) Cropped view of (a) with explanation of symbols used in subsequent figures. Cropped area avoids undesired edge effects. See Appendix 7.2 for full-view photographs of models.

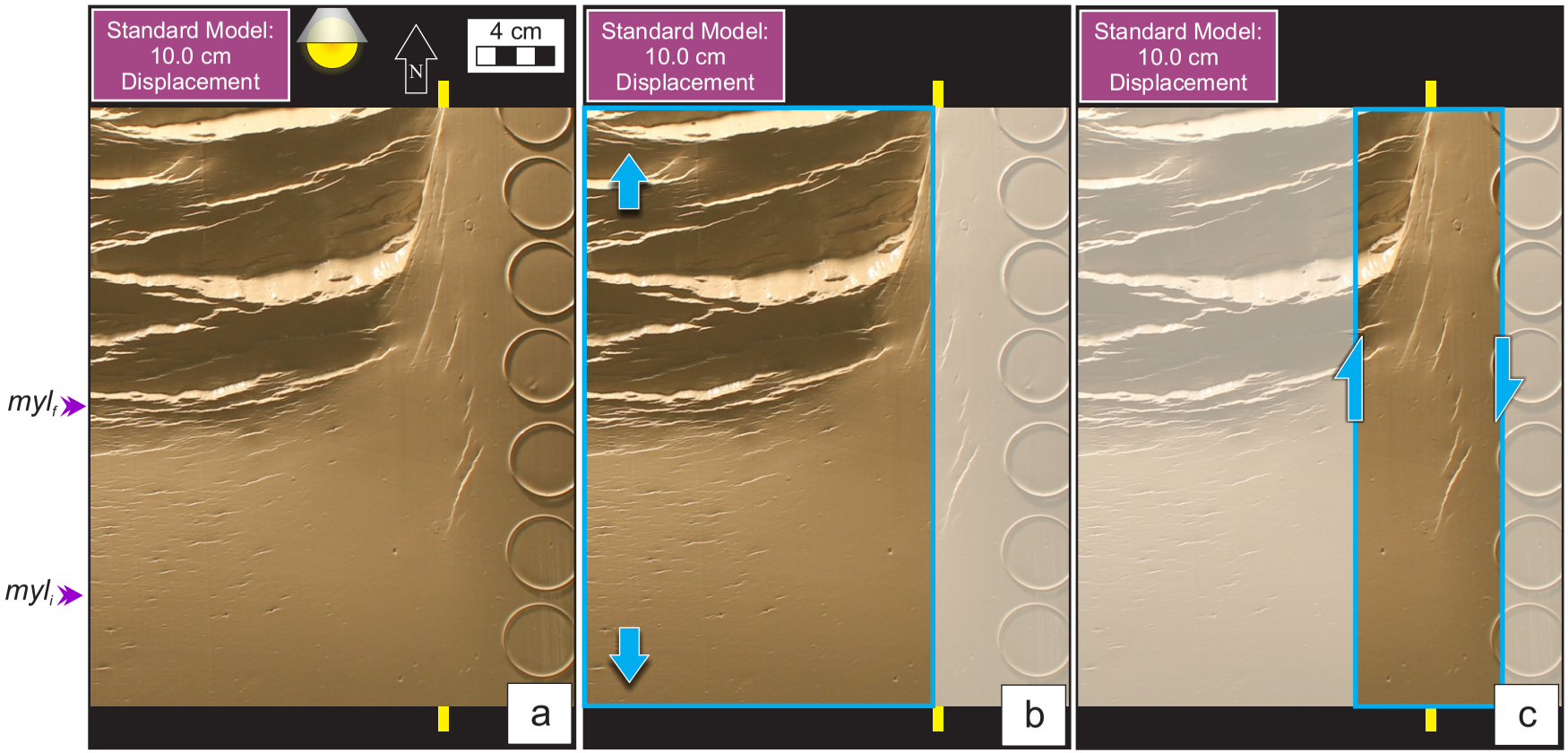

Fig. 3.1: Photographs showing two domains of deformation within Standard Model in plan view at 10.0 cm displacement. Yellow bars show approximate location of underlying N-trending discontinuity. Small purple arrows indicate initial and final positions of edge of mylar sheet (myl_i and myl_f respectively). (a) Standard Model without annotation. (b) Broad extensional domain with E-striking normal faults (indicated by blue box and N- and S-trending arrows) develops in clay above putty. (c) Broad right-lateral shear zone develops with NNE-striking oblique-slip faults above N-trending discontinuity (blue box and arrows show area and sense of shear).

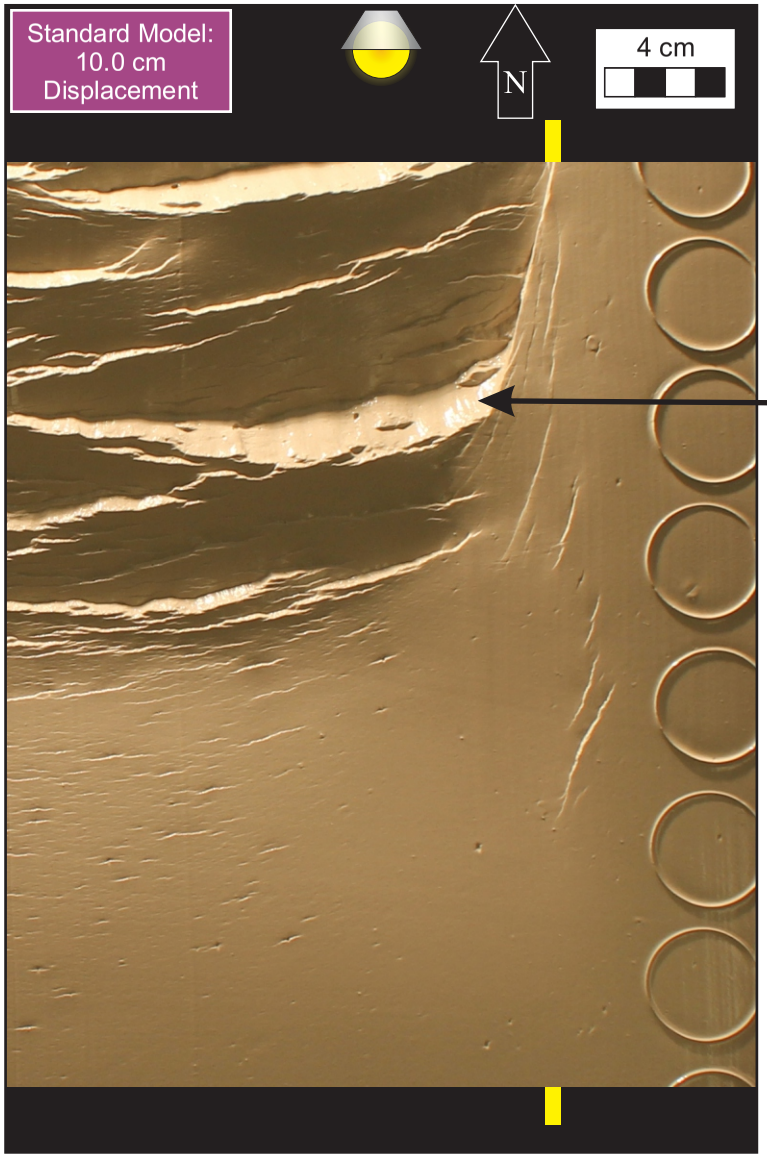

Fig. 3.2: Deformation at intersection of shear zone and extensional domain in Standard Model. E-striking normal faults in extensional domain link with NNE-striking oblique-slip faults in shear zone. Yellow bars show approximate location of underlying N-trending discontinuity. Faults have the greatest displacement near intersection of the extensional domain and the shear zone.

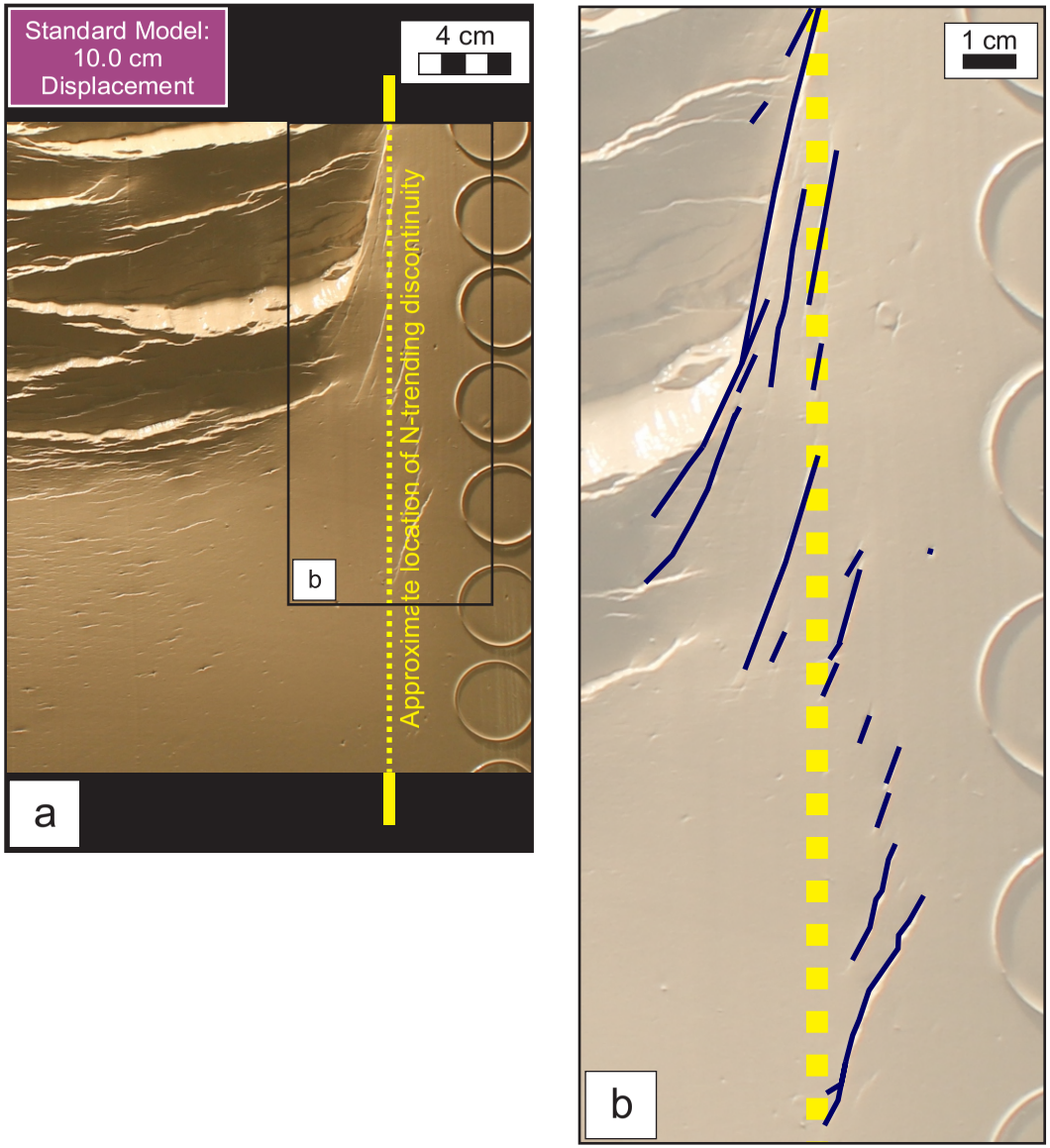

Fig. 3.3: Comparison of orientations of deep and shallow structures. (a) Yellow bars and dashed line show the approximate location of N-trending discontinuity. (b) Enlarged view showing NNE-striking faults above N-trending discontinuity.

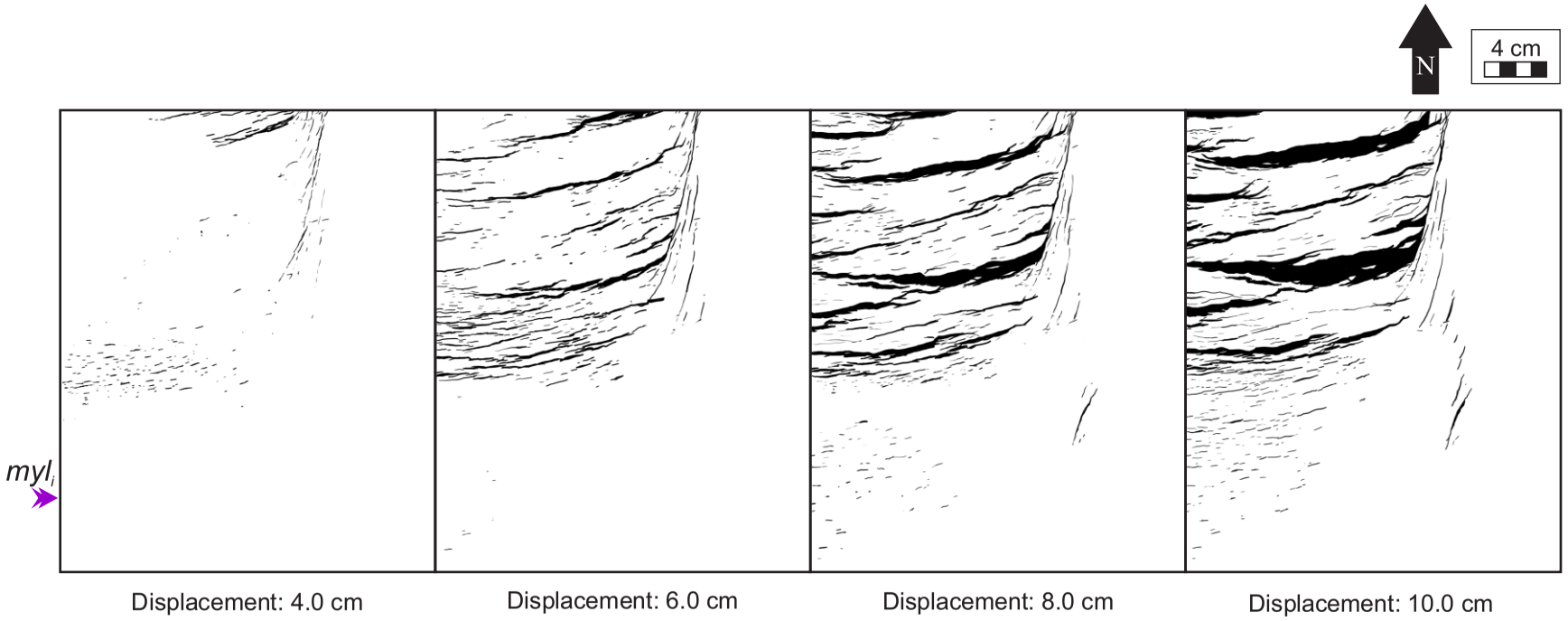

Fig. 3.4: Temporal development of Standard Model from 4.0 cm to 10.0 cm of displacement. Fault traces are black. The width of the polygons for normal faults represents the heave on the normal faults (i.e., the E-striking faults). Small purple arrow indicates initial position of edge of mylar sheet (myl_i).

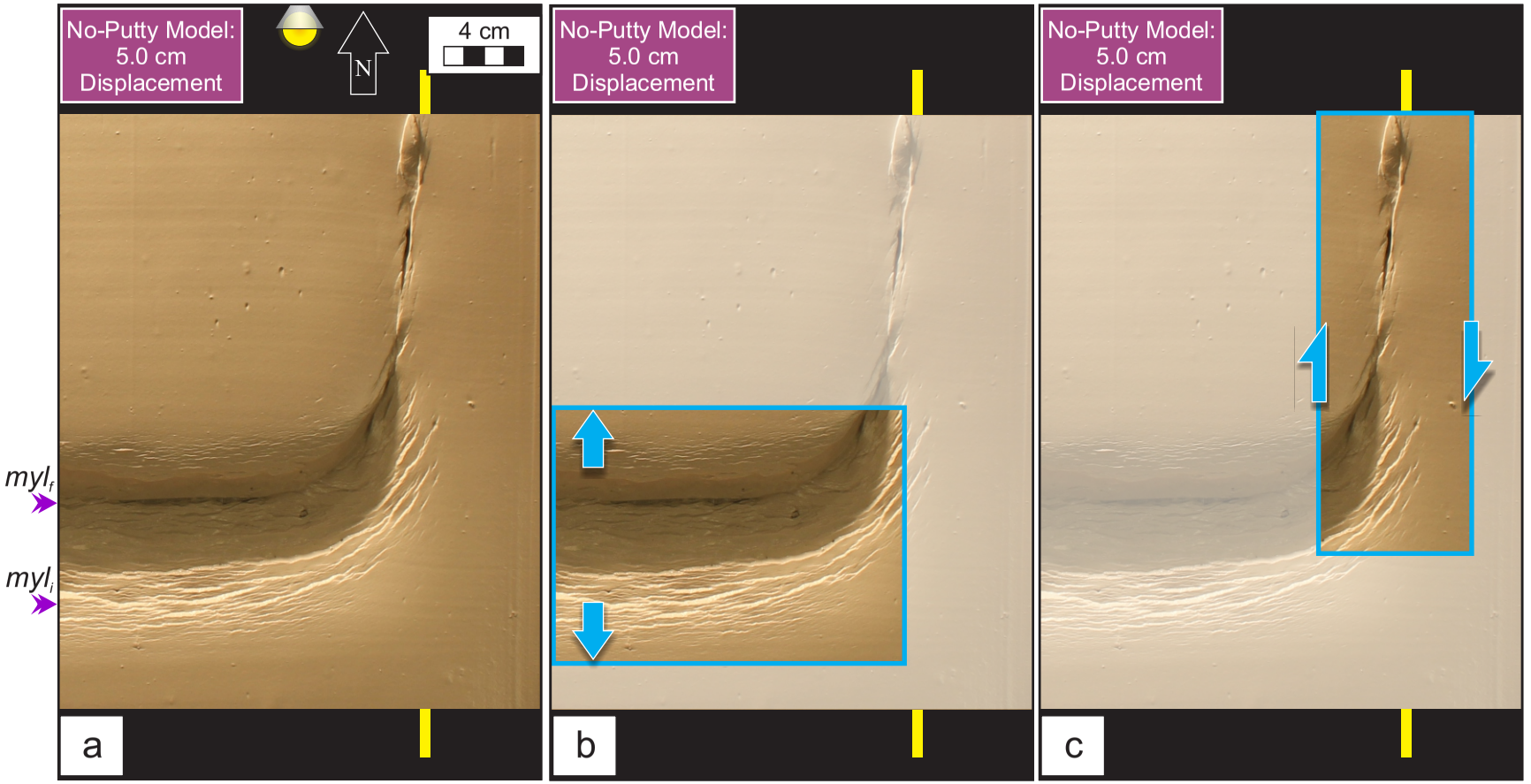

Fig. 3.5: Extensional domain and shear zone of No-Putty Model at 5.0 cm of displacement (see text in Methods section 2.3. for explanation of final-displacement magnitude). Yellow bars show approximate location of underlying N-trending discontinuity. Small purple arrows indicate initial and final positions of edge of mylar sheet (*myl*$_i$ and *myl*$_f$ respectively). (a) No-Putty Model without annotation. (b) No-Putty Model has a focused extensional domain above edge of mylar sheet. White-outlined blue arrows indicate extension direction. (c) No-Putty Model has a focused right-lateral shear zone above N-trending discontinuity. White-outlined blue arrows indicate sense of shear above N-trending discontinuity.

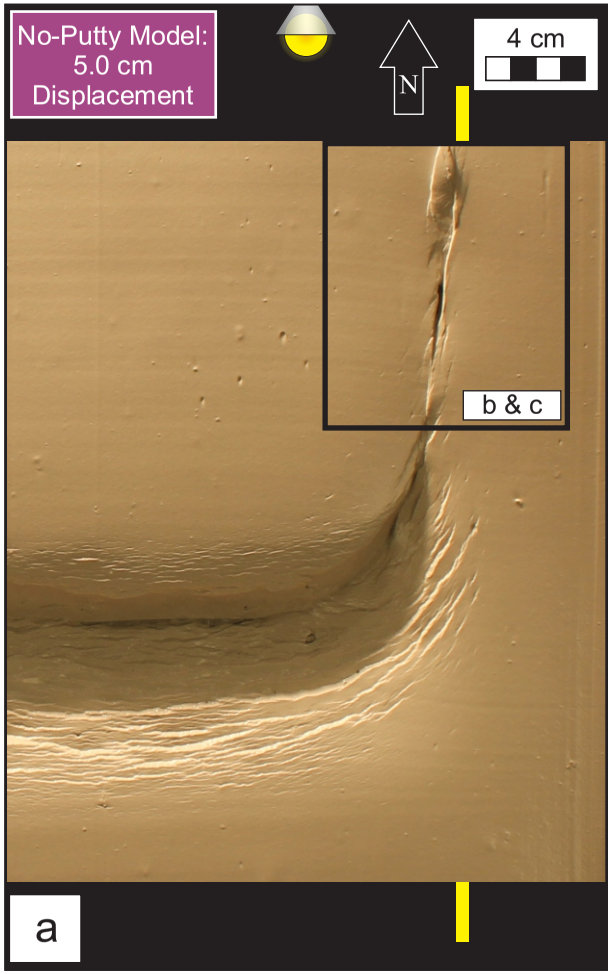

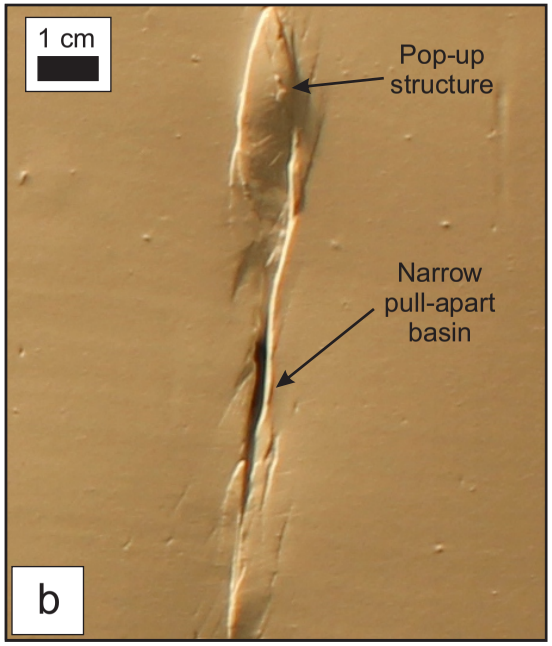

Fig. 3.6: Structural features within shear zone of No-Putty Model. (a) Location of Figs. 3.6b and 3.6c. (b) Enlargement of shear zone showing deformational features. Uplifted blocks of clay are likely pop-up structures that formed at restraining bends. Down-thrown blocks of clay are likely pull-apart basins that formed at releasing bends. (c) Interpretation of faults showing NNE-striking master fault and NE-striking faults that are likely R-type Riedel faults with right-lateral strike-slip.

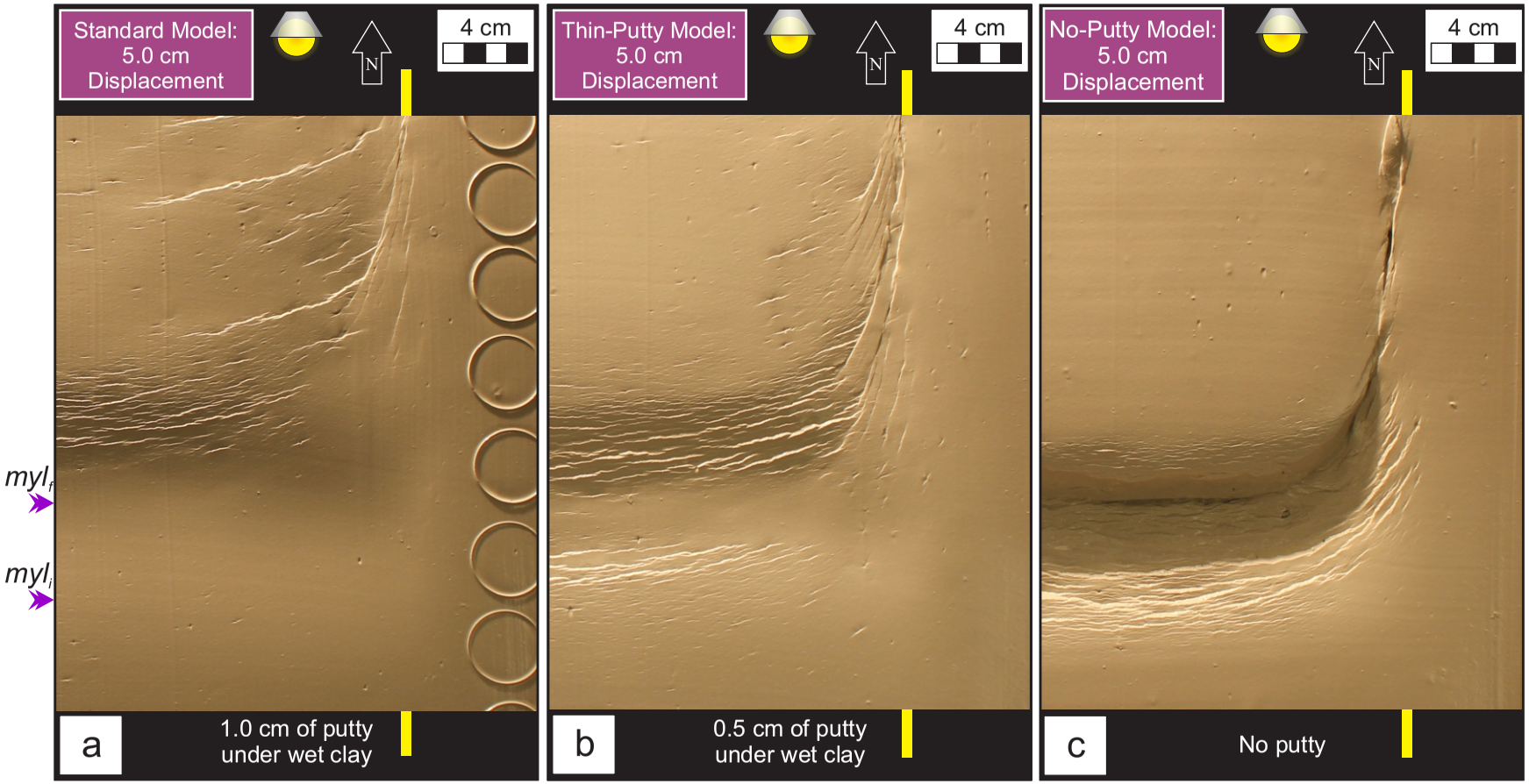

Fig. 3.7: Comparison of (a) Standard Model, (b) Thin-Putty Model, and (c) No-Putty Model at 5.0 cm displacement. Because the maximum boundary displacement on the No-Putty Model was 5.0 cm, this comparison also features the Standard Model and Thin-Putty Model with 5.0 cm boundary displacement. Yellow bars show approximate location of underlying N-trending discontinuity. Small purple arrows indicate initial and final positions of edge of mylar sheet (myl_i and myl_f respectively). With decreasing putty thickness, faulting is more focused above edge of mylar sheet in extensional domain and N-trending discontinuity in shear zone.

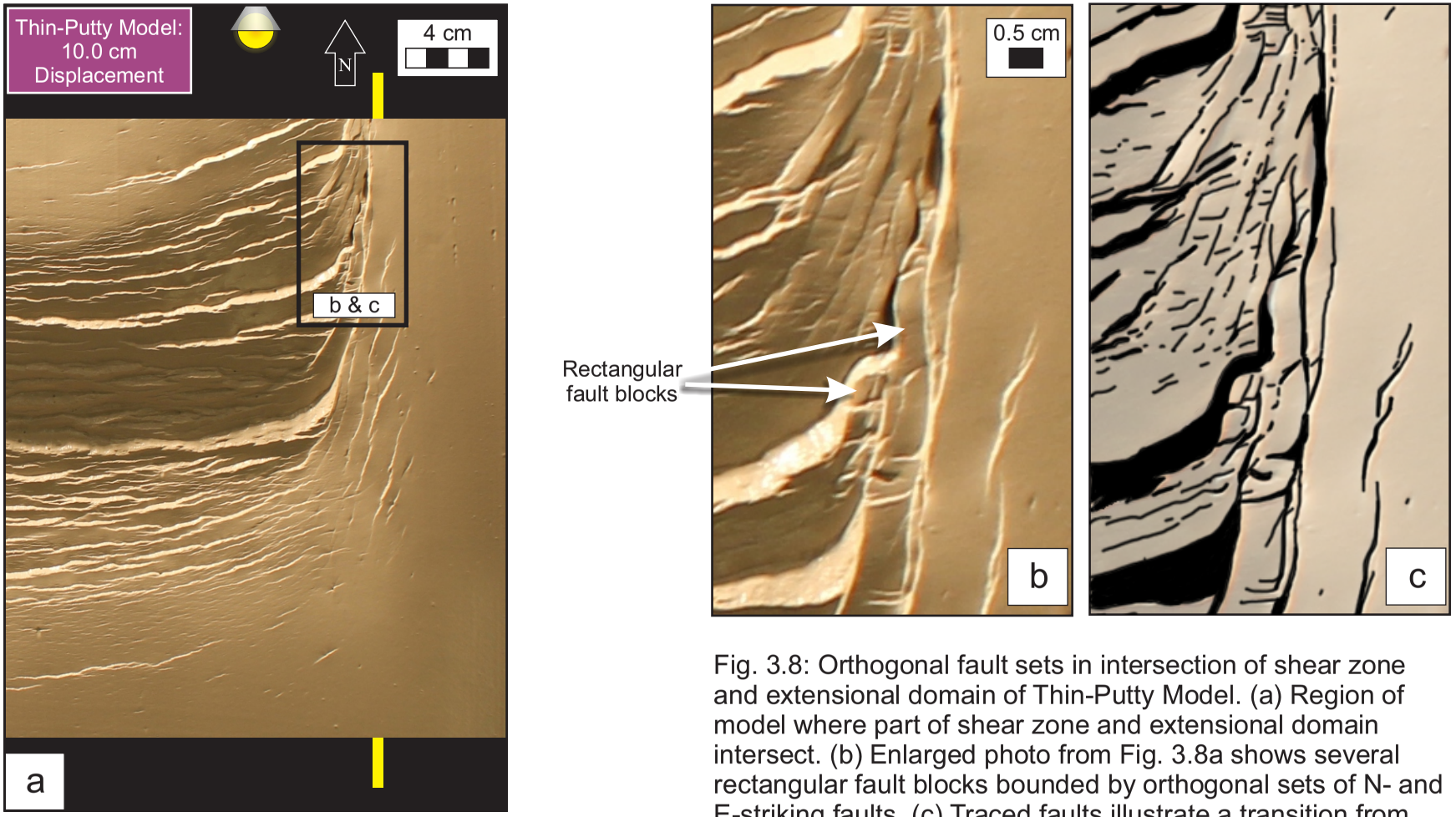

Fig. 3.8: Orthogonal fault sets in intersection of shear zone and extensional domain of Thin-Putty Model. (a) Region of model where part of shear zone and extensional domain intersect. (b) Enlarged photo from Fig. 3.8a shows several rectangular fault blocks bounded by orthogonal sets of N- and E-striking faults. (c) Traced faults illustrate a transition from NNE-striking faults in the shear zone (east) to ENE- and E-striking faults in the extensional domain (west).

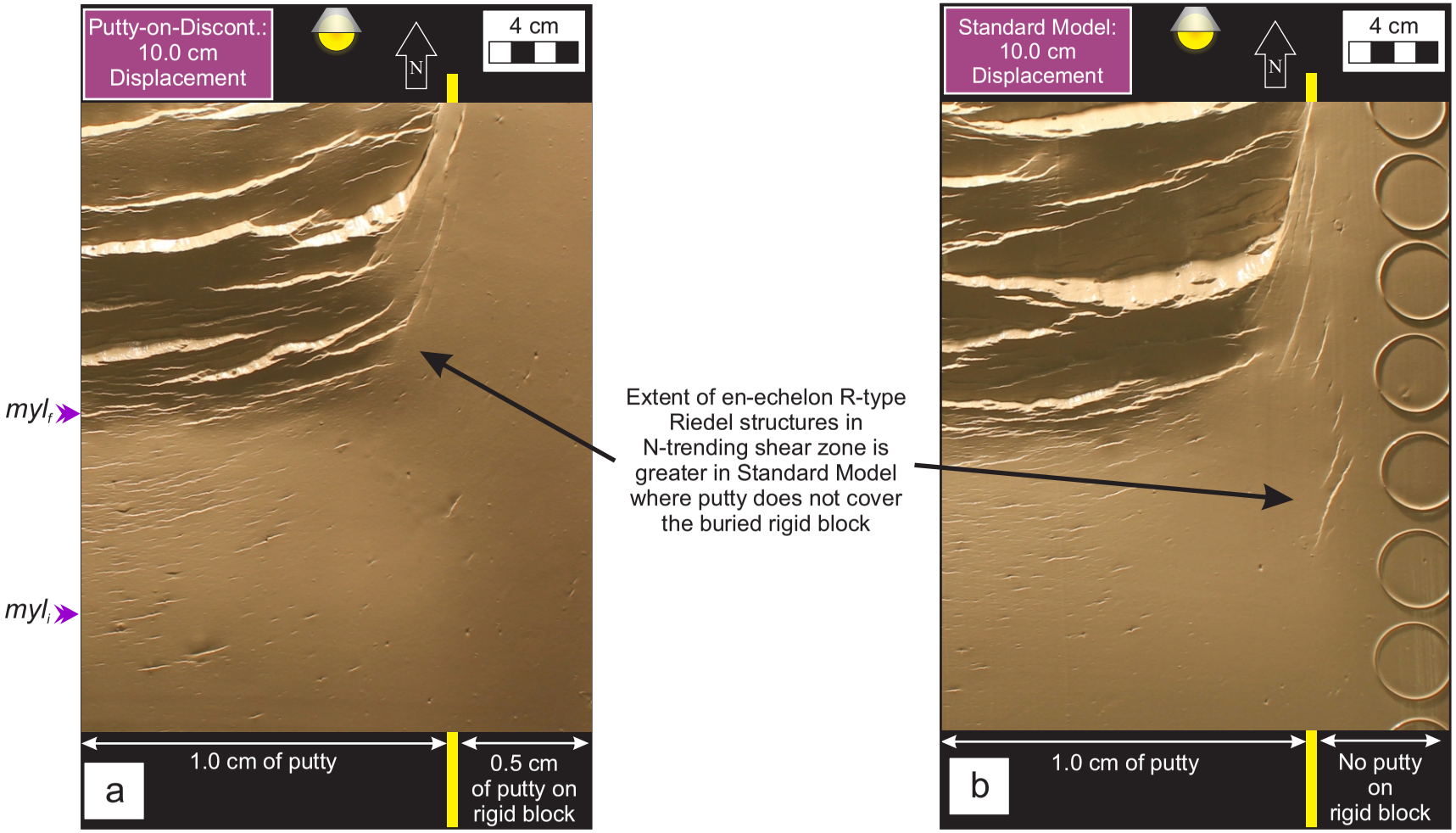

Fig. 3.9: Comparison of (a) Putty-on-Discontinuity Model and (b) Standard Model. Yellow bars show approximate location of underlying N-trending discontinuity. Small purple arrows indicate initial and final positions of edge of mylar sheet (*myl*$_i$ and *myl*$_f$ respectively). En-echelon R-type Riedel structures in the shear zone of (b) Standard Model extend farther south than in (a) Putty-on-Discontinuity Model.

Fig. 3.10 (next page): Plan view of Variable-Putty Model at 10 cm of displacement. Yellow bars show approximate location of both underlying N-trending discontinuities. Small purple arrows indicate initial and final positions of edge of mylar sheet (myl_i and myl_f respectively).

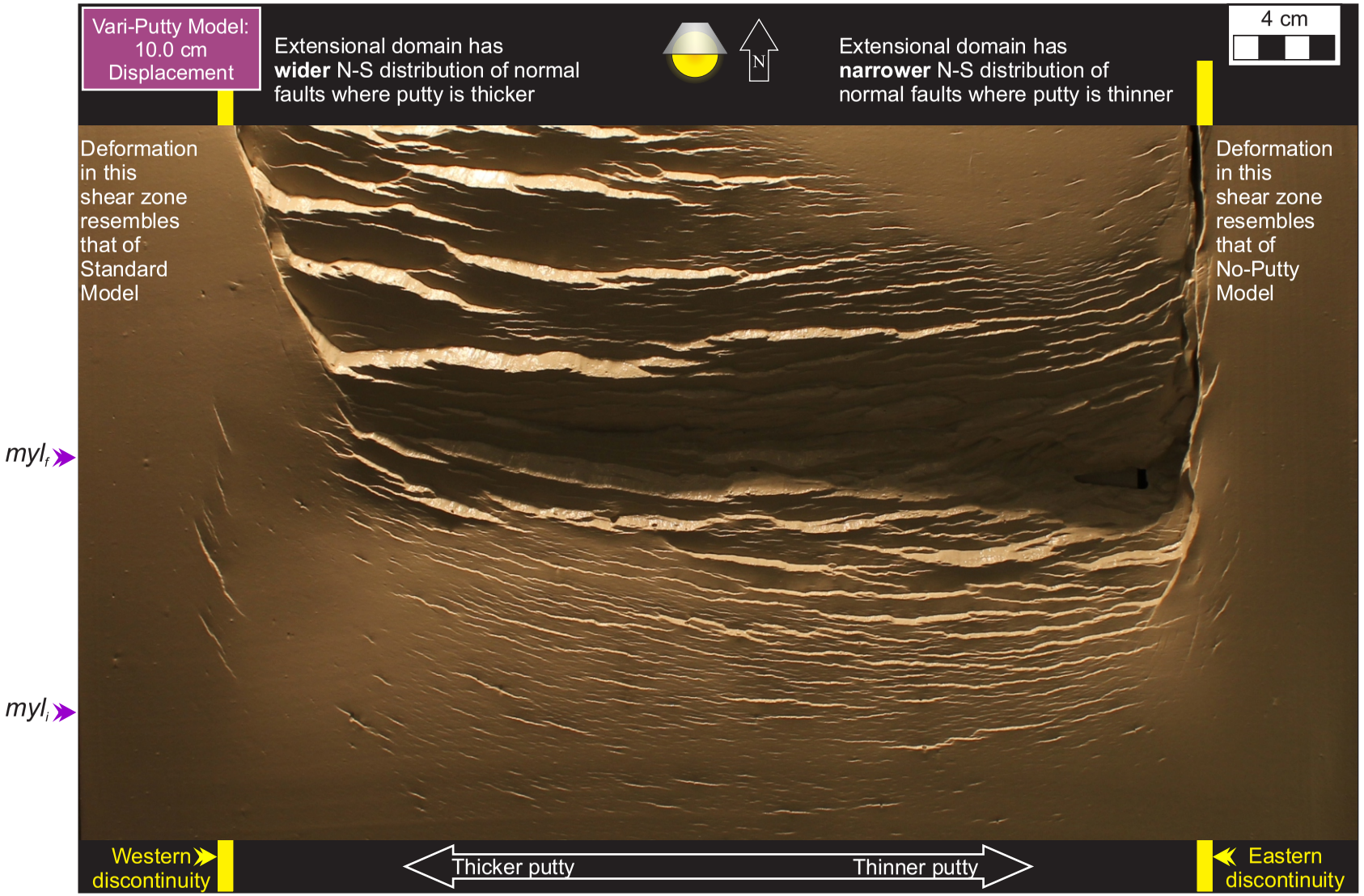

Fig. 3.10: Caption on previous page.

Fig. 3.11 (next page): Plan view of Layered Model at 10 cm of displacement. In both the western and eastern shear zones, deformation extends beyond the N-trending discontinuities and the area underlain by putty. Yellow bars show approximate location of both underlying N-trending discontinuities. Small purple arrows indicate initial and final positions of edge of mylar sheet (myl_i and myl_f respectively).

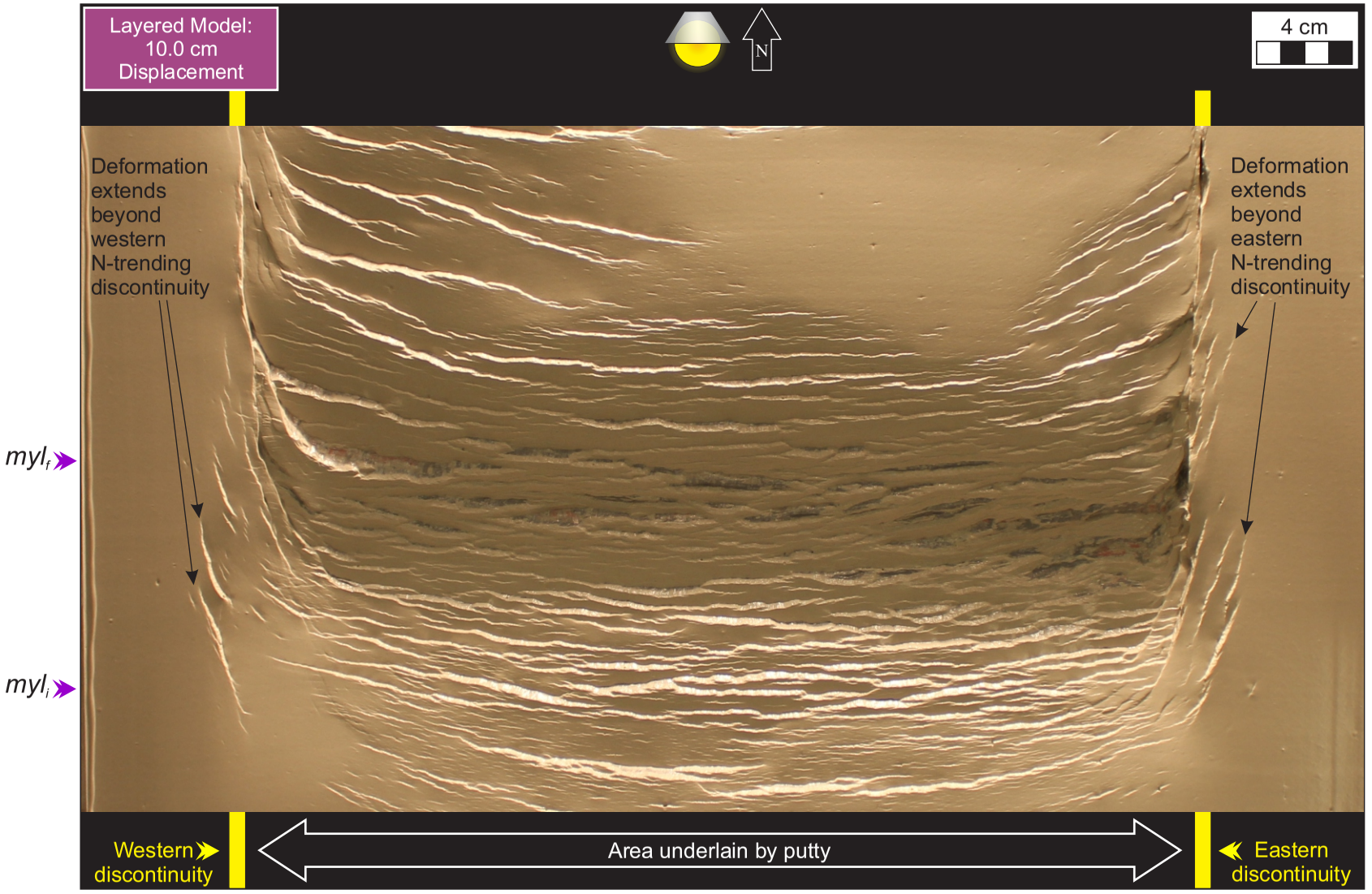

Fig. 3.11: Caption on previous page

Fig. 3.12 (next page): Plan view of base of Layered Model at 10 cm of displacement. Photograph of base is oriented so that the western and eastern discontinuities are located in the photo's west (left) and east (right), respectively. In both western and eastern shear zones, deformation does not extend beyond the area underlain by putty. No faults nucleate above the rigid blocks at clay-block contact; cracks in rigid-block impressions are from desiccation of clay. Yellow bars show approximate location rigid blocks at depth. The lateral extent of the yellow bars is based on the impressions in the clay. Small purple arrows indicate initial and final positions of edge of mylar sheet (myl_i and myl_f respectively). Lighting from south illuminates N-dipping fault surfaces, but basal view causes fault surfaces to appear S-dipping.

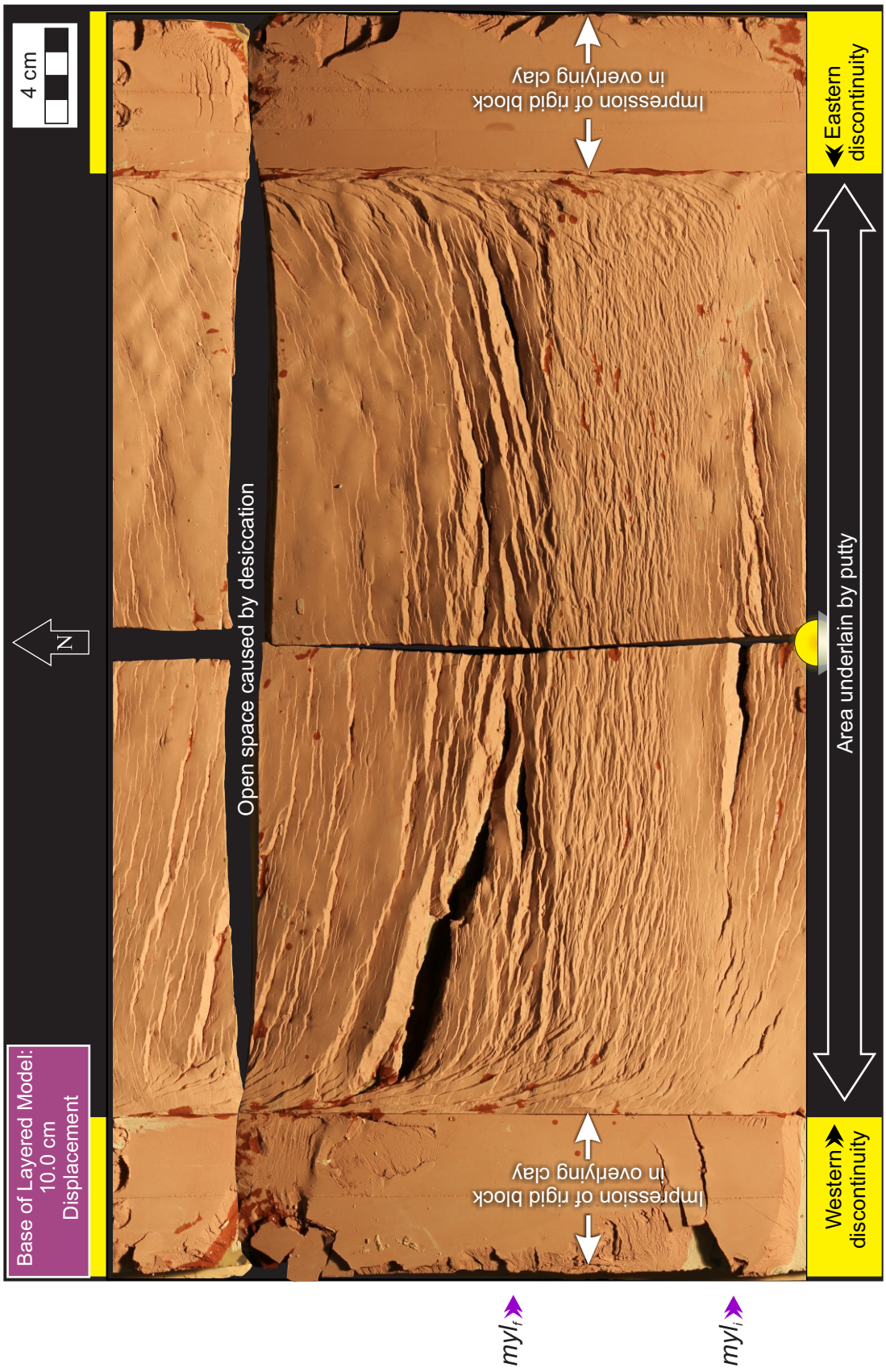

Fig. 3.12: Caption on previous page

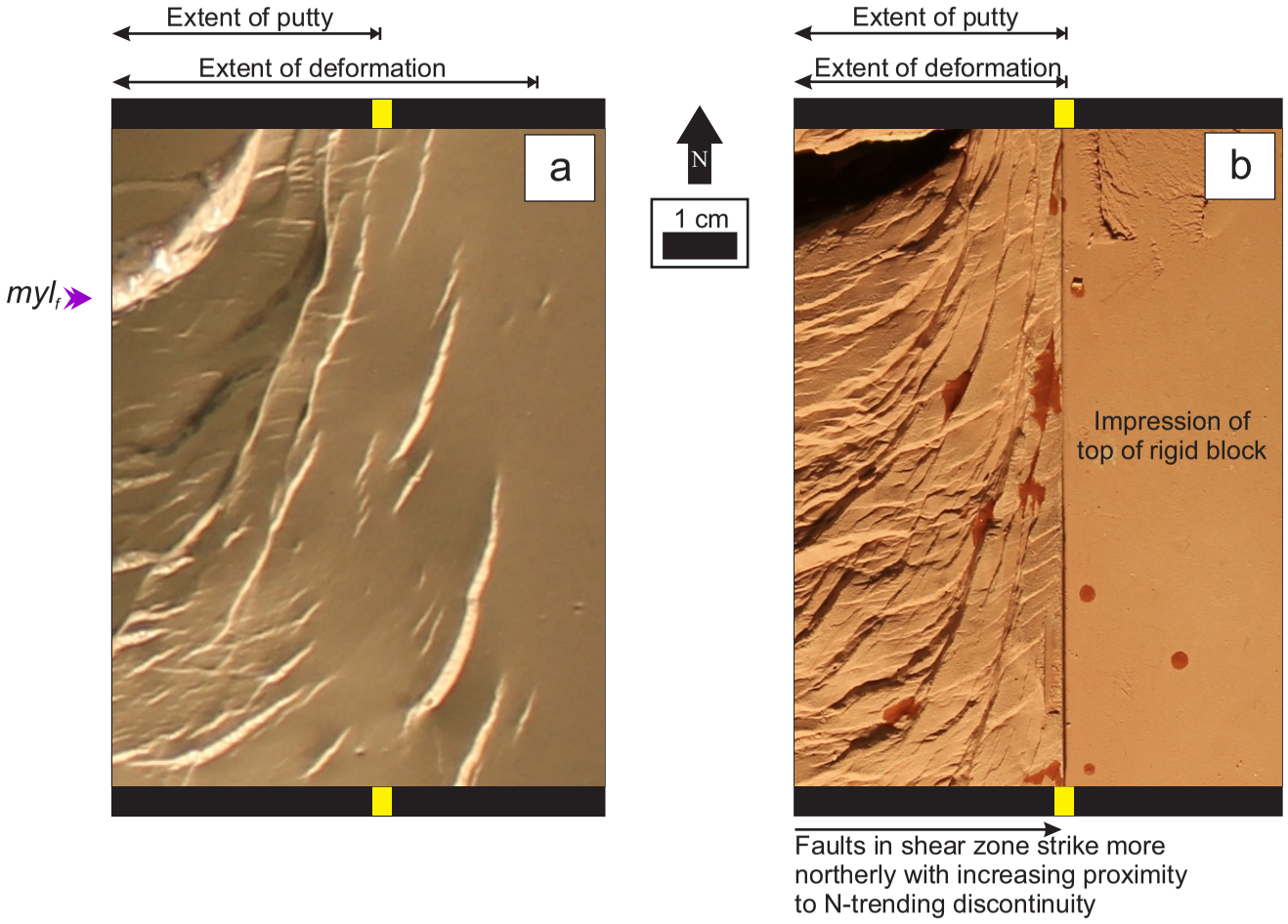

Fig. 3.13: Enlarged comparison of deformation at (a) top and (b) bottom of clay for western side of Layered Model. Photos are flipped (along N-S axis) to show fault orientations similar to other photos in Observations. Photos are aligned to approximate final position of edge of mylar sheet (*myl*$_f$). Yellow bars show approximate location of underlying N-trending discontinuity. “Wet” spots in Fig. 3b are residual pieces of putty.

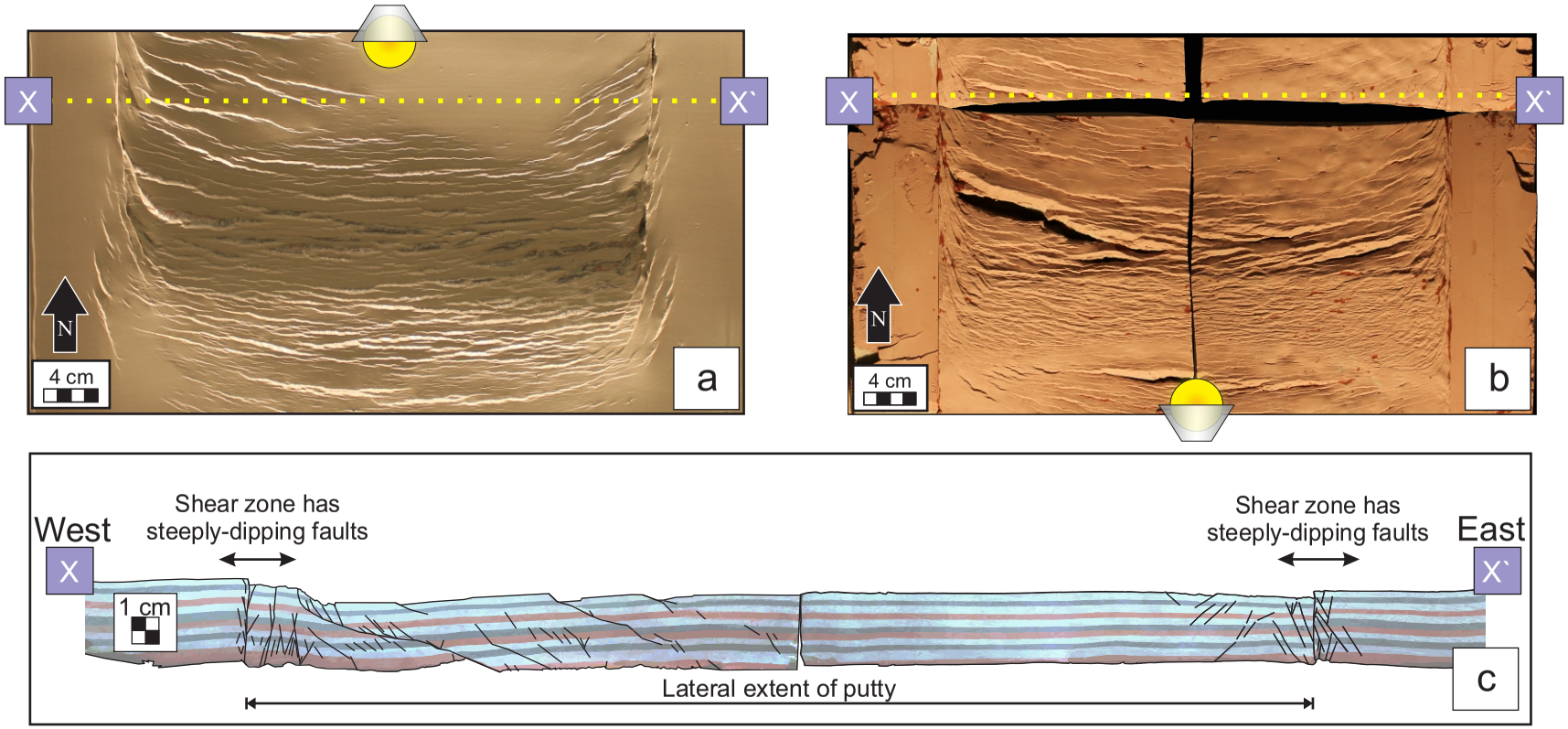

Fig. 3.14: Layered Model with West-East (X-X`) cross section. Faults in shear zone dip steeply. (a) Top of clay model. (b) Base of model at clay-putty contact. (c) Cross section of X-X`.

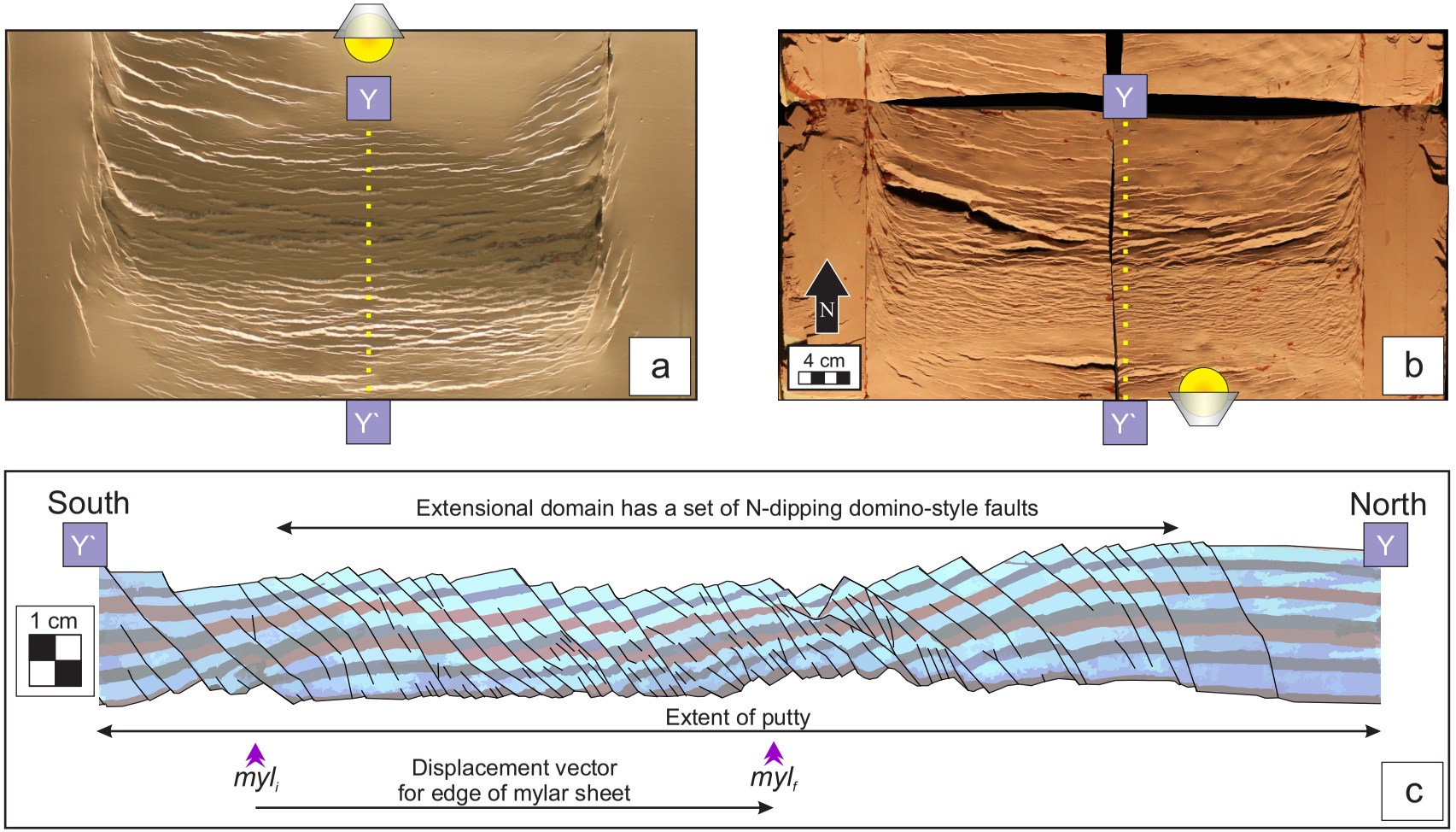

Fig. 3.15: Layered Model with North-South (Y-Y`) cross section. (a) Top of clay model. (b) Base of clay at clay-putty contact. (c) Y-Y` cross section. Small purple arrows indicate initial and final positions of edge of mylar sheet (myl_i and myl_f respectively).

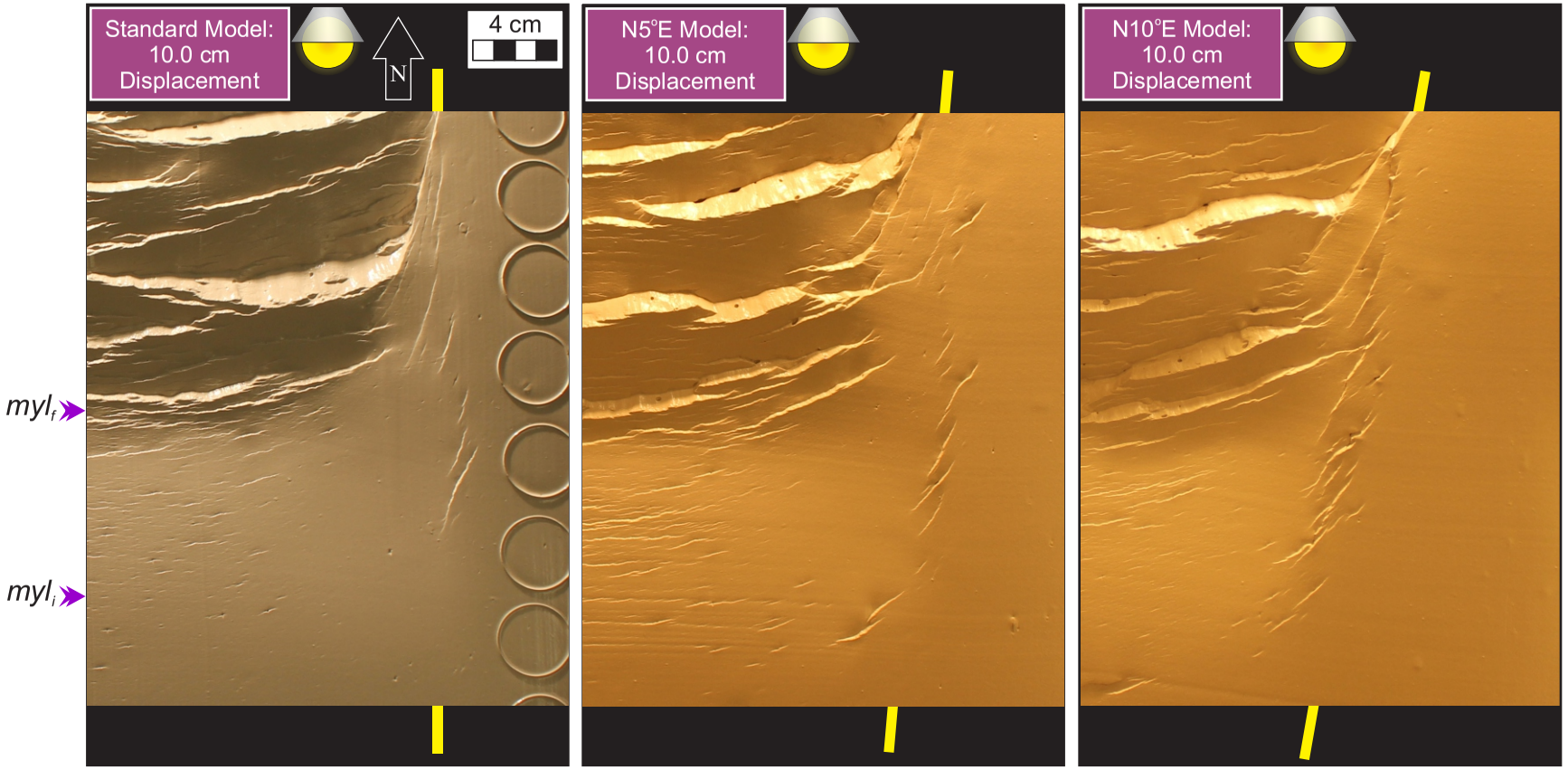

Fig. 3.16: Comparison of (from left to right) Standard Model, N5°E Model, and N10°E Model at 10.0 cm of displacement. Yellow bars show approximate location of underlying shear-dominated discontinuities. Small purple arrows indicate initial and final positions of edge of mylar sheet (myl_i and myl_f respectively). ENE-striking faults that link with NNE- and NE-striking faults have greater displacement than faults that do not link at intersection of extensional domain and shear zone.

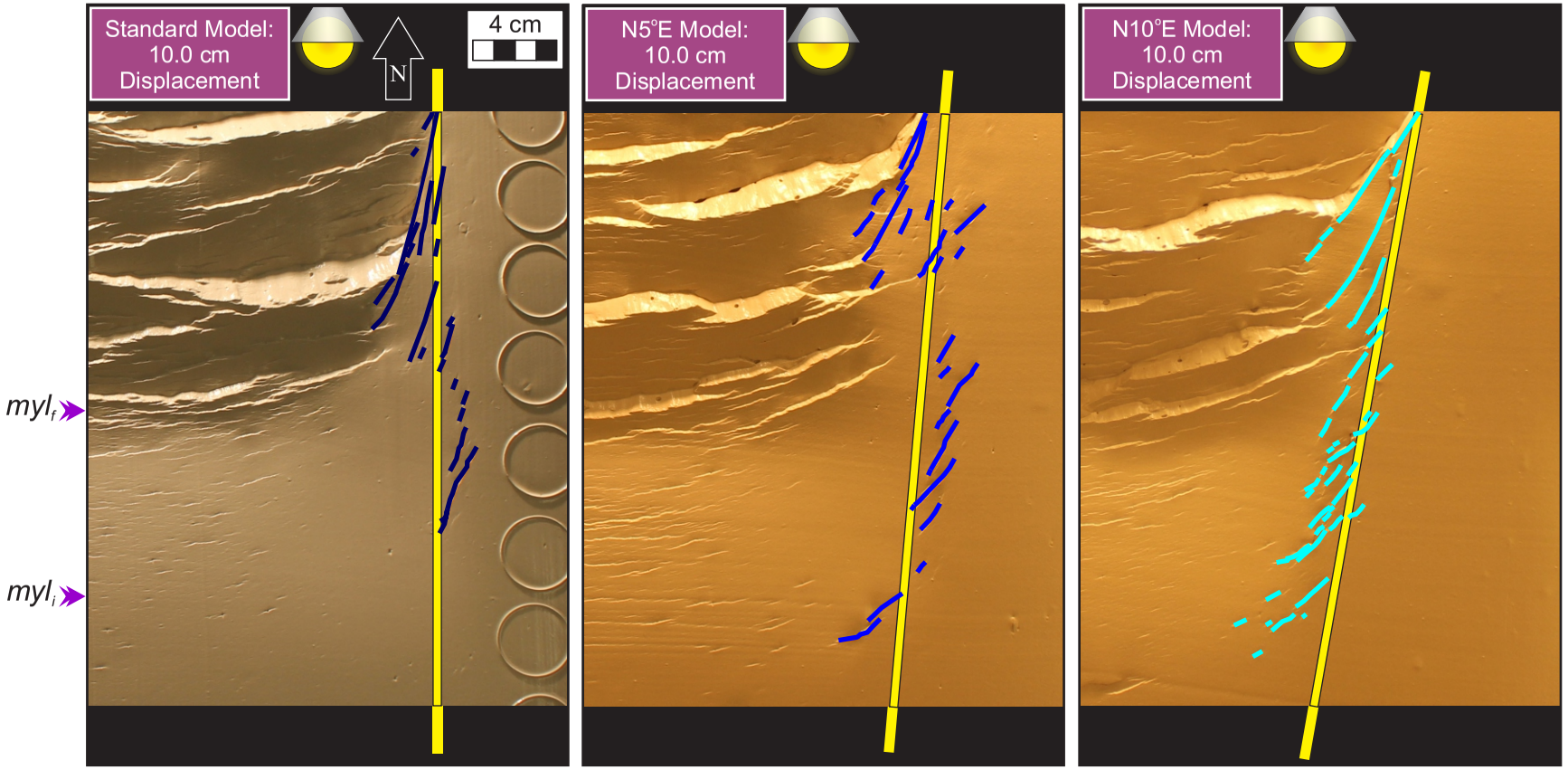

Fig. 3.17: Fault traces in shear zone for (from left to right) Standard Model, N5°E Model, and N10°E Model. Fault-trace lines have a variation of blue for each model. Yellow bars show approximate location of underlying shear-dominated discontinuities. Small purple arrows indicate initial and final positions of edge of mylar sheet (myl_i and myl_f respectively). Uninterpreted photos are in Fig. 3.16.

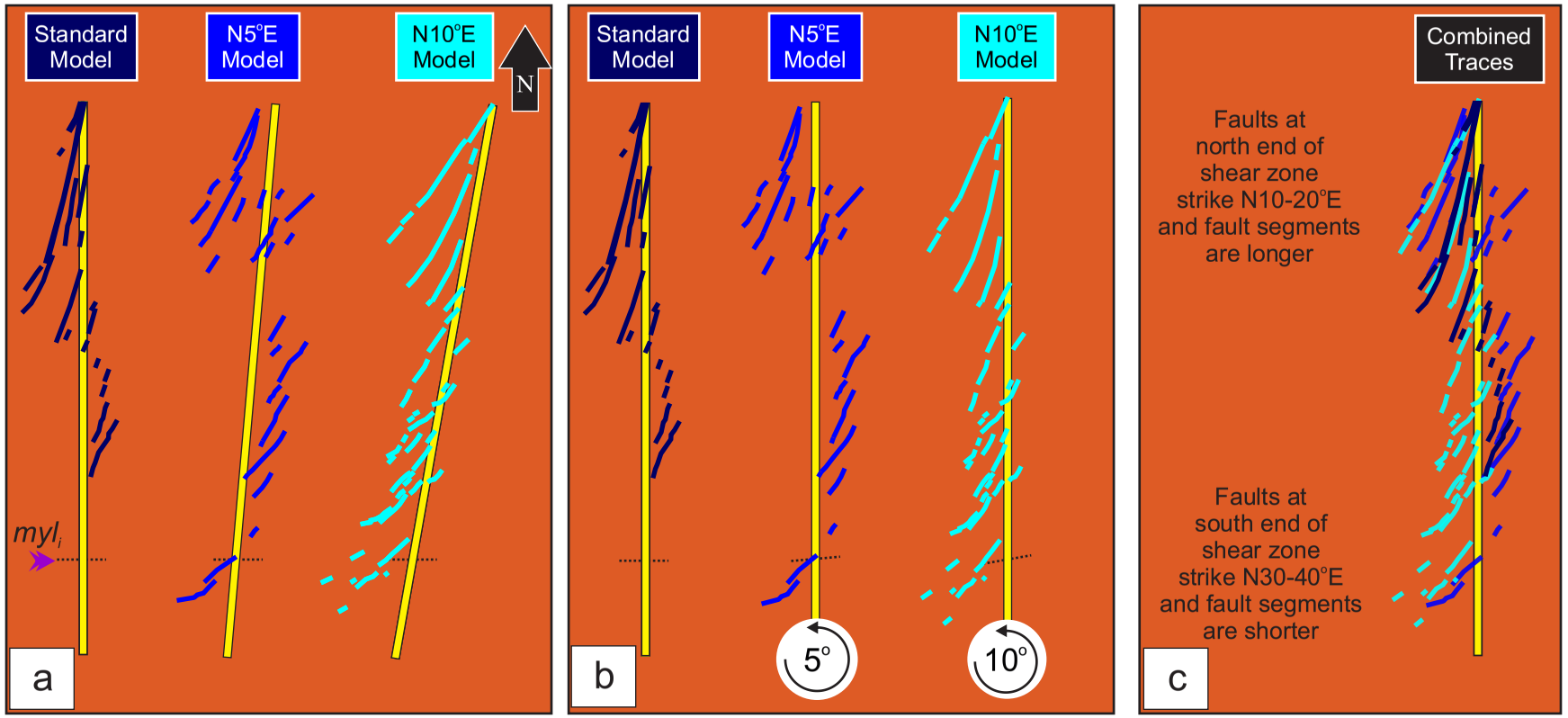

Fig. 3.18: Comparison of fault traces (variations of blue) in shear zone above shear-dominated discontinuities (yellow). Traces made from Fig. 3.16. (a) Side-by-side comparisons of models with underlying shear-dominated discontinuities in their true orientations. Initial position of the edge of mylar sheet (dashed line) trends E for each model. (b) Side-by-side comparison with all shear-dominated discontinuities rotated to trend N. Traces are aligned with respect to intersection of the initial position of the edge of mylar sheet with buried rigid block. (c) Fault traces and shear-dominated discontinuities superimposed to compare fault orientations and fault lengths.

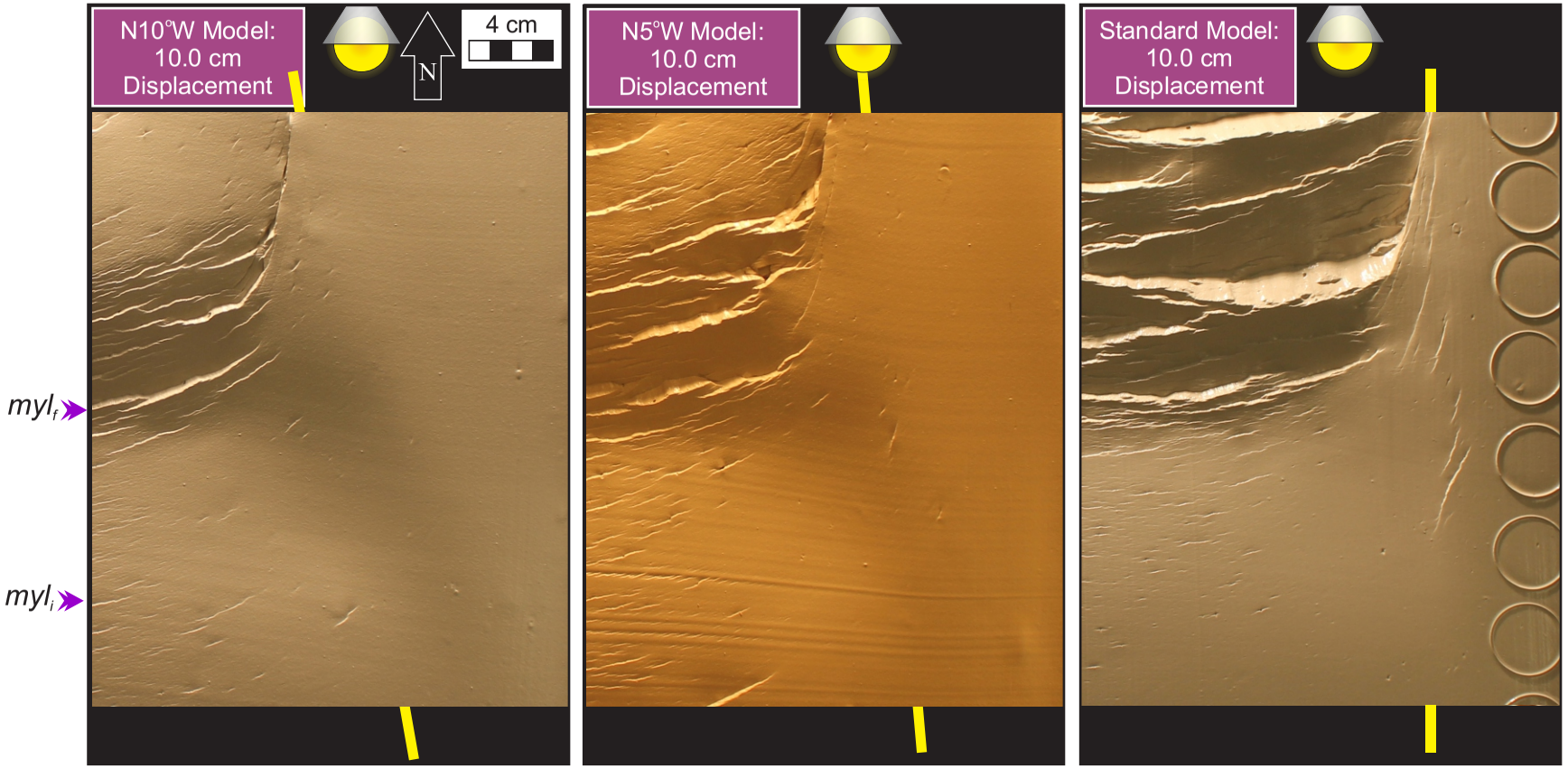

Fig. 3.19: Comparison of extensional domains and shear zones of (from left to right) N10°W Model, N5°W Model, and Standard Model at 10.0 cm of displacement. Yellow bars show approximate location of underlying shear-dominated discontinuities. Small purple arrows indicate initial and final positions of edge of mylar sheet (myl_i and myl_f respectively).

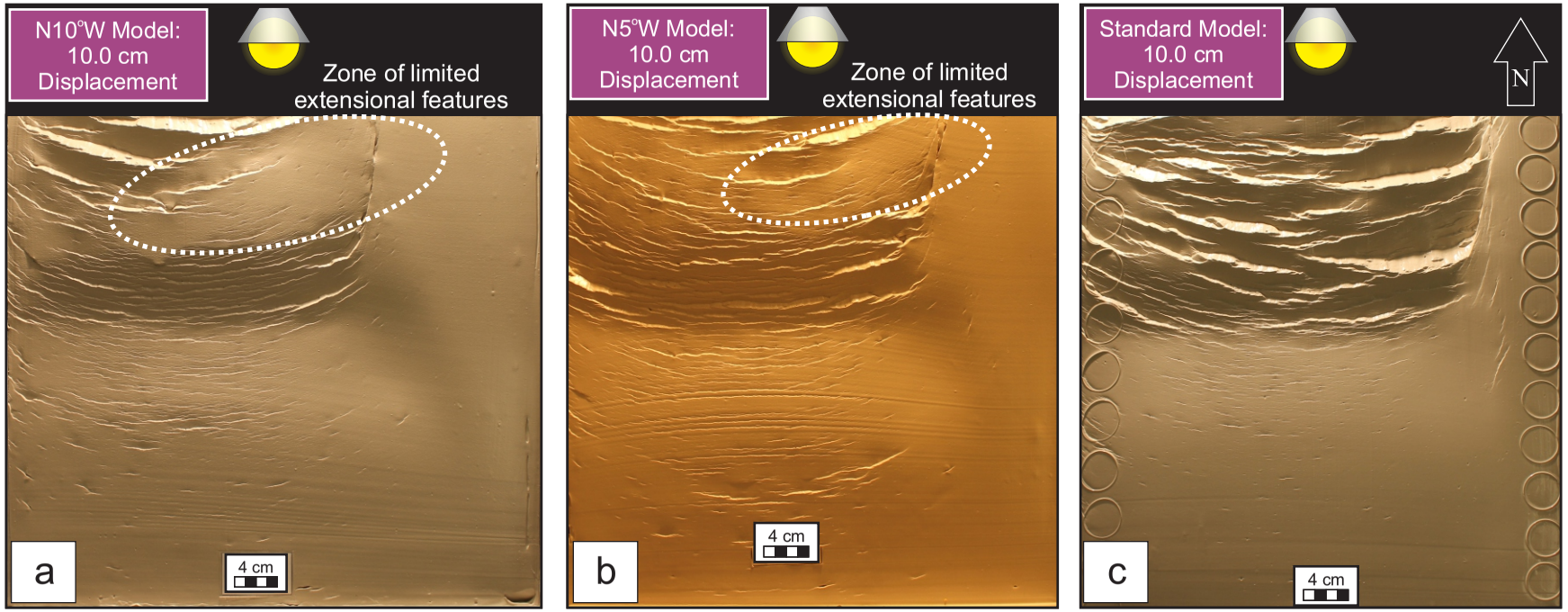

Fig. 3.20: Zones of limited extensional features. Photos are cropped at E and W edges of models to display full extent of these zones. Comparison of the (a) N10°W Model, (b) N5°W Model, and (c) Standard Model at 10.0 cm of displacement.

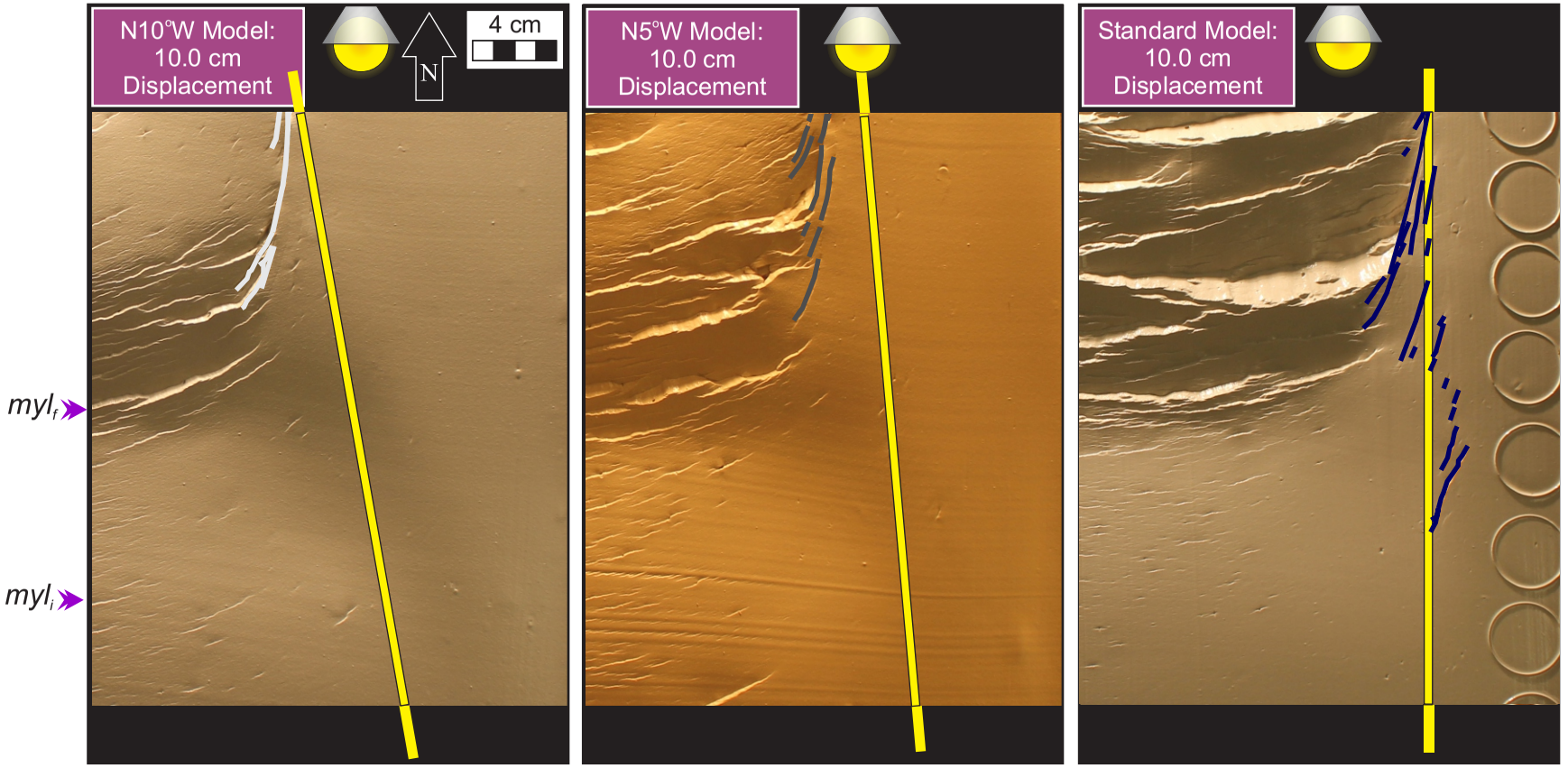

Fig. 3.21: Fault traces in shear zones of (from left to right) N10°W Model, N5°W Model, and Standard Model at 10.0 cm of displacement. Fault-trace lines have a variation of gray for each model. Yellow bars show approximate location of underlying shear-dominated discontinuities. Small purple arrows indicate initial and final positions of edge of mylar sheet (myl_i and myl_f respectively). Uninterpreted photos are in Fig. 3.19.

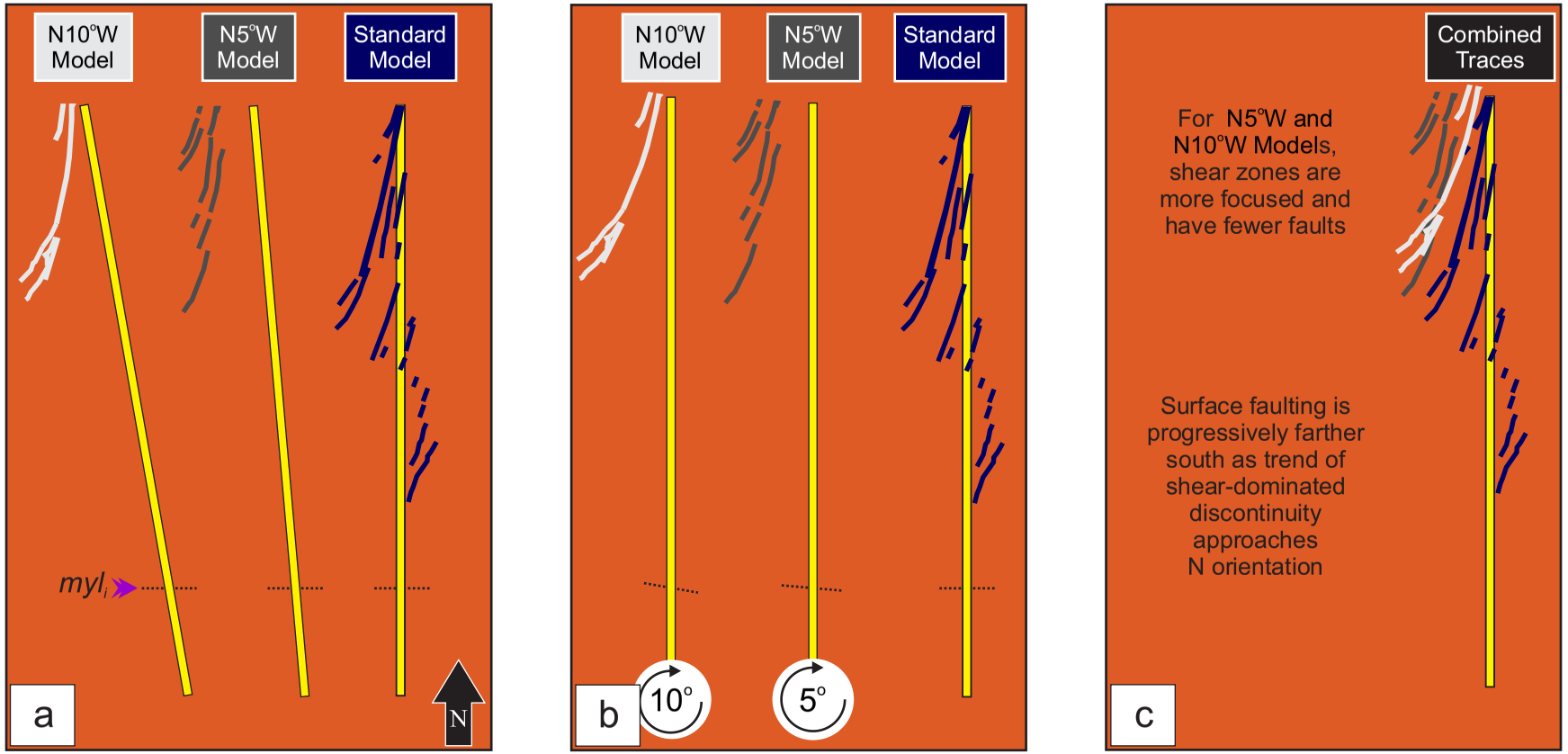

Fig. 3.22: Comparison of fault traces in shear zone above shear-dominated discontinuities (yellow). Traces made from Fig. 3.19. (a) Side-by-side comparisons of models with underlying shear-dominated discontinuities in their true orientations. Inital position of the edge of mylar sheet (dashed line) trends E for each model. (b) Side-by-side comparison with all shear-dominated discontinuities rotated to trend N. Traces are aligned with respect to intersection of the initial position of the edge of mylar sheet with buried rigid block. (c) Fault traces and shear-dominated discontinuities superimposed to compare fault orientations and fault lengths.

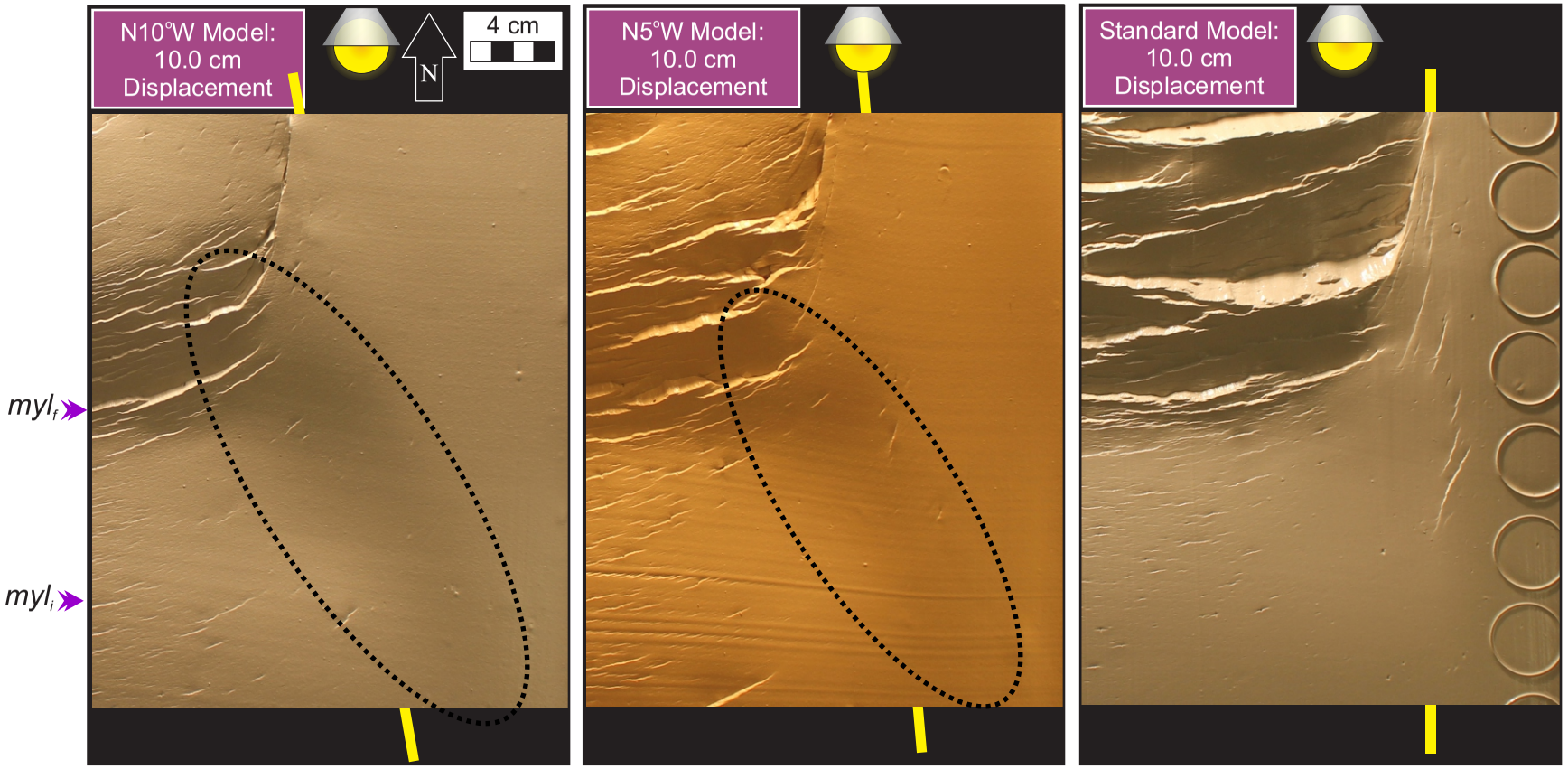

Fig. 3.23: NW-trending depressions (dashed ellipses) in (from left to right) N10°W Model and N5°W Model at 10.0 cm of displacement. Yellow bars show approximate location of underlying shear-dominated discontinuities. Small purple arrows indicate initial and final positions of edge of mylar sheet (myl_i and myl_f respectively). NW-trending depressions occur along the underlying shear-dominated discontinuity between the initial and final location of the mylar sheet. Standard Model (left) lacks such a NW-trending depression in comparison.

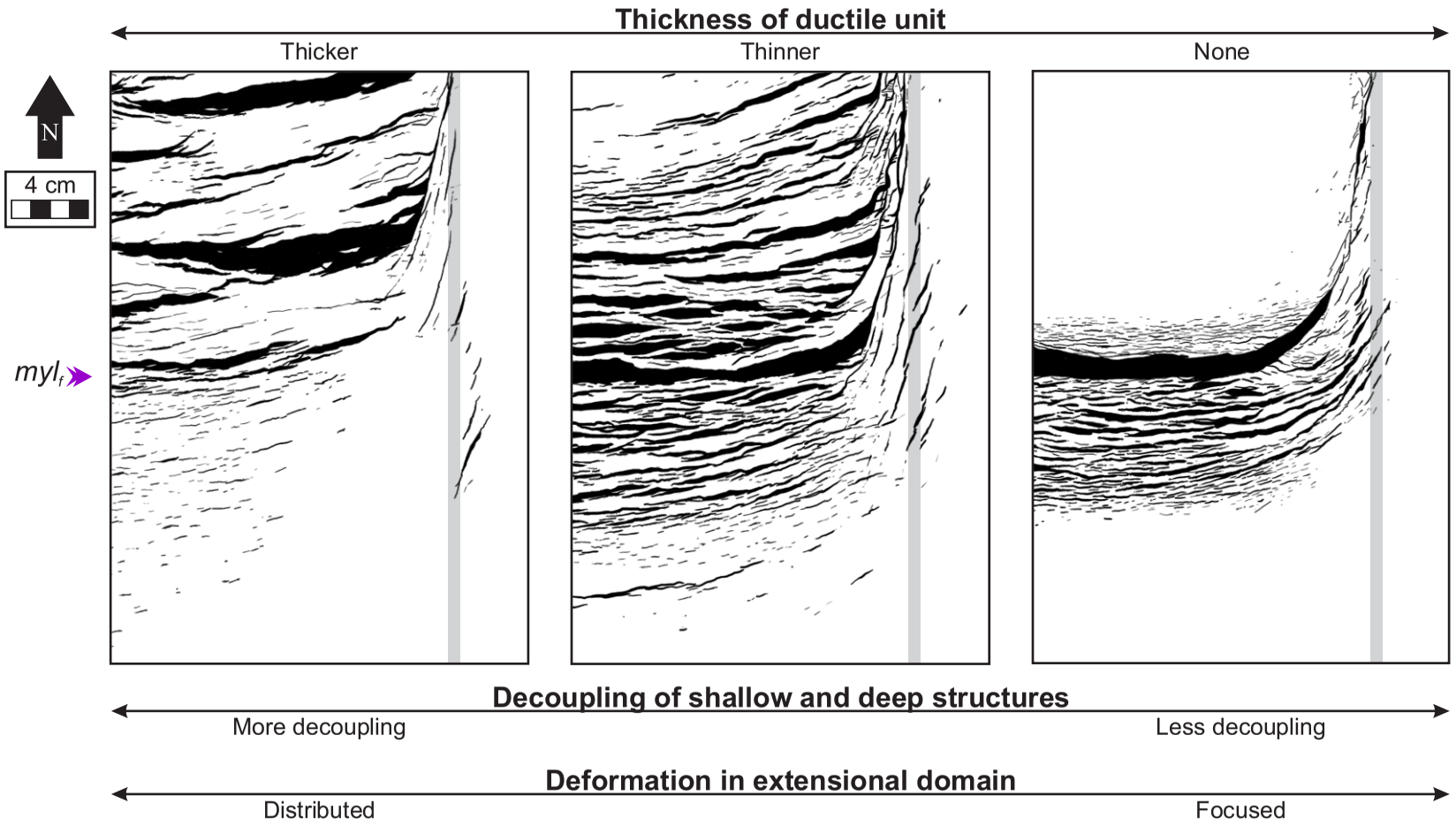

Fig. 4.1: Effect of putty thickness on fault patterns at top of clay for (from left to right) Standard Model at 10.0 cm of displacement, Thin-Putty Model at 10.0 cm of displacement, and No-Putty Model at 5.0 cm displacement (see Methods section 2.3 for explanation of this maximum displacement magnitude). Illustrations are aligned to final position of edge of mylar sheet (*myl*$_f$). Gray bars show approximate location of underlying N-trending discontinuity.

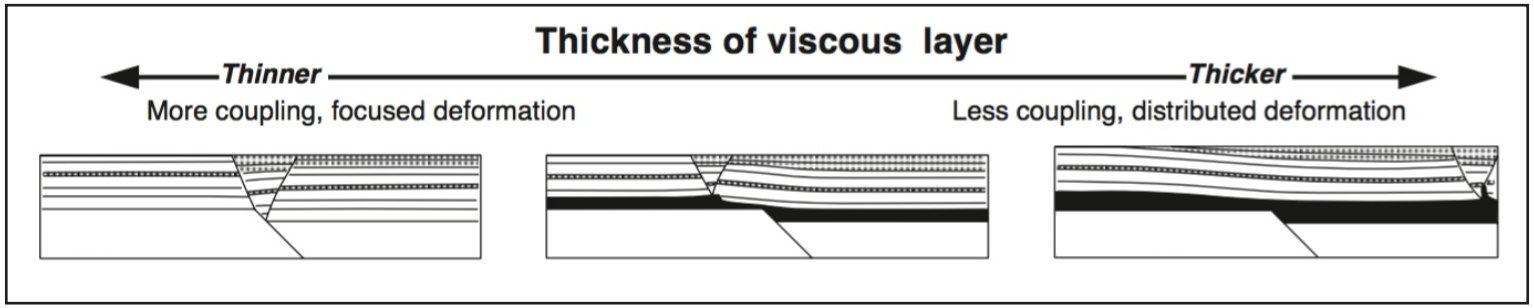

Fig. 4.2: Relationship of thickness of ductile (viscous) layer (shown in black) to coupling and distribution of deformation in experimental models of Withjack and Callaway (2000). Cross sections show deformation patterns above an upward-propagating normal fault.

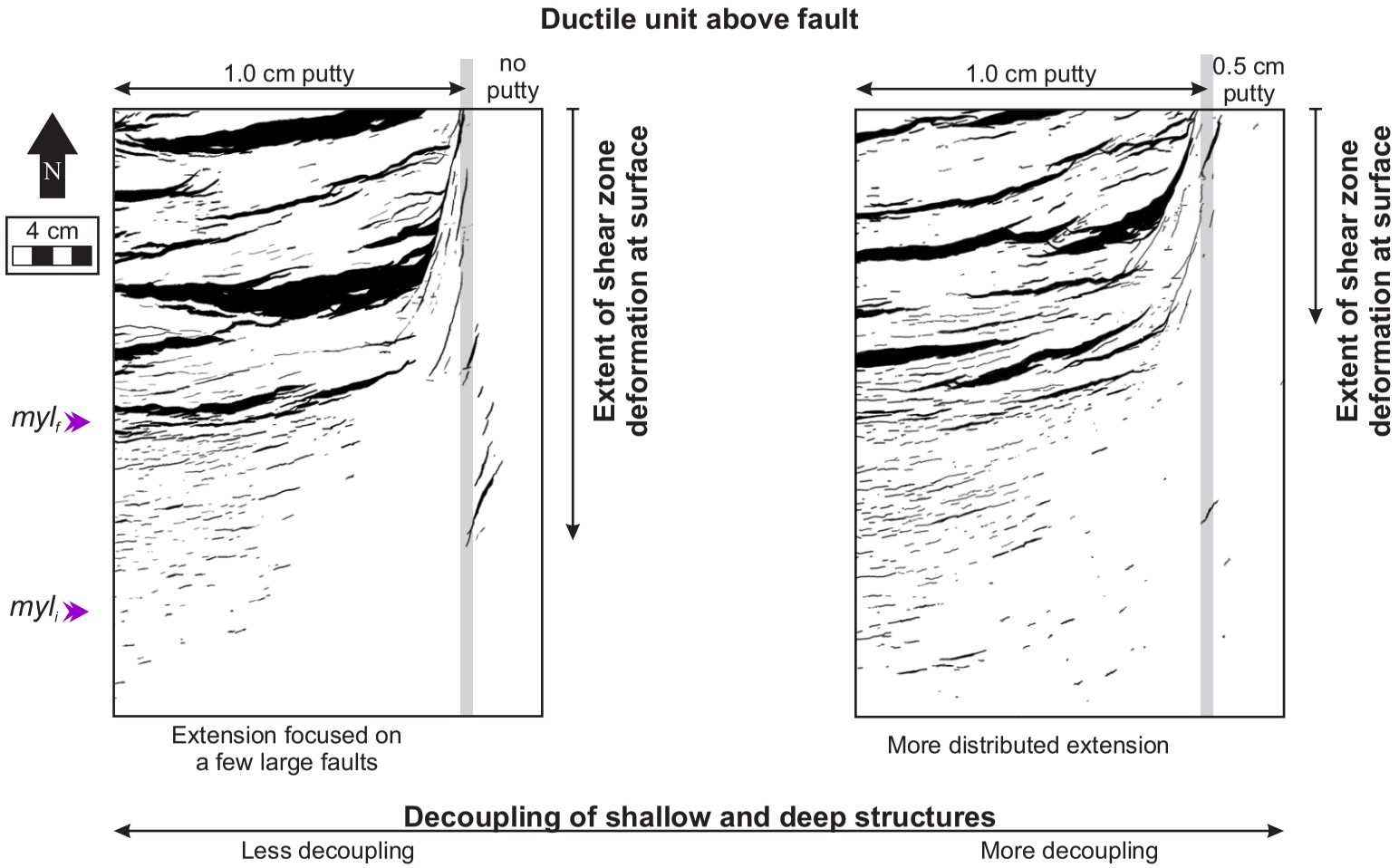

Fig. 4.3: Effect of putty above N-trending discontinuity on fault patterns at top of clay for (from left to right) Standard Model (10.0 cm displacement) and Putty-on-Discontinuity Model (10.0 cm displacement). Small purple arrows indicate initial and final positions of edge of mylar sheet (myl_i and myl_f respectively). Gray bars show approximate location of underlying N-trending discontinuity.

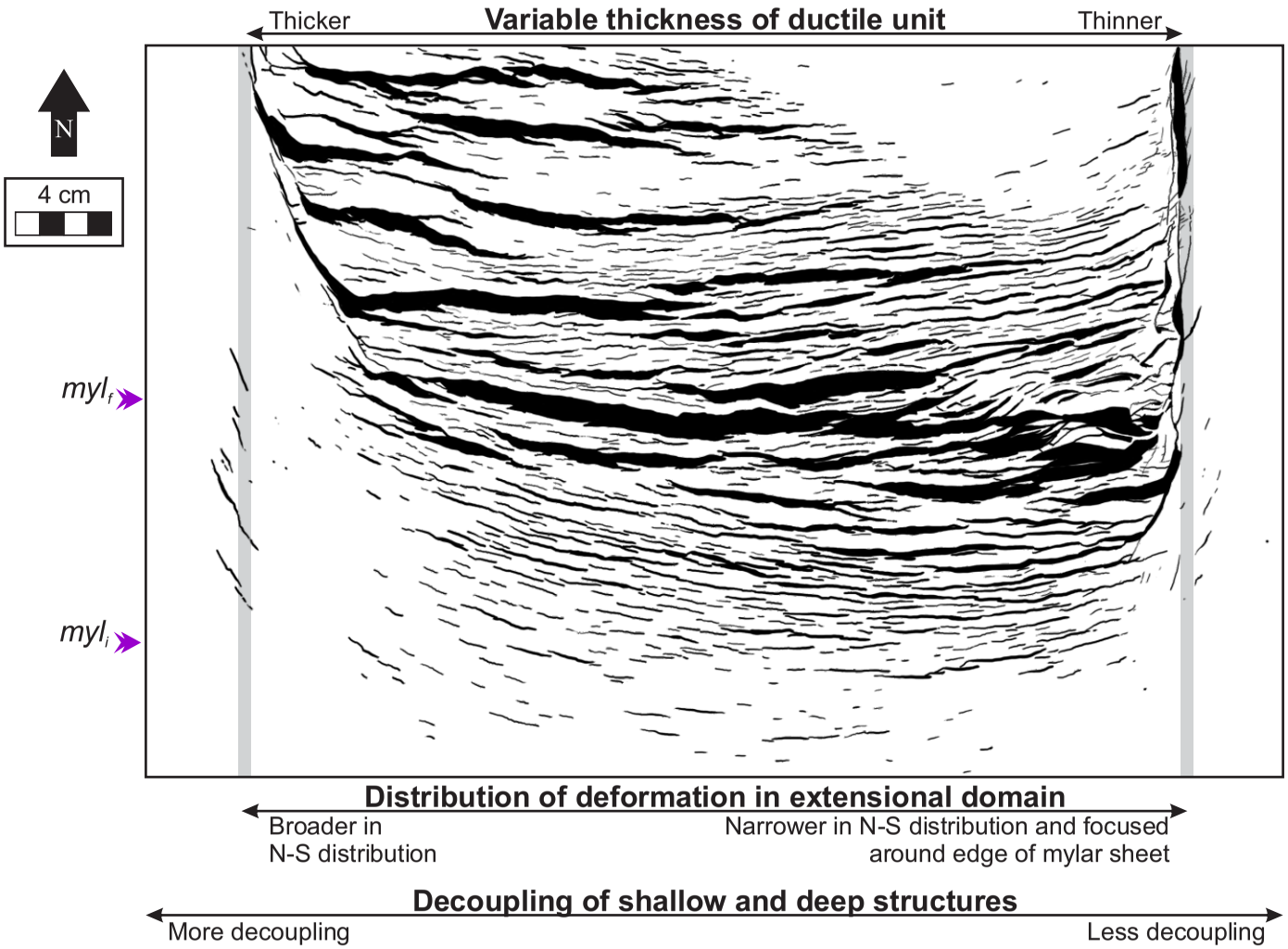

Fig. 4.4: Effect of varying putty distribution on fault patterns at top of clay for Variable-Putty Model (10.0 cm of displacement). Small purple arrows indicate initial and final positions of edge of mylar sheet (myl_i and myl_f respectively). Gray bars show approximate locations of underlying N-trending discontinuities.

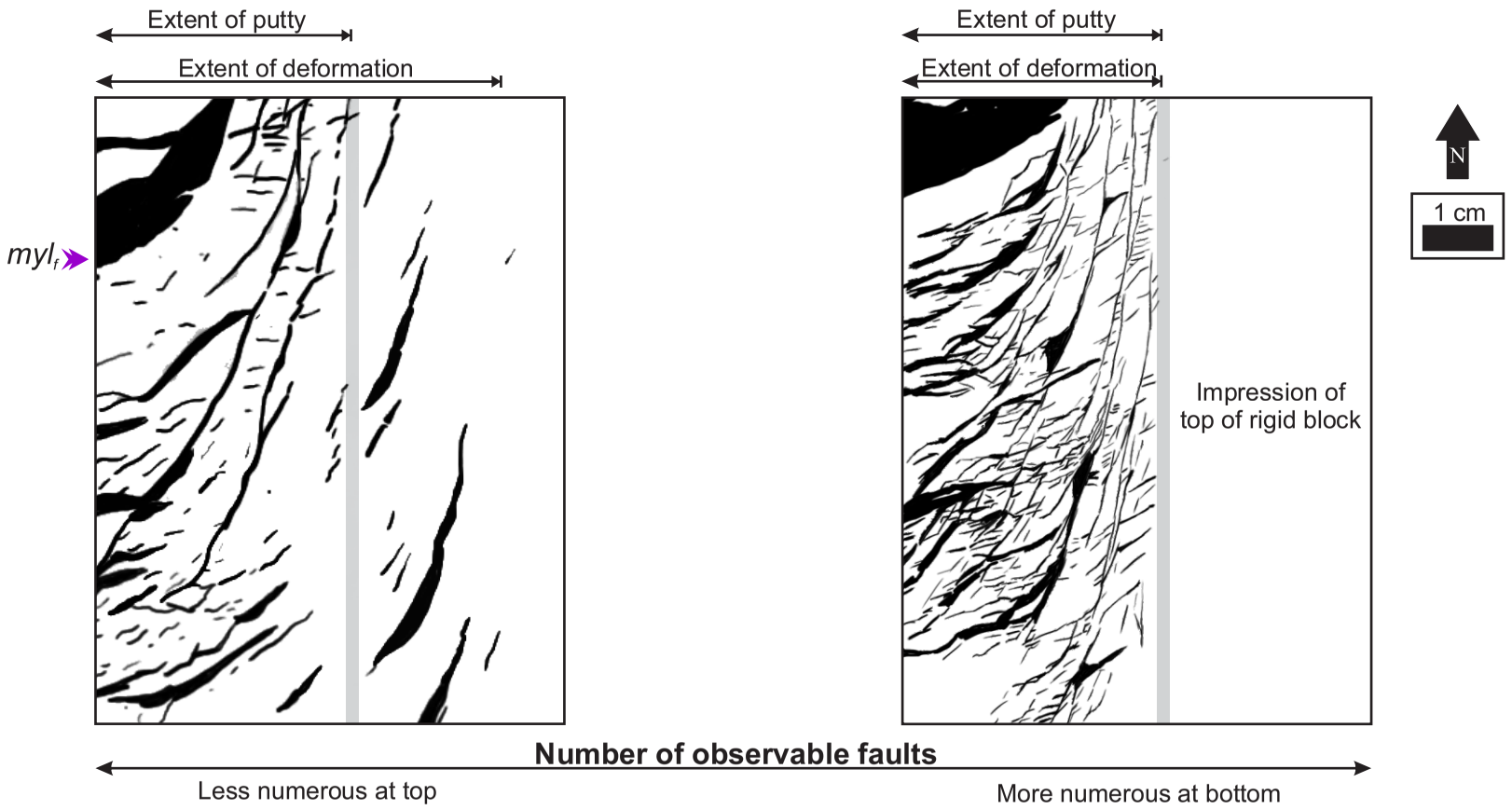

Fig. 4.5: Comparison of deformation at top (left) and bottom (right) of clay for thicker-putty side of Layered Model. Fault-trace images are from west side of Layered Model but are flipped (along N-S axis) to show fault orientations similar to other figures in Discussion. Illustrations are aligned to approximate final position of edge of mylar sheet (myl_f). Gray bars show approximate location of underlying N-trending discontinuity. For bottom of clay layer, not all faults are traced because some are too small to resolve and some features are possibly related to post-desiccation fracturing.

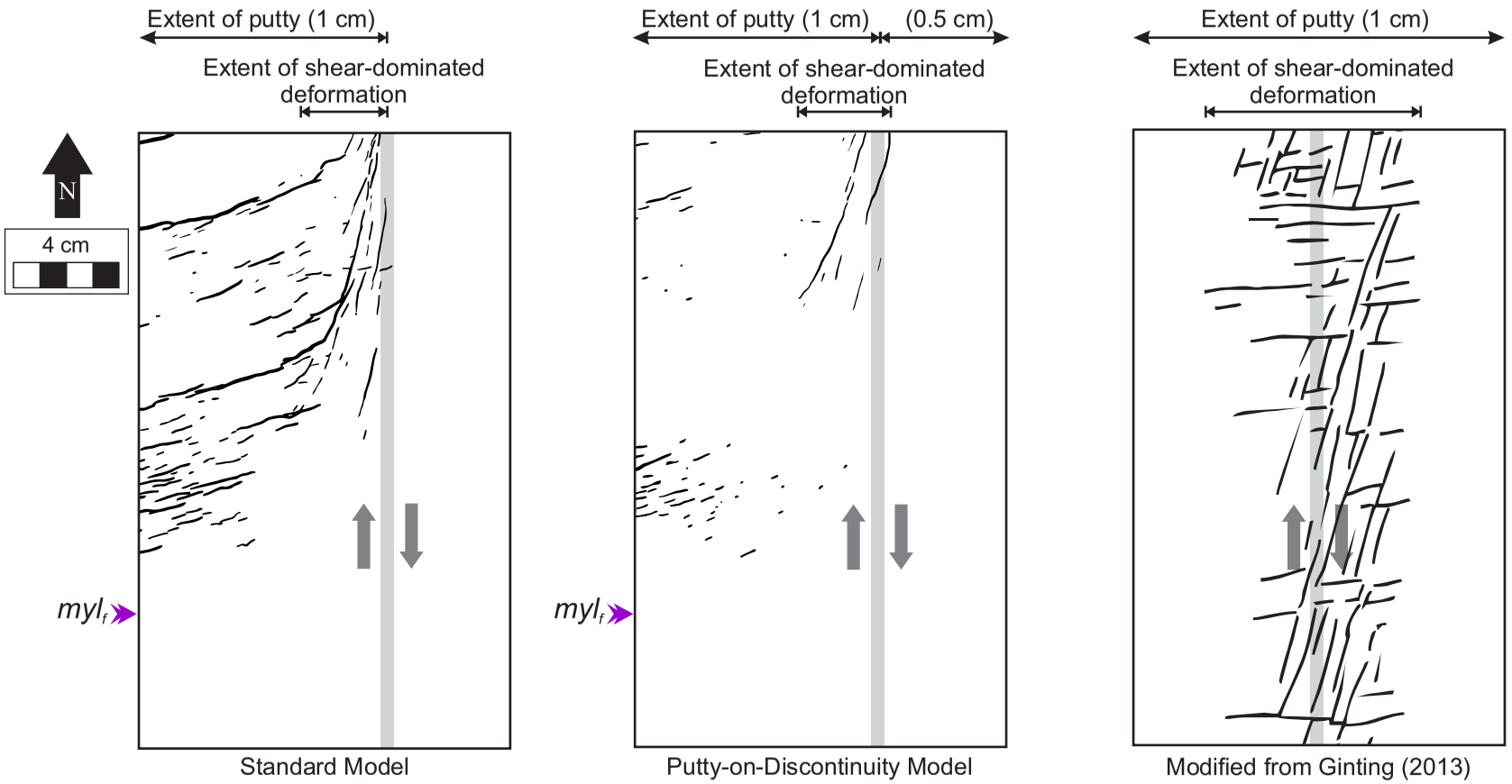

Fig. 4.6: Comparison of fault patterns in shear zones relative to lateral extent of underlying putty for (from left to right) Standard Model, Putty-on-Discontinuity Model, and clay model of Ginting (2013). All models have 5.0 cm of right-lateral displacement (dark gray arrows). Gray bars show approximate location of underlying N-trending discontinuity. For (left) Standard Model and (center) Putty-on-Discontinuity Model, purple arrows indicate final positions of edge of mylar sheet (*myl*$_f$). Top row of black arrows indicates lateral extent of underlying putty; second row of black arrows indicates lateral extent of shear-related brittle deformation at surface of wet clay.

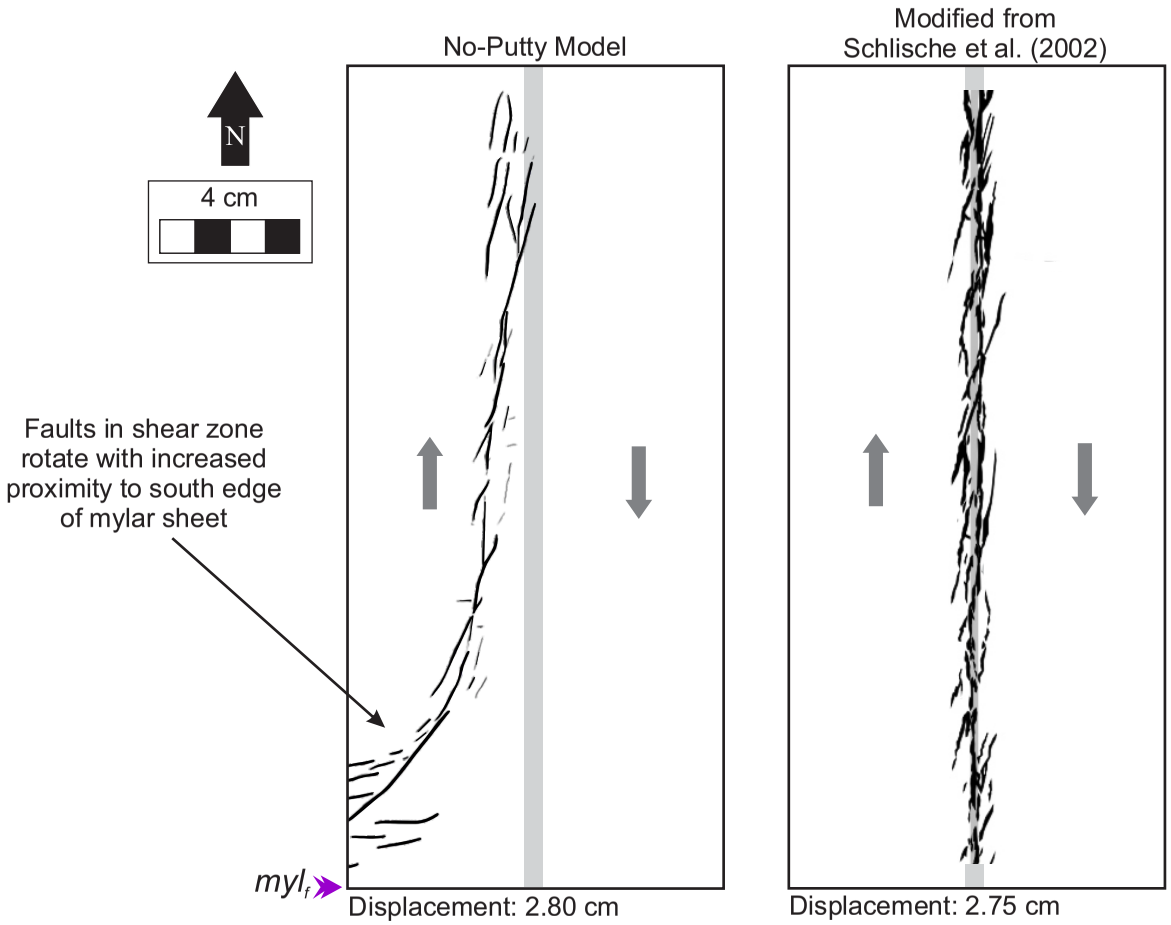

Fig. 4.7: Comparison of faults in shear zones in clay models with no putty: (left) No-Putty Model and (right) strike-slip model from Schlische et al. (2002). Gray bars show approximate location of underlying N-trending discontinuity. Dark-gray arrows give sense of displacement relative to the discontinuity. Purple arrow indicates final position of edge of mylar sheet (*myl*$_f$) for No-Putty Model.

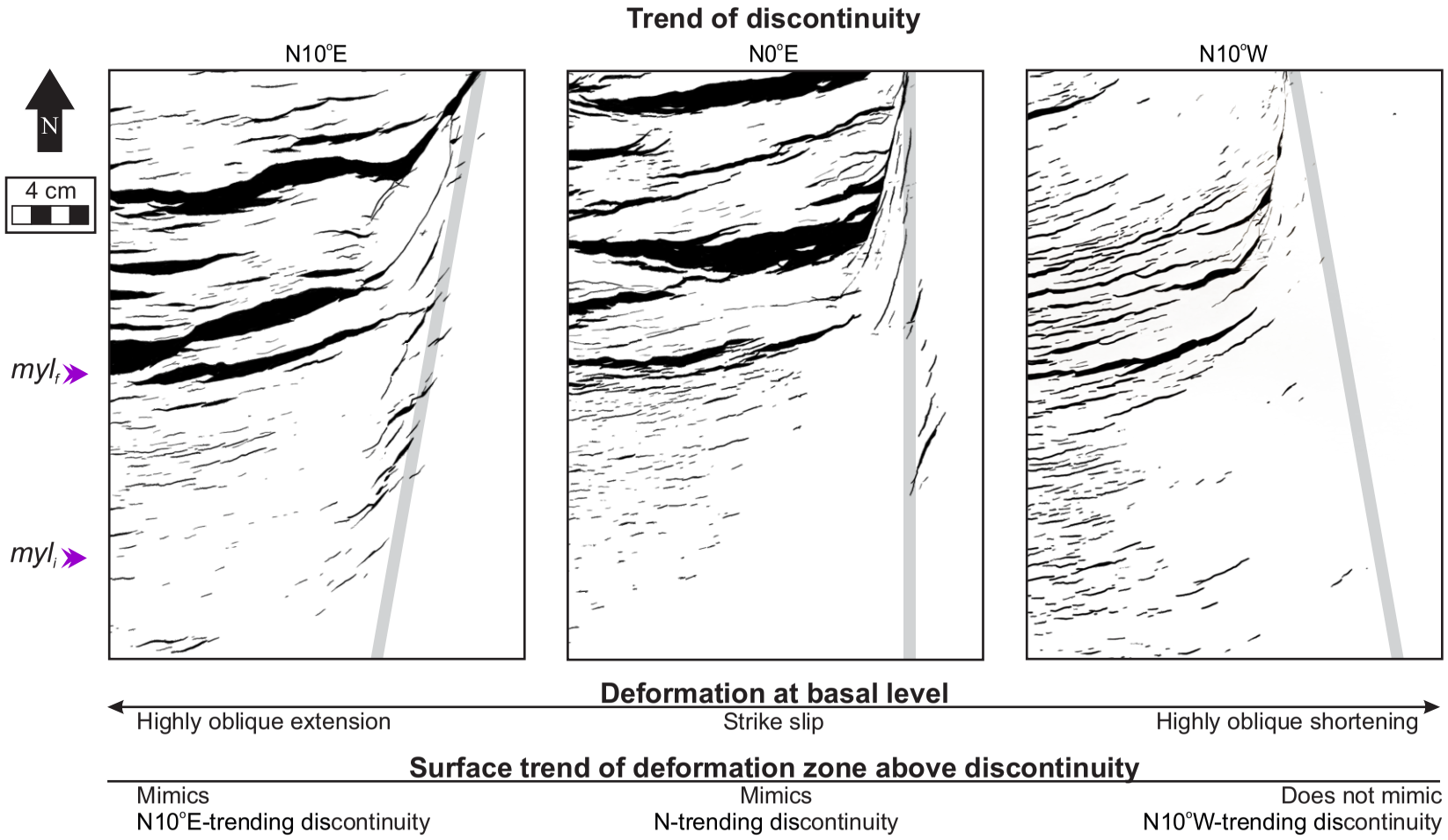

Fig. 4.8: Effect of varying the trend of the shear-dominated discontinuity on fault patterns at top of clay for (from left to right) N10°E Model, Standard Model, and N10°W Model (all with 10.0 cm of displacement). Small purple arrows indicate initial and final positions of edge of mylar sheet (myl_i and myl_f respectively). Gray bars show approximate location of discontinuity between ductile unit in the west and rigid block in the east.

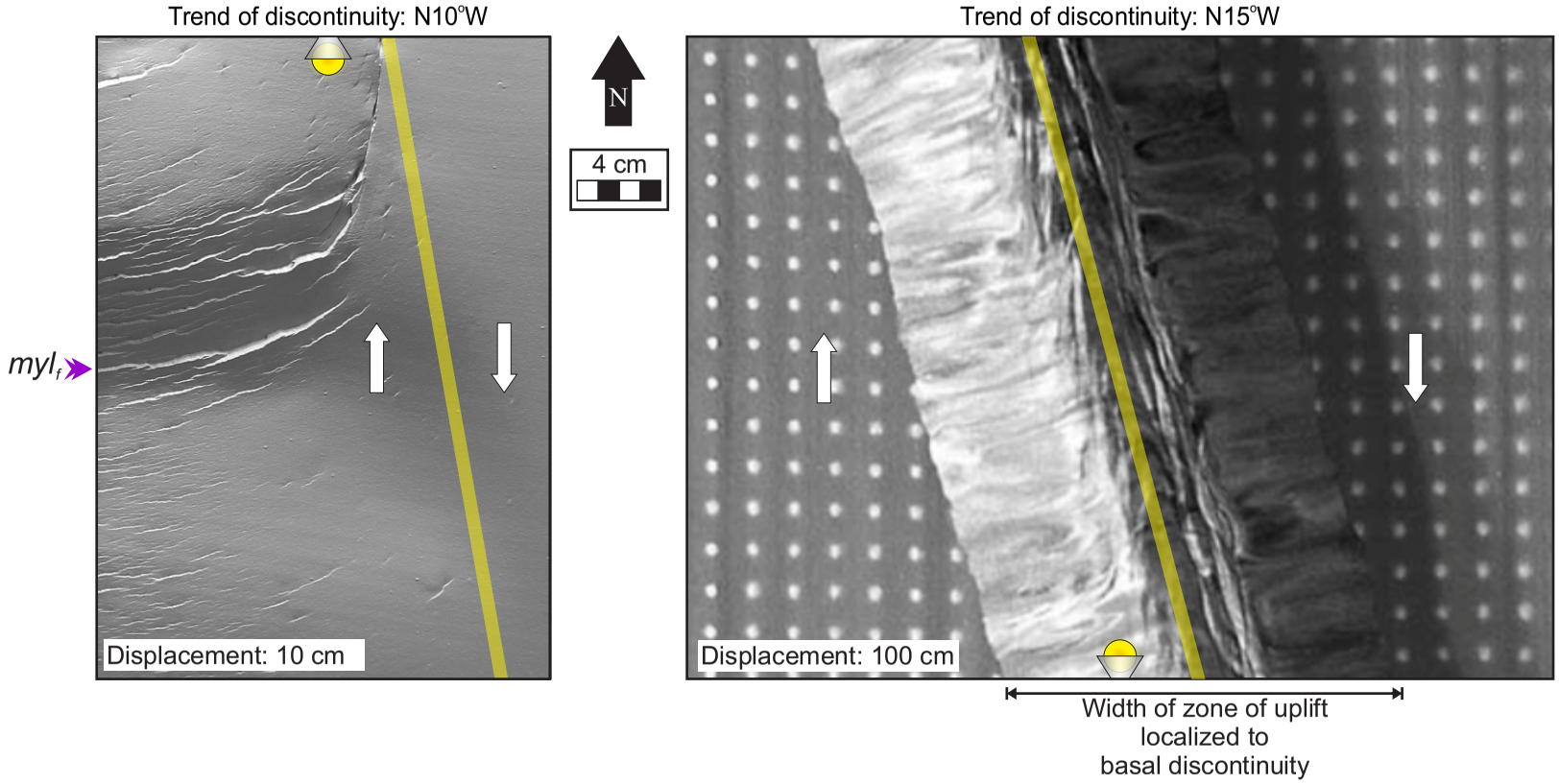

Fig. 4.9: Comparison of analog models with highly oblique shortening for (left) photo of N10°W Model and (right) photo of sand model of McClay et al. (2004). White arrows give sense of displacement relative to the basal discontinuity. Yellow bars show approximate location of discontinuity at depth. Discontinuity in clay model trends N10°W; discontinuity in sand model trends N15°W.

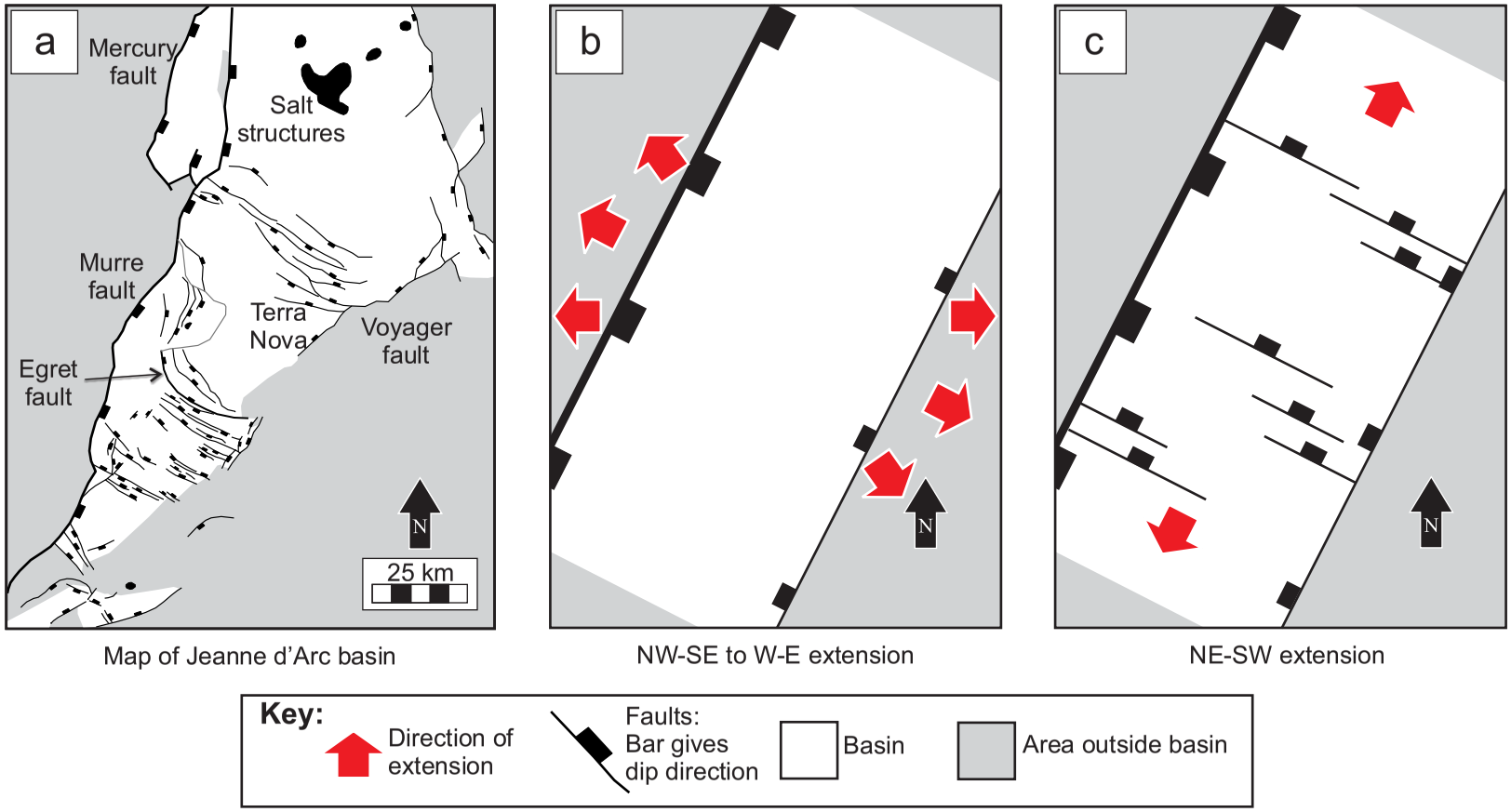

Fig. 4.10: Evolution of Jeanne d'Arc basin. (a) Map of Jeanne d'Arc basin (modified from Withjack and Schlische, 2005) showing location of major fault systems and the Terra Nova field, a region subsequently shown in Fig. 4:13a. Southern part of map shows faults cutting Middle Jurassic unit; northern part of map shows faults cutting Albian / Aptian unit. (b) Cartoon illustrating activity on the Murre, Mercury, and Voyager fault systems during the Late Triassic through Jurassic in response to NW-SE to W-E extension. (c) Cartoon illustrating a later episode of NE-SW extension during the Early Cretaceous.

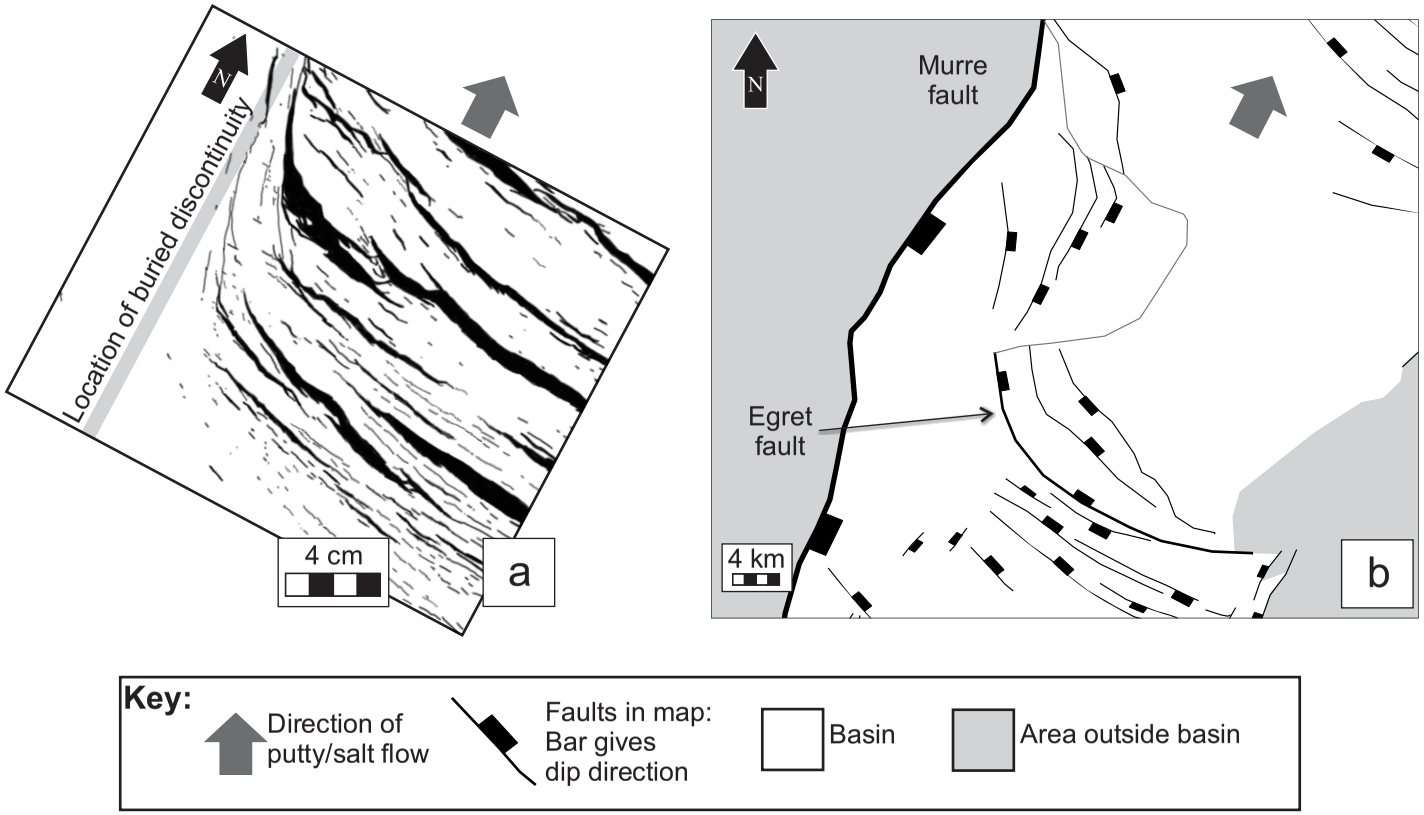

Fig. 4.11: Comparison of faults in (a) Putty-on-Discontinuity Model to (b) faults pattern in the central Jeanne d'Arc basin (map modified from Withjack and Schlische, 2005). (a) Cropped Putty-on-Discontinuity-Model fault-trace map is rotated so that direction of displacement of the mylar sheet is parallel to the inferred direction (NE) of salt flow in Jeanne d'Arc basin. Fault-trace map is flipped from E-W so that shear-dominated discontinuity (gray bar) is in west to relate the buried rigid block to (b) sub-salt NE-striking splays of Murre fault. Note the centimeter scale for Putty-on-Discontinuity Model and kilometer scale for map of Jeanne d'Arc basin.

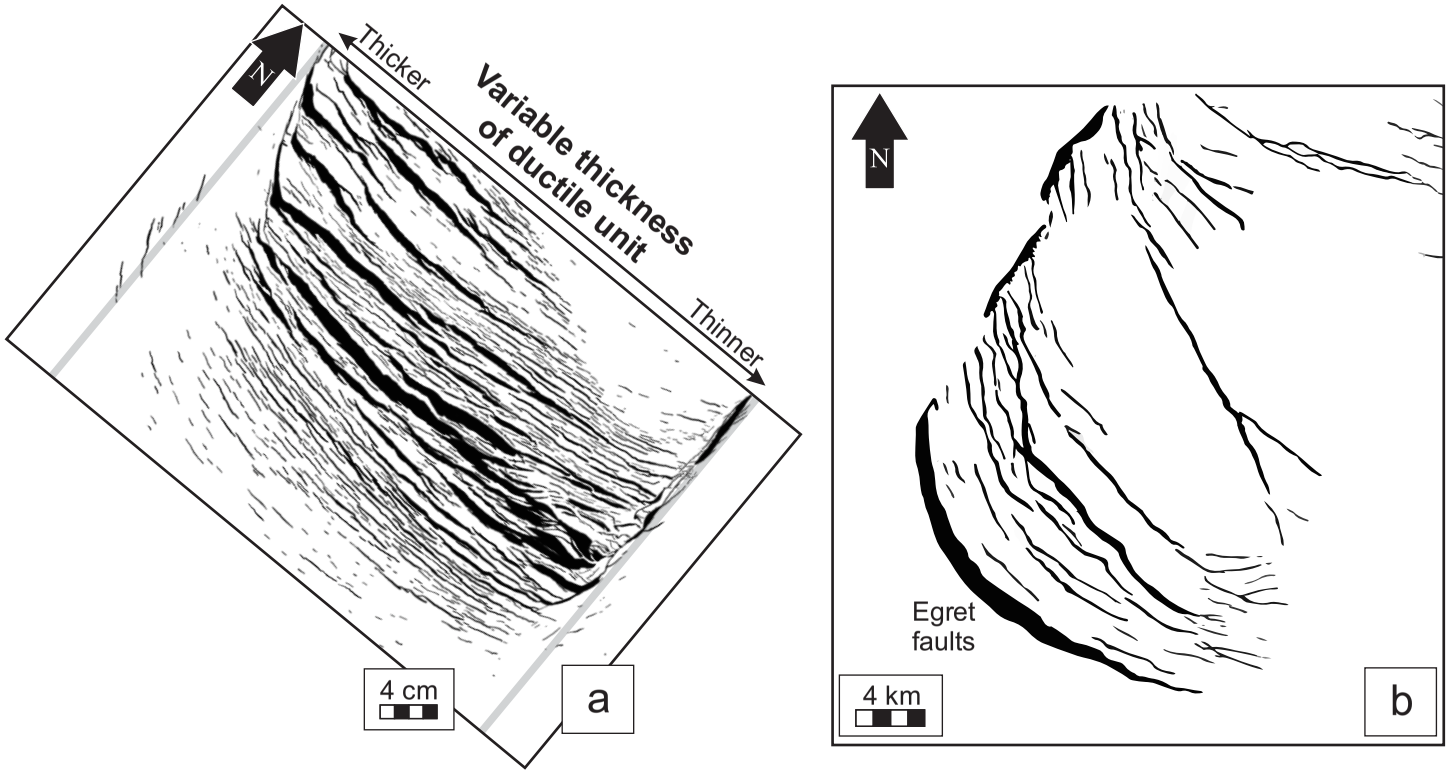

Fig. 4.12: Comparison of deformation in (a) Variable-Putty Model and (b) Jeanne d'Arc basin. (a) Fault-trace map of Variable-Putty Model is rotated so that the direction of displacement of the mylar sheet is parallel to the inferred direction (NE) of salt flow in Jeanne d'Arc basin. (b) Black polygons are faults cutting the Tithonian (Upper Jurassic) unconformity (modified from McIntyre et al., 2004). Southwest side of map shows NNW- to NW-striking faults linking with NE-striking faults. Note the centimeter scale for Variable-Putty Model and kilometer scale for map of Jeanne d'Arc basin.

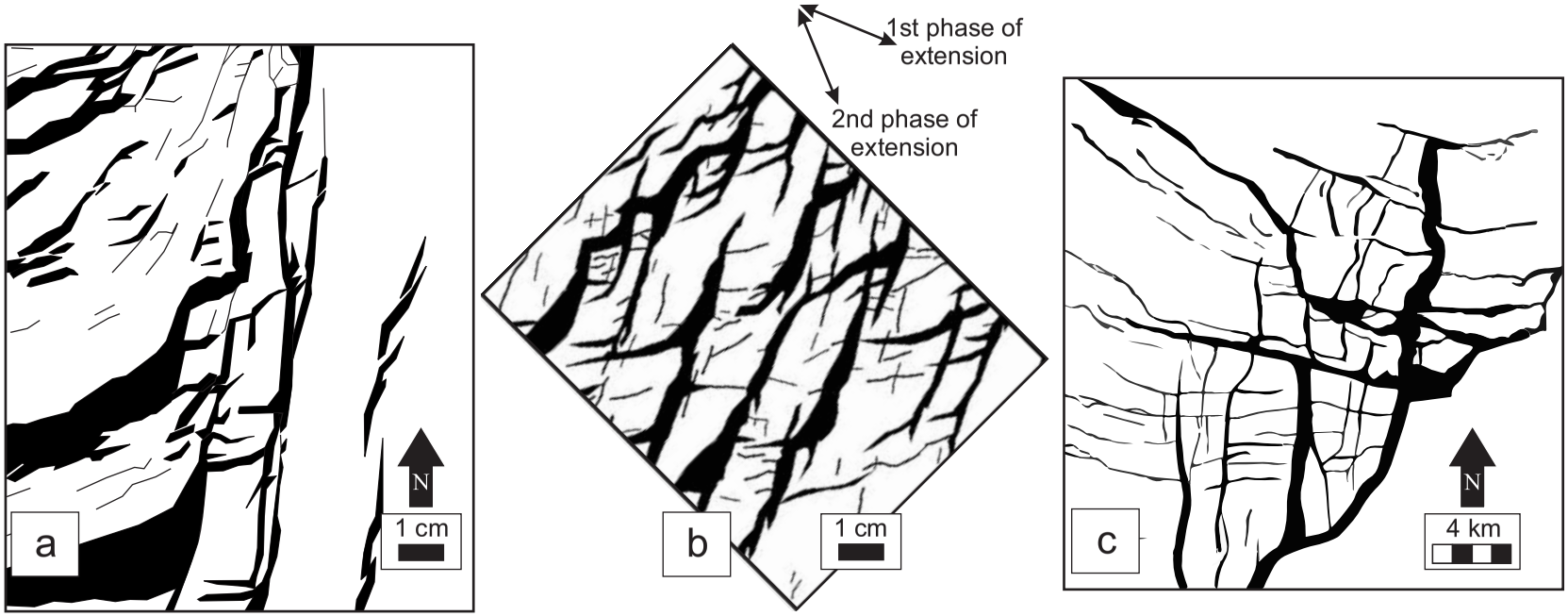

Fig. 4.13: Orthogonal fault sets in models and Jeanne d'Arc basin. (a) Orthogonal fault sets in Thin-Putty Model. (b) Clay model (modified from Henza et al., 2009) with two phases of non-coaxial extension (indicated by arrows) has orthogonal fault sets. (c) Map of Terra Nova region (modified from McIntyre et al., 2004) shows orthogonal fault sets with N- and E-striking faults that have similar geometry to orthogonal fault sets produced in clay models (a and b).